Narrowband Interference Detection and Mitigation for Indoor Ultra-Wideband Communication Systems

A Thesis Submitted

to the College of Graduate Studies and Research

in Partial Fulfillment of the Requirements

for the Degree of Master of Science

in the Department of Electrical and Computer Engineering

University of Saskatchewan

By

Huy Quang Quach

Saskatoon, Saskatchewan, Canada

PERMISSION TO USE

In presenting this thesis in partial fulfillment of the requirement for a Degree of Master of Science from the University of Saskatchewan, the author agrees that the libraries of this University may make it freely available for inspection. The author further agrees that permission for copying of this thesis in any manner, in whole or in part for scholarly purposes may be granted by the professor who supervised this thesis work or, in his absence, by the Head of the Department or the Dean of the College of Graduate Studies and Research at the University of Saskatchewan. Any copying, publication, or use of this thesis, or parts thereof, for financial gain without the author's written permission is strictly prohibited. Proper recognition shall be given to the author and the University of Saskatchewan in any scholarly use which may be made of any material in this thesis.

Request for permission to copy or to make any other use of material in this thesis in whole or part should be addressed to:

Head of the Department of Electrical and Computer Engineering,

57 Campus Drive,

University of Saskatchewan,

Saskatoon, Saskatchewan,

Canada S7N 5A9

ABSTRACT

In February 2002, the FCC (2002 a, b) issued a ruling that ultra-wideband (UWB) could be used for data communications as well as for radar and safety applications. UWB system is constrained to have a maximum power transmission of -41 dBm and a bandwidth ranging from 3.1-10.6 GHz. UWB co-exists and does not interfere with the existing narrowband or wideband communication systems in the same spectrum. However, due to its low power in the same bandwidth, UWB is affected by the so-called narrowband (NB) interference. This thesis presents a method to estimate and detect narrowband signals in radio impulse receiver with the intention to eliminate the NB interference.

Narrowband bandwidth is very small compared to the bandwidth of UWB therefore the interference can be considered as a single tone. To detect such a tone using conventional techniques is not feasible at least up to this time for UWB as current technology can not support such high data rates. Alternatives way to track down the narrowband signal include using a power spectral density estimation technique called spectrogram. For all cases, the spectrogram at specific frequency range where the narrowband active statistically be larger than its overall average power. Here, a threshold detector is built which reports detection at the frequency range where the narrowband is located if the spectrogram exceeds a threshold value.

Upon completing of successful NB detection, the NB signal in the UWB system will be estimated in digital form and cancelled in analog form. The pipelined LMS algorithm is used to estimate the NB signal; the algorithm is implemented using a built-in IP core from the Altera DSP library which can be simulated in either Matlab platform or in FPGA boards. The design correctness has been validated by means of Monte-Carlo

simulation and hardware implementation using standard UWB IEEE standard channel models, Time Hopping-Pulse Position Modulation and the rake receiver technique.

ACKNOWLEDGEMENTS

I extend my gratitude to Dr. Anh V. Dinh for his guidance and support throughout this thesis work. I also wish to thank Natural Sciences and Engineering Research Council (NSERC) for financial backing and resources to complete this research. Many thanks go to my colleagues Bi Pham and Yongsoon Lee for many productive technical conversations.

Thank you to my aunt, Tuyet Ngoc Tran, for allowing me to stay at her place and cooking for me during the course of my studies.

Special thanks go to my parents, Thien Van Quach and Lang Ngoc Tran for providing years of encouragement.

TABLE OF CONTENTS

LIST OF FIGURES

LIST OF ABBREVIATION

ADC	Analog to Digital Converter
ASIC	Application-Specific Integrated Circuit
AWGN	Additive White Gaussian Noise
BER	Bit Error Rate
BPM	B-Phase Modulation
BPSK	Binary Phase Shift Key
CLA	Carry-Look-Ahead
CLB	Configurable Logic Block
CPLD	Complex Programmable Logic Device
CRA	Carry-Ripple Adder
CUL	Coefficient Update Loop
DARPA	Defense Advance Research Projects Agency
DFT	Discrete Fourier Transform
DSP	Digital Signal Processing
DU	Desired-to-Undesired ratio
EFP	Error Feedback Path
EIRP	Equivalent Isotropically Radiated Power
ESD	Energy Spectral Density
FCC	Federal Communication Commission
FFFP	Filter Feed-Forward Path
FPGA	Field Programmable Gate Array
IEEE	Institute for Electrical and Electronics Engineers

IID	Independent and Identical Distribute
INR	Interferer to Noise Ratio
IR	Impulse Radio
ISI	Inter-Symbol Interference
LMS	Least Mean Square
LUT	Look-Up-Table
MAA	Multiply and Accumulate
MAC	Medium Access Control
MAI	Multiple Access Interference
MB	Multi Band
μP	Microprocessor
MMSE	Minimum Mean Square Error
MRC	Maximal Ratio Combiner
MSD	Mean Square Deviation
MSE	Mean Square Error
NB	Narrowband
NBI	Narrowband Interference
NLMS	Normalize Least Mean Square
OFDM	Orthogonal Frequency Division Multiplexing
OOK	On-Off Keying
PAM	Pulse Amplitude Modulation
PBI	Partial Band Interference
PCI	Peripheral Component Interconnect

PDA	Personal Digital Assistant
PDF	Probability Density Function
PPM	Pulse Position Modulation
PSAM	Pilot-Symbol Assisted Modulation
PSD	Power Spectral Density
RF	Radio Frequency
RLA-LMS	Relaxed Look-Ahead LMS
RV	Random Variables
SoC	System on Chip
SSS	Strict-sense-stationary
TH-PPM	Time-Hopping Pulse Position Modulation
UWB	Ultra Wideband
WB	Wideband
WLAN	Wireless Local Area Network
WPAN	Wireless Personal Area Network
WSS	Wide Sense Stationary

Chapter 1 Introduction and Motivation

The most influential milestone in the history of Ultra Wideband (UWB) wireless communications was set in April 2002 when the Federal Communications Commission (FCC) approved the first guidelines allowing UWB signals contained within specified emission masks [1]. This chapter describes what UWB is, why and how this technology gets adopted into wireless communications. The importance of this technology is its co-existence with other technologies in the same spectrum. Sharing spectrum causes problems in UWB communications, which motivate for this work.

1.1 Ultra Wideband Overview

Historically, UWB radio systems were mainly developed as a military tool because they have acquired high capability to scan through trees and beneath ground surfaces. Recently, UWB technology has been focused on consumer electronics and communications. Although UWB systems are years away from being ubiquitous, UWB technology is changing wireless industry today. UWB technology is different from the conventional narrowband wireless transmission technology. Instead of broadcasting on separate frequencies, UWB spreads signals across a very wide frequency range. The signals are transmitted in sequences of very short pulses rather than continuous waveforms using Radio Frequencies (RF) carrier as in narrowband (NB) communication

systems. This technique has been extensively used in radar applications and went under the name of Impulse Radio (IR).

The most remarkable roadmap in UWB wireless communications was regulated in April 2002 by FCC. However, according to the FCC rules, UWB concept is not limited to the pulsed transmission but can be extended to continuous-like transmission techniques, providing the occupied bandwidth of the transmitted signal is greater than 500 MHz. The general consensus establishes that a signal is UWB if its bandwidth is large with respect to the carrier or center frequency of the spectrum. In other words, the fractional bandwidth is as high as 0.2-0.25 percent of its central frequency. These pulses or waveforms, because of their large bandwidth, must, at least in principle, co-exist in a friendly manner with other Hertzian waveforms present in the air interface. The coexistence principle introduces strict limitations over Power Spectral Densities (PSD) and raises the issue of designing power efficient networks in addition to the narrowband interference (NBI) avoidance in UWB communication systems.

The following section describes the modulation techniques that are most commonly used in the UWB systems.

1.1.1 Type of Modulation in UWB Systems

UWB signals are obtained by either applying the Pulse Position (PPM), Pulse Amplitude (PAM), On-Off Keying (OOK), and Bi-Phase modulation. Each of these modulation techniques will be examined.

In PPM modulation, each pulse is delayed or sent in advance of a regular time scale. A binary communication system can be established with a forward or backward shift of the pulse in time. By setting specific time delay for each pulse, an M-ary system

can be created. Considering Figure 1-1 which provides an illustration of a 4-ary PPM modulation, here T_c is associated with the amount of time allocated to transmit one UWB pulse. T_c is therefore divided into M different time slots of width λ. In this case, M=4, the bit or symbol which is being transmitted determines which time slot the pulse occupies.

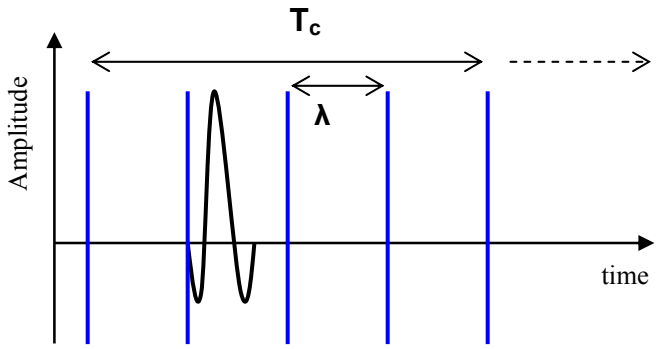

Figure 1-1. A 4-ary PPM.

Another common modulation method is to invert the pulse, that is, to create a pulse with opposite phase. This is known as bi-phase modulation (BPM). Bi-phase is therefore antipodal and in a purely additive whit Gaussian noise (AWGN) channel has error performance identical to binary phase shift keying (BPSK). Figure 1-2 illustrates a bi-phase modulation where a negative pulse represents a "0" and a positive pulse represents a "1".

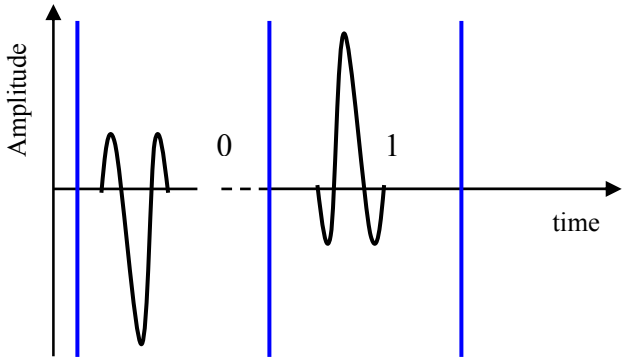

Figure 1-2. A Bi-phase Modulation.

PAM is an M-ary modulation format where the information is encoded into an amplitude of the pulse. Figure 1-3 gives an example of a 4-ary PAM. PAM however is not a particularly attractive modulation scheme for UWB since its modulation order (M-ary) is inversely proportional to its energy efficiency and UWB systems are power limited.

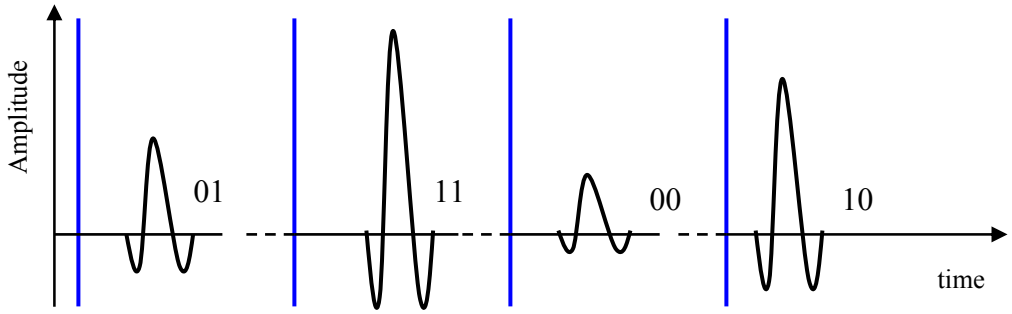

Figure 1-3. A 4-ary PAM.

It is worth to mention OOK. This is a modulation technique where the absence or presence of a pulse signifies the digital information of "0" or "1". This technique is also not very energy efficient but may be attractive for a low cost, low complexity system. Figure 1-4 provides an example of OOK modulation.

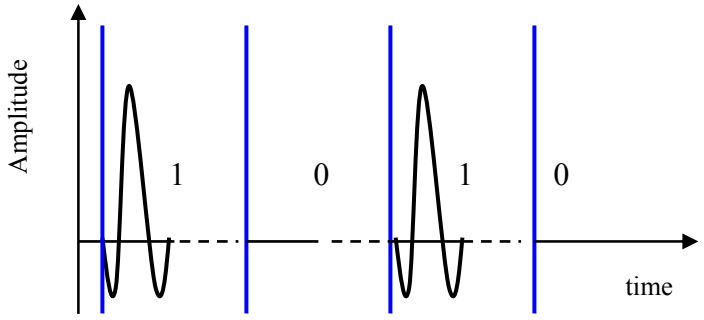

Figure 1-4. A On-Off Keying (OOK).

1.1.2 Fractional Bandwidth

As mentioned earlier, the term UWB comes from the radar world and refers to electromagnetic waveforms that are characterized by an instantaneous fractional energy bandwidth greater than 0.2-0.25. Let E be the instantaneous energy of the waveform, the energy bandwidth is then identified by the frequencies f_L and f_H, which delimited the interval where most of the energy E (i.e., over 90%) is captured. The width of the interval $[f_L, f_H]$ is called energy bandwidth as shown in Figure 1-5 [2]. Note that if f_L is the lower limit and f_H is the upper limit of the Energy Spectral Density (ESD) and the center frequency of the spectrum is located at $(f_L + f_H)/2$.

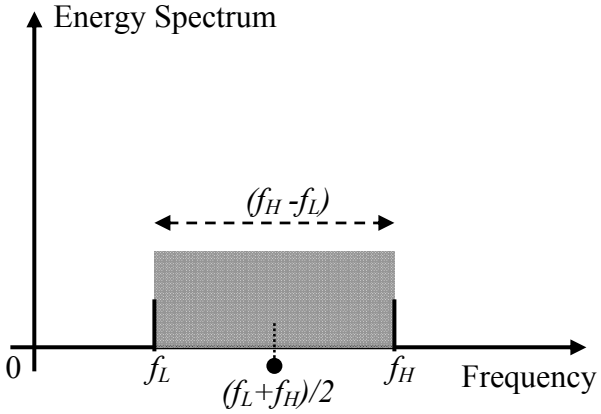

Figure 1-5. Energy bandwidth.

Fractional bandwidth is defined as the ratio of the energy bandwidth and the center frequency and expressed as:

$$\text{Fractional bandwidth} = \frac{(f_H - f_L)}{\frac{(f_L + f_H)}{2}} \qquad \textbf{(1-1)}$$

A signal having fractional bandwidth greater than 0.2-0.25 is called a UWB signal. A signal with an energy bandwidth of 2 MHz, for example, is UWB if the center frequency of its spectrum is lower than 10 MHz.

Often the term “percent bandwidth” is used. Percent bandwidth is simply the fractional bandwidth in percentage units. Also in use is the relative bandwidth which is equal to half of the fractional bandwidth. Relative bandwidth represents the ratio between half of the energy bandwidth and the center frequency.

There are different ways to choose the lower and upper limit frequencies depending on how stringent the requirement on the bandwidth is set. For example, in a recent release of UWB emission masks in the United States (FCC, 2002), the f_L and f_H are set to be the lower and upper frequencies of the -10dB emission points. The selection of -10 dB over the -20 dB bandwidth established by the Defense Advance Research Projects Agency (DARPA) [3] is motivated by the fact that UWB emission is permitted at lower power levels, which are close to the noise floor. Under these conditions, the -20 dB emission points cannot be measured correctly. Within the FCC, 2002 regulation, a signal is always assumed to be UWB if its bandwidth at -10dB emission point exceeds 500 MHz, regardless of the fractional bandwidth values.

The type of NB signal contains within the UWB spectrum will be examined in the following sections.

1.2 Narrowband Overview

Narrowband (NB) refers to a signal which occupies only a small amount of spaces on the radio spectrum. NB is opposite to the broadband or wideband (WB). In the study of wireless communications such as a UWB system, narrowband implies that the bandwidth under consideration is sufficiently “narrow” compared to the UWB bandwidth. The NB in study for indoor communications is the wireless local access network (WLAN) based Orthogonal Frequency Division Multiplexing (OFDM) signal.

This WLAN system is also known as the third wireless generation and has been used to offer maximum data rate at a central frequency in the 5 GHz frequency band. The standardization of this wireless generation is taking place simultaneously in the U.S., Japan and Europe. The Institute for Electrical and Electronics Engineers (IEEE) is working on this WLAN and models it as the IEEE 801.11a standard. The standard is based on the OFDM modulation scheme having a bandwidth of 16 MHz per subcarrier in OFDM. The modulation scheme ranges from BPSK up to 64-QAM. Together with a variable error-coding rate, OFDM modulation allows the data rate to be adapted from 6 Mbit/s to 54 Mbit/s, depending on the propagation channel conditions. The IEEE 802.11a is the primary interference for indoor UWB communication systems. Interference concept is to be discussed in the subsequent section.

1.3 Interference

A WB system, by its nature, interferes with the existing NB services in the same frequency band and in turn, the NB signals act as interferers to the WB system. The extent to which performance is degraded by the interference clearly depends on the number and distribution of the interferers, the relative power between WB and NB and the type of modulation of the two signals. With respect to transmission power, FCC specifications and European standards [4], essentially limit the equivalent isotropically radiated power (EIRP) to US Part 15 limits, that is, -41 dBm/MHz for UWB in the range of frequency from 3.1-10.6 GHz. To be UWB, the signal must occupy an instantaneous bandwidth of at least 500 MHz. Figure 1-6 in next page illustrates the FCC UWB spectral masks.

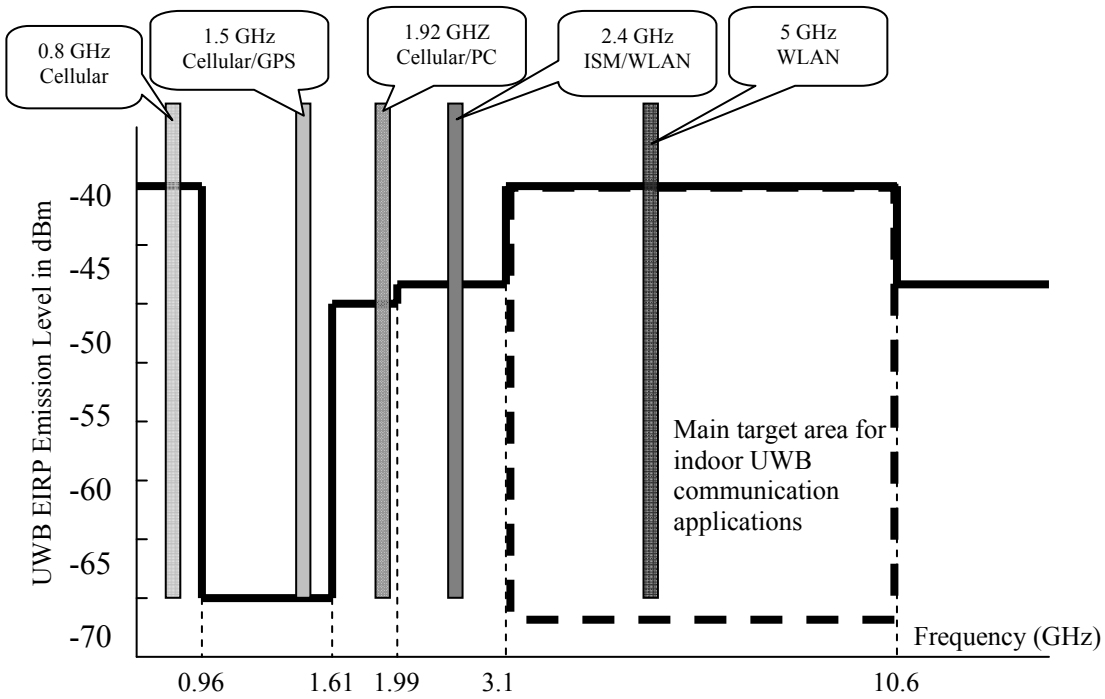

Figure 1-6. FCC UWB Spectral Masks.

The specifications intent is to enable the co-existence of UWB radio services with the currently licensed NB services, including commercial cellular as well as critical applications, such as the Global Position Systems (GPS) and navigation systems. A brief commentary on the narrowband interference that inflicted and observed from UWB system is addressed here and detailed analysis is to be given in Chapter 2.

Figure 1-6 shows within the spectrum of interested, the narrowband interference (NBI) is the 5 GHz OFDM based WLAN signal. There are works studying degradation in the performance of UWB radios due to narrowband interference within the 3.1-10.6 GHz frequency range, such as tone jammers [5], partial band interference (PBI) [6] and WLAN IEEE 802.11a interference [7]. If the frequency of the tone jammers is known, several techniques can be used to shape the transmit pulse in such a way to avoid the interference [8-10]. In [11], spreading codes are designed to combat NBI using frequency-spreading technique. The performance of generalized RAKE receivers and

Minimum Mean Square Error (MMSE) receivers, in the presence of Multiple Access Interference (MAI) and NBI, has been analyzed in [12-15]. These techniques assume that all relevant user codes, multipath parameters, and noise parameters are known. Performance in the presence of multiple users was also studied. For example, Forouzan provided an exact bit error rate (BER) expression for the interference limited uncoded time-hopping pulse position modulation (TH-PPM) and approximate expressions for the coded asynchronous case [16]. Authors in [7] and [17-20] provided both analysis and simulation results for NB interference effect on UWB system.

As mentioned earlier, the primary narrowband interference occupies within the indoor UWB communication system is the IEEE802.11a; in particular the OFDM based WLAN signal, the power spectrum density for NBI scenario is shown in Figure 1-7. In contrast to the UWB, the WLAN NB allowed emission is +40 dB/MHz, which may be expected to be 10-12 dB above the noise floor while the UWB emission below this noise level. As the result, the presence of NB may cause severe degradation in the performance of UWB systems.

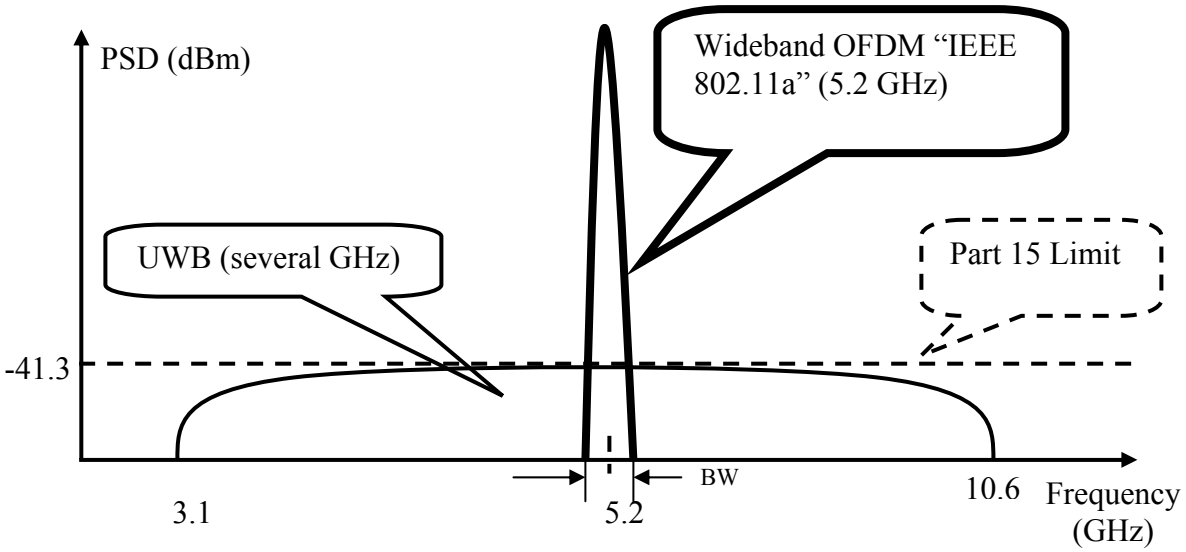

Figure 1-7. UWB indoor communication narrowband interference spectrums.

Ikegami and Ohno proposed two solutions to combat such NBI [21]. One is to use a filter to remove unwanted interference. For example, a sixth-order Chebyshev filter with a cutoff frequency at 4 GHz, a ripple less than 0.2 dB, and a -20 dB attenuation at 5.18 GHz can be used. This filter causes a 1 dB loss when there is no interference, however, significant performance improvement can be achieved with the presence of the interfering signal. The second solution is the use of a multi-band UWB system by applying a system with 11 subcarrier pulses at an interval of 200 MHz from 3.2 to 5.2 GHz. The highest frequency subcarriers are removed because they overlap with the 802.11a spectrum. It was concluded that, at a desired-to-undesired (DU) ratio of 0 dB, removal of the two highest subcarriers gives the best BER performance, while at a DU ratio of -10 dB, removal of three subcarriers gives the best performance.

The NBI problem in the UWB system remains open for other alternative solutions and leads to the work of this thesis. Motivation and research objectives are to be discussed in the following section.

1.4 Motivation and Research Objectives

Within the 3.1-10.6 GHz frequency band, the narrowband interference (NBI) is the major component that contributes to the degrading of the indoor UWB systems performance. There are published works scoping with the NBI [22-24]. Research in this thesis continues from the previous works and extends NBI cancellation studies into ways that are more practical by shifting from Matlab simulation into hardware synthesis utilizing the Digital Signal Processing (DSP) Unit in a Field Programmable Gate Array (FPGA).

The excitement of this research is the hands-on with practical experiments, working with Signal Compiler recently developed by Altera which lends the tools to convert from Simulink blocks into a hardware synthesisable code.

The objective of this thesis work is to develop a NB detection and a NB cancellation unit in the UWB system. For indoor communications, NBI occurs on an occasional basis, thus it is worth to detect the presence of NB signal and turn on a NB cancellation unit whenever the narrowband interference is detected. The benefit having a NB detection in place is to save energy by turning off the NB canceller and removing the latency that generated by the NB estimator when the narrowband interference is absent.

The bandwidth of the NB signal is much narrower compared to the bandwidth of the UWB signal therefore the interference can be considered as a single tone. To detect such a tone using conventional technique is not feasible at least up to this time as current technology can not support such high data rate in UWB. An alternative way tracking down the NB signal must be sought.

The major problem in combating interferences in UWB systems is signal acquisition. Therefore, the interference mitigation techniques which can be performed at the front end prior to acquisition are of interest for UWB systems. In addition, current digital technology is not suitable due to the extremely short duration pulses used in UWB. The interference rejection techniques that can be implemented in analog are more suitable but may not be cost effective due to the fact that purely analog take longer to design and must be re-designed for any change in future implementations. The goal for NBI suppression implementation targets cost effective and system simplification. The combination between analog and digital is the best fit and proved in [25, 26].

Giving that the adaptive filtering process occurs at the Intermediate Frequency (IF) stage, hardware required to implement the adaptive filter must process at the IF rate. Operating at such a rate requires a sampling rate in the order of hundreds of MHz. Currently available DSP can be clocked at a maximum of 400-600 MHz, therefore, the sampling rate achieved for adaptive filter implementation is as low as few GHz which is not efficient in UWB systems. Thus, a technology that provides a combination for the speed of an ASIC and the reprogrammbility of a microprocessor is highly desirable. FPGA provides a good combination of these features for high-speed implementations with the flexibility of a Commercial Off-the-Shelf (COTS) platforms. Current FPGA's are capable of performing the necessary processing demanded by most adaptive filters although this requires further optimization of the algorithms to facilitate real-time operation. This thesis concentrates on the development of high-speed adaptive filter architectures to estimate the NB signal in UWB system. The method of implementing adaptive filters in FPGA is exploiting large data processing concurrency in the form of parallelism and pipelining provided by the technology.

In this thesis, a new NB detection method and further improvement of the NBI suppression in UWB system are developed. The task is accomplished by replacing Matlab simulate DSP simulation models with a DSP implemented in FPGA devices.

1.5 Thesis Overview

This thesis focuses on two areas related to UWB system performance, detection and cancellation of the NBI. Chapter 2 discusses mathematical analysis and methods to generate a UWB signal as well as OFDM based WLAN signals. Impulse radio methods based on the generation of pulses that are very short in time and TH-PPM are described.

The methods of generating non-impulsive signal such as OFDM are also covered. This chapter also describes the derivations of the PSD for time-hopping UWB signals using PPM and OFDM signals. Chapter 3 looks into the NBI detection method. This chapter begins with a review of basic signal processing techniques, including mean, variance, FFT, spectrogram, and error probability. Finally, complete mathematical representations for NBI detection as well as false alarm probability are derived. Chapter 4 focuses on the design and formation of the NB estimation circuit. First, the methods to estimate frequency, phase and amplitude of the NB are addressed. Constructing the NB estimation circuit, part of the circuit formation, the digital LMS adaptive filter and NB elimination are discussed. Chapter 5 concentrates on the validation to support theories and discussions from Chapter 1 to Chapter 4. Conclusion and accomplishment are summarized in chapter 6. Potential work for future development is also suggested in this chapter.

Chapter 2 The UWB Radio and WLAN Based OFDM Signal

The UWB and NB concepts have been already discussed in Chapter 1. In this chapter, the extension of UWB and NB properties will be examined in more details in terms of mathematical representation as well as real time Matlab/Simulink generated signals. This chapter also studies the effect of NB onto the UWB in frequency domain.

2.1 The Ultra-Wideband Systems

The UWB system under studied consists of a transmitter to send an UWB signal to a receiver through a communication channel. Each of these components and the power spectral density of the signal is to be described in detail in the following section to set the foundation for development of the NB detection and elimination.

2.1.1 UWB Transmitter Structure

A general UWB transmitter block diagram is shown in Figure 2-1 [27].

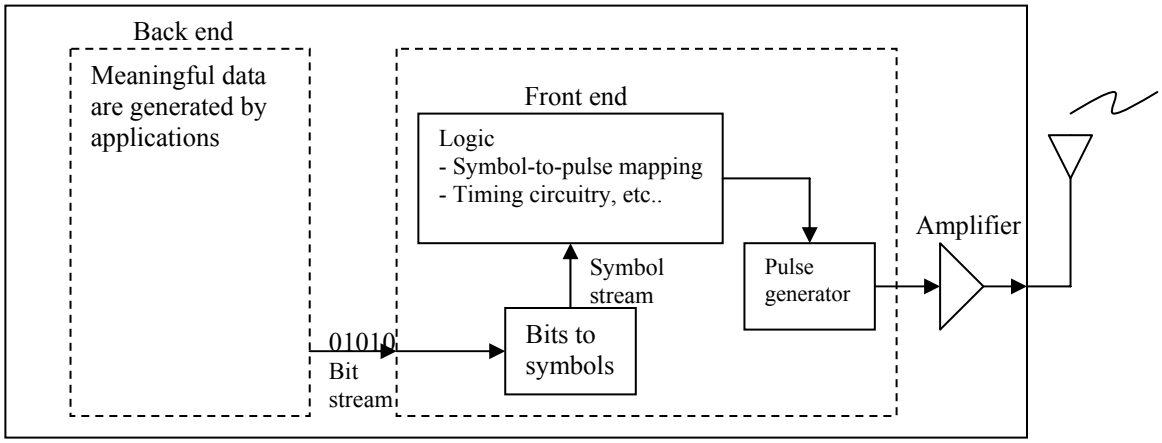

Figure 2-1. A general UWB transmitter block diagram.

First, meaningful data are generated by applications that are separate from the physical layer transmitter. Applications may be an email client or a web browser on a personal computer, a calendar application on a personal digital assistant (PDA), or a digital stream of data from a DVD player. This part of the wireless device is often called the “back end”.

This binary information stream is then passed to the “front end” of the transmitter. If higher modulation schemes are to be used, the binary information are mapped from bits to symbols, each symbol representing multiple bits. These symbols are then mapped onto an analog pulse shape which is generated by a pulse generator. Pulses can be optionally amplified before being passed to an antenna. Large gain of the amplifier is typically not required and may be omitted since the power spectral of UWB is limited. Precision timing circuitry is required to send the pulses out at specific intervals.

2.1.2 UWB Receiver Structure

A general UWB receiver block diagram is shown in Figure 2-2. The receiver performs the inverse operations of the transmitter to recover and pass the data to the “back end” applications.

There are two major differences between the transmitter and the receiver. One is that the receiver requires an amplifier to boost the power from the extremely weak received signal. The other is that the receiver must perform the functions of detection or acquisition to locate the desired pulse among the other signals and then continue tracking the desired pulses to compensate any mismatch between the clocks of the transmitter and the receiver.

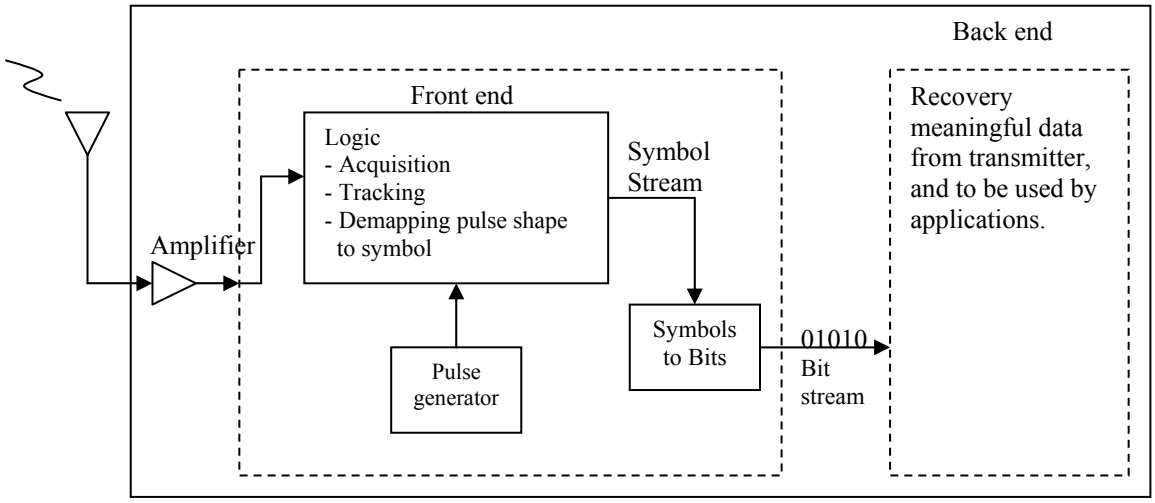

Figure 2-2. A general UWB receiver block diagram.

2.1.3 Generation of TH-PPM-UWB Signals

The properties of UWB have been already described in Chapter 1 which provide a foundation to build a simple UWB transmitter. The UWB system under investigating is a time-hopping pulse position modulation (TH-PPM-UWB) with a single reference 2nd order derivative Gaussian pulse shape *p(t)*. TH-PPM-UWB is most commonly used in the study of UWB. The system requires only a single template pulse for reception. Most of the complexity of this system resides in the providing an accurate timing for the generation of the transmitted sequence and subsequent reception. The TH-PPM-UWB signals to be generated can be schematized as shown in Figure 2-3 [28].

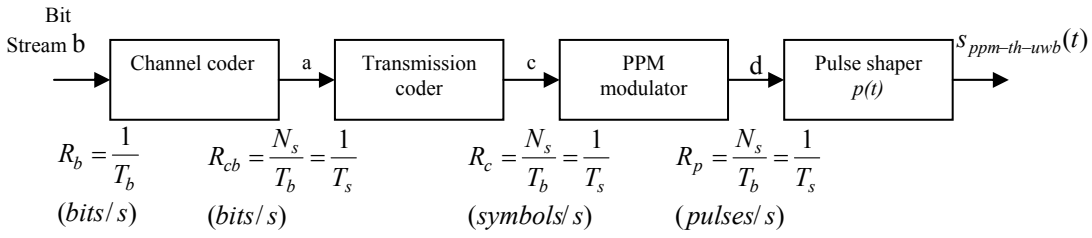

Figure 2-3. Transmission scheme for a TH-PPM-UWB.

Given the binary sequence b = (…, b_0, b_1…, b_k, b_{k+1} ….), generated at a rate of $R_b = \frac{1}{T_b}$ bits/s, the first block repeats each bit N_s times and generates a binary sequence (…, b_0, b_0, b_0…,b_1, b_1, b_1…, b_k, b_k, b_k.., b_{k+1}, b_{k+1}, b_{k+1} ….) = (…, a_0, a_1…, a_k, a_{k+1} ….) = a at a rate of $R_{cb} = \frac{1}{T_b}$ bits/s. This system introduces redundancy code is called a block coder indicated as channel coder in the Figure 2-3.

A second block called a transmission coder applies an integer-value code c= (…, c_0, c_1…, c_k, c_{k+1} ….) to the binary sequence a=(…, a_0, a_1…, a_k, a_{k+1} ….) and generates a new sequence d. The generic element of the sequence d is expressed as follows:

$$d_j = c_j T_c + a_j \varepsilon \qquad \textbf{(2- 1)}$$

where T_c and ε are constant terms that satisfy the condition $c_j T_c + \varepsilon < T_s$ for all c_j. In general, $\varepsilon < T_c$.

The coded real-valued sequence d enters a third block, the PPM modulator, which generates a sequence of unit pulses (Dirac pulses $\delta(t)$) at a rate of $R_p = N_s / T_b = 1/T_s$ pulses/s. These pulses are located at time $jT_s + d_j$, and are therefore shifted in time from nominal position jT_s by d_j. Pulses occur at times ($jT_s + c_j T_c + a_j \varepsilon$) where code c introduces a time hopping (TH) shift on the generated signal.

The last block is a pulse shape filter with impulse response *p(t)*. The impulse response *p(t)* must be such that the signal at the output of the pulse shaper filter is a sequence of non-overlapping pulses. The most commonly adopted pulse shapes is the second derivatives Gaussian waveform.

The signal *s(t)* at the output of the UWB transmitter can be expressed as:

$$s(t) = \sum_{j=-\infty}^{+\infty} p(t - jT_s - c_j T_c - a_j \varepsilon) \qquad \textbf{(2- 2)}$$

Note that the bit interval or bit duration (T_b) is the time used to transmit one bit, the relationship between bit duration and symbol duration expressed as $T_b = N_s T_s$, where N_s is the number of redundant bits. Also note that in Equation (2-2), the term $c_j T_c$ defines the pulse randomization or dithering with respect to the nominal instance of time occurring at multiples of T_s. Let η_j be a random TH dither, where $\eta_j = c_j T_c$, Equation (2-2) is now simplified as:

$$s(t) = \sum_{j=-\infty}^{+\infty} p(t - jT_s - \eta_j - a_j \varepsilon) \qquad \textbf{(2- 3)}$$

The signal in Equation (2-3) emits two different pulse shapes $p_o(t)$ and $p_1(t)$ in correspondence to the information bits "0" and "1". The following scenario generated TH-PPM-UWB signal using pseudo random number to generate a set of time-hopping (TH) code with a bit rate of 50 Mbps. In the case of Figure 2-4, the bit stream is [1 0] and the TH code is [2 1 2 2 1] with the time shift introduced by PPM is 0.5 ns and $N_s = 5$.

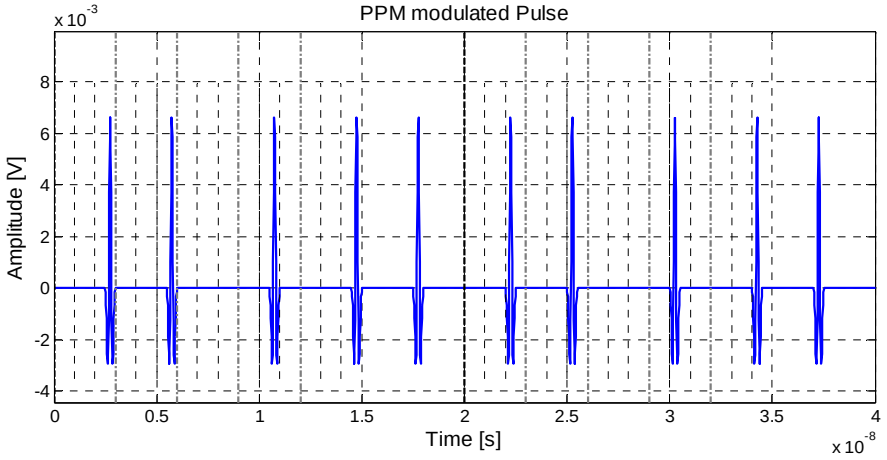

Figure 2-4. TH-PPM-UWB Signal.

The effects of TH-code and PPM shift factor are shown in Figure 2-5 and Figure 2-6. The pulse represents a bit "1" occupy within the five frames of the first half, while the pulse represents a bit "0" occupy within the five frames of the second half and so forth if the number of bit is larger than two. Since TH-code for the first frame is equal to 2, a pulse in the first frame must start at 2 and shifted by the PPM factor since the bit is equal to "1", this phenomenon is illustrated in Figure 2-5, the pulse starts at 2.5 ns. The unlike case for the bit equal to "0", a pulse starts according to the TH-code without applying the PPM shift factor as shown in Figure 2-6, the pulse starts at 2.2 ns. The power spectrum of a pulse is given in the next section.

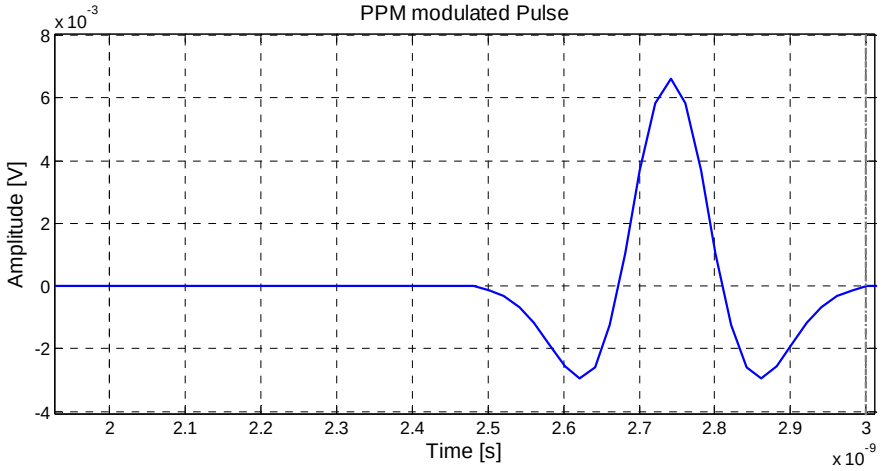

Figure 2-5. First frame of the first bit.

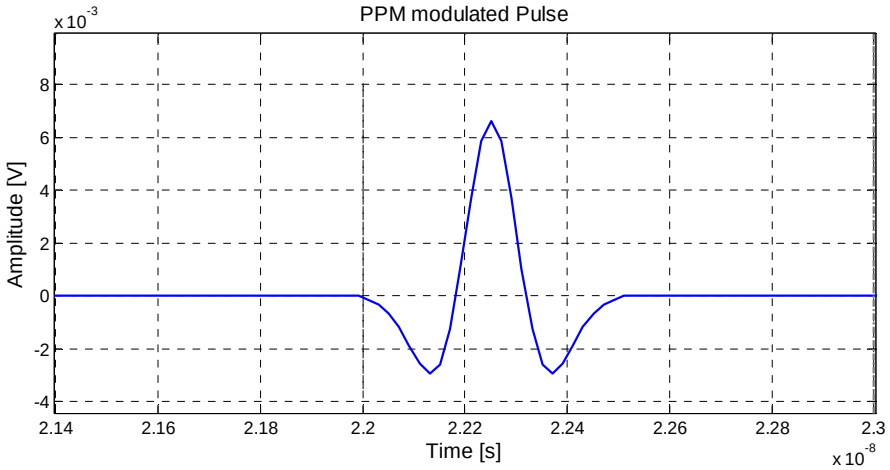

Figure 2-6. First frame of the second bit.

2.1.4 Power Spectral Density of the PPM Signal

The output of a TH-PPM-UWB modulator in its analog form is expressed as:

$$s(t) = \sum_{j=-\infty}^{+\infty} p(t - jT_s - \eta_j - a_j\varepsilon) \qquad \textbf{(2- 4)}$$

Similarly, given the modulating signal *m(t)*, the PPM pulse *x(t)* in its analog form consists of a train of identically shaped and non-overlapping pulses that are shifted from nominal instances of time T_s by the signal samples $m(kT_s)$. The expression of the PPM pulse in its analog form is given as:

$$x_{ppm}(t) = \sum_{j=-\infty}^{+\infty} p(t - jT_s - m(jT_s)) = p(t) * \sum_{j=-\infty}^{+\infty} \delta(t - jT_s - m(jT_s)) \qquad \textbf{(2- 5)}$$

Equation (2-5) is commonly known as the uniform sampling representation. A slightly different version of analog PPM, called the natural sampling, is obtained without explicit sampling of the modulating pulse *m(t)*. The two forms between PPM and TH-PPM, however, differ very little if the maximum shift is small compared to the pulse period T_s.

A sufficient condition for the pulse of Equation (2-5) to be strictly non-overlapping and the order of the pulses unaltered is:

$$p(t) = 0 \ \text{ for } |t| \geq \frac{T_s}{2} - |m(t)|_{\max} \text{ where } |m(t)|_{\max} \leq \frac{T_s}{2} \qquad \textbf{(2- 6)}$$

Power Spectral Density (PSD) of a PPM signal is difficult to calculate due to the non-linear nature of the PPM modulation. A complete derivation of this spectrum can be found in [29] and is based on various articles by Lehmann [30], Padgett [31] and Win [32]. Only the principle for generic periodic modulating signal of interested for understanding the spectrum of a TH-PPM-UWB results are to be discussed.

2.1.4.1 Power Spectral Density of the TH-PPM-UWB Signals

The difference between the two expressions TH-PPM-UWB

$$s(t) = \sum_{j=-\infty}^{+\infty} p(t - jT_s - \eta_j - a_j\varepsilon) \qquad \textbf{(2-7)}$$

and PPM-UWB signal

$$x_{ppm}(t) = \sum_{j=-\infty}^{+\infty} p(t - jT_s - m(jT_s)) = p(t) * \sum_{j=-\infty}^{+\infty} \delta(t - jT_s - m(jT_s)) \qquad \textbf{(2-8)}$$

is the $m(kT_s)$ process and the time dither process which incorporated the time shift introduced by the TH-code η and the time shift introduced by the PPM modulator ε.

Since ε is much smaller than η, it closely follows periodicity of the TH code. One can reasonably makes the first approximation and hypothesis that the effect of the ε shift on the PSD is not significant with respect to η. Therefore the signal of Equation (2-3) $s(t) = \sum_{j=-\infty}^{+\infty} p(t - jT_s - \eta_j - a_j\varepsilon)$ is modulated by a periodic signal and its PSD according to [33] is as the following

$$\begin{aligned} P_{x_{PPM}}(f) = \frac{1}{T_s^2} \sum_{m=-\infty}^{+\infty} \sum_{n=-\infty}^{+\infty} \sum_{l=-\infty}^{+\infty} \left| J_n\left(2\pi M\left(m\frac{1}{T_s} + nl\frac{1}{T_p}\right)\right)\right|^2 . \\ \left| P\left(m\frac{1}{T_s} + nl\frac{1}{T_p}\right)\right|^2 \left|\delta\left(f - \left(m\frac{1}{T_s} + nl\frac{1}{T_p}\right)\right)\right| \end{aligned} \qquad \textbf{(2-9)}$$

As indicated in (2-3), the PSD contains discrete frequency components located at the fundamental. PSD also contains components at the pulse repetition frequencies and their harmonics at linear combinations with respect to the fundamental frequency.

Note that the pulse repetition frequency $1/T_s = N_p/T_p$ is a multiple of the fundamental frequency of the periodic waveform therefore PSD is composed of lines occurring at N_p/T_p and the harmonics. The case $N_p = 1$ corresponds to the absence of coding, its PSD composed of line at $1/T_p$ and harmonics. The computed PSD for $N_p = 1$ is shown in Figure 2-7 [a, b]. It shows the power concentrates on the spectrum lines with the undesirable effect of presenting spectral line peaks. This phenomenon is not a surprise since the effect of ε is neglected.

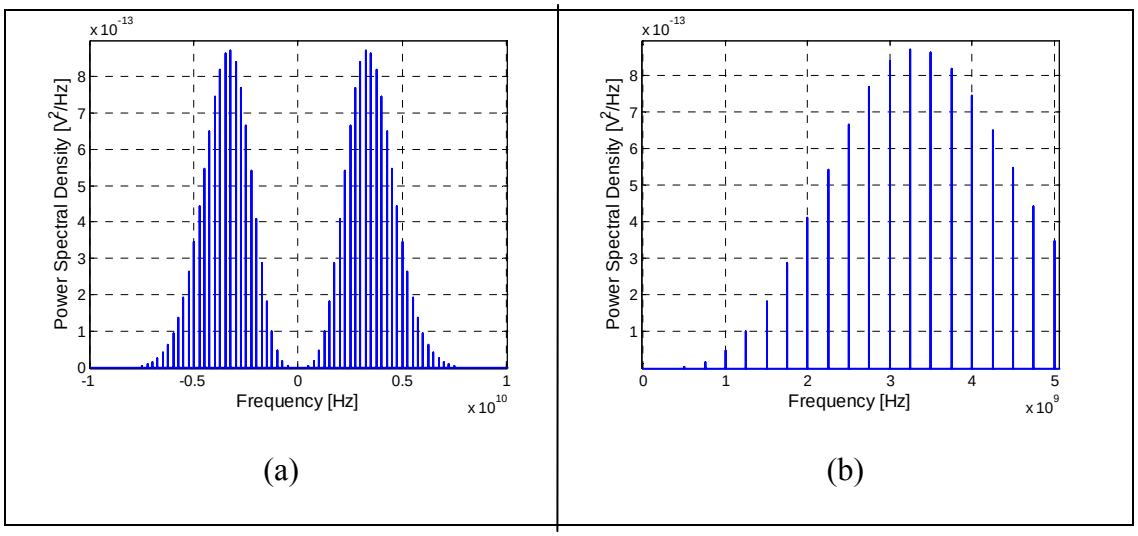

Figure 2-7. (a) PSD without PPM shift and no TH coding, (b) Zoom in version of (a).

The transmitted signal under investigation consists of five pulses per bit and the pulses are equally spaced in time with a pulse repetition period T_s. Since there is lacked of TH coding, all five pulses occupy at the same position inside each T_s interval. Each pulse has a second derivative Gaussian shape with a maximum length of 0.5 ns.

As expected, Figure 2-7a and Figure 2-7b are composed of spectral lines occurring at $1/T_s = 0.25$ GHz and the harmonics. The transmitted power is concentrated

at multiple of the pulse repetition frequencies. The envelop of the PSD has the shape of a Fourier transform of the second derivative Gaussian waveform.

In practice, N_p is set equal to N_s which is the period of the code coincides with the number of pulses per bit. The spectrum lines occur at $1/T_p$ and the harmonics, where $T_b = N_s T_s = N_p T_s$ is the bit interval. Although the spectrum is still discrete, spectrum lines occur at frequencies that are more crowded than in the previous case for the same bandwidth since $1/T_b < 1/T_s$.

The whitening effect[1] of the code is visible in over a large number of spectrum lines and spectral peaks are less accentuate. Subsequent analysis is on the dependencies of PPM time shift ε for the case when $N_s = N_p$.

First, let the signal $v(t)$ without ε effect be:

$$v(t) = \sum_{j=1}^{N_s} p(t - jT_s - \eta_j) \qquad \textbf{(2-10)}$$

taking the Fourier transform of $v(t)$ yields:

$$P_v(f) = P(f) \sum_{m=1}^{N_s} e^{-j(2\pi f(mT_s + \eta_m))} \qquad \textbf{(2-11)}$$

The corresponding generated PSD for Equation (2-11) is shown in Figure 2-8(a), and a close view of Figure 2-8 (a) is shown in Figure 2-8 (b).

[1] To eliminate the undesirable spectral peaks lines on the spectrum line.

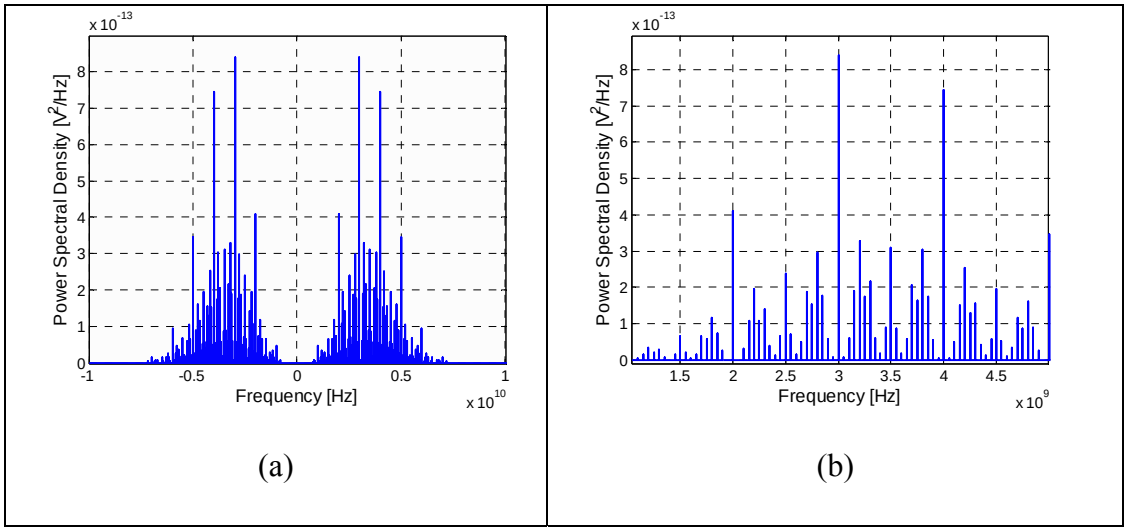

Figure 2-8. (a) PSD-Without PPM shift factor with TH coding, (b) Zoom in version of (a).

The spectral lines are located at a distance of $1/(N_s T_s) = 50\ MHz$. This indicates the transmitted power is concentrated at the multiples of the bit repetition frequency. This result is justified by the periodicity of the TH code, which coincides with N_s. The envelope of the PSD still resembles to the Fourier transform of the second order derivatives Gaussian waveform.

The comparison of the PSD with and without TH code verifies that the TH code having effect of diminishing the number of peaks with the highest power contribution since the same power is distributed over a larger number of spectral lines. This effect is more prominent when the values of N_s is further increased.

Now consider $v(t)$ as the basic multi-pulse used for transmission and apply the PPM shift factor ε, the new expression of $v(t)$ is:

$$\hat{v}(t) = \sum_{j=-\infty}^{+\infty} v(t - jT_b - \varepsilon b_j) \qquad \textbf{(2-12)}$$

The expression $\hat{v}(t)$ is represents a PPM modulated waveform in which the shift is ruled by the sequence of data symbols *b*. The assumption is that if *b* is a strict-sense-

stationary (SSS)[2] discrete random process and the different extracted random variables b_k are statistically independent with a common probability density function *w*, and from Rowe [34], the signal of Equation (2-10) has PSD in the form:

$$P_{\bar{v}}(f) = \frac{|P(f)|^2}{T_s}\left[1 - |W(f)|^2 + \frac{|W(f)|^2}{T_s}\sum_{n=-\infty}^{+\infty}\delta(f - \frac{n}{T_s})\right] \qquad \textbf{(2-13)}$$

where *P(f)* equals to the PSD of the multi-pulse given in Equation (2-9).

Giving the multi-pulse repetition rate T_b, the spectrum of the TH-PPM-UWB signal can be obtained as:

$$P_s(f) = \frac{|P_v(f)|^2}{T_b}\left[1 - |W(f)|^2 + \frac{|W(f)|^2}{T_b}\sum_{n=-\infty}^{+\infty}\delta(f - \frac{n}{T_b})\right] \qquad \textbf{(2-14)}$$

Equation (2-14) has double effects; one is on the TH code through $P_v(f)$ and the other is on the time shift introduced by the PPM modulator. The graphical illustration of TH-PPM-UWB PSD is shown in Figure 2-9. Note that the discrete component of the spectrum consists lines at $1/T_p$ and the amplitude of the lines is weighted by the statistical properties of the source represented by $|W(f)|^2$.

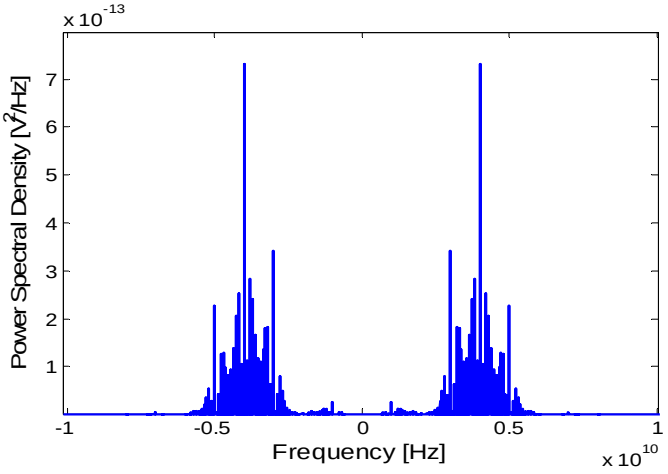

Figure 2-9. PSD - PPM shift factor with TH coding.

[2] The SSS of random process X(t) is to have characteristics that do not change as t varies.

The PSD in Figure 2-9 is composed of a continuous part and the spectral lines located at multiples of $1/T_p$. A comparison of the PSD in Figure 2-9 with the PSD in Figure 2-8 and Figure 2-7 shows the introduction of both TH coding and PPM distorts the orginal Gaussian shape of the PSD. Figure 2-10 also shows the PSD of the TH-PPM-UWB signal is fully contained within the envelope of the UWB PSD that results from the transmission of equally spaced pulses with the same shape, same average repetition frequency and same average power.

If p indicates the probability of emitting a bit "0" (no shift) and 1-p the probability of emitting a bit "1", then the amplitude of the PSD speak line becomes:

$$|W(f)|^2 = 1 + 2p^2(1-\cos(2\pi f\varepsilon)) - 2p(1-\cos(2\pi f\varepsilon)) \qquad \textbf{(2-15)}$$

If the source emits equiprobable[3] symbols "0" and "1" then Equation (2-13) can be simplified as:

$$|W(f)|^2 = \frac{1}{2}(1+\cos(2\pi f\varepsilon)) \qquad \textbf{(2-16)}$$

Since the time shift is small, the discrete components dominate the spectrum.

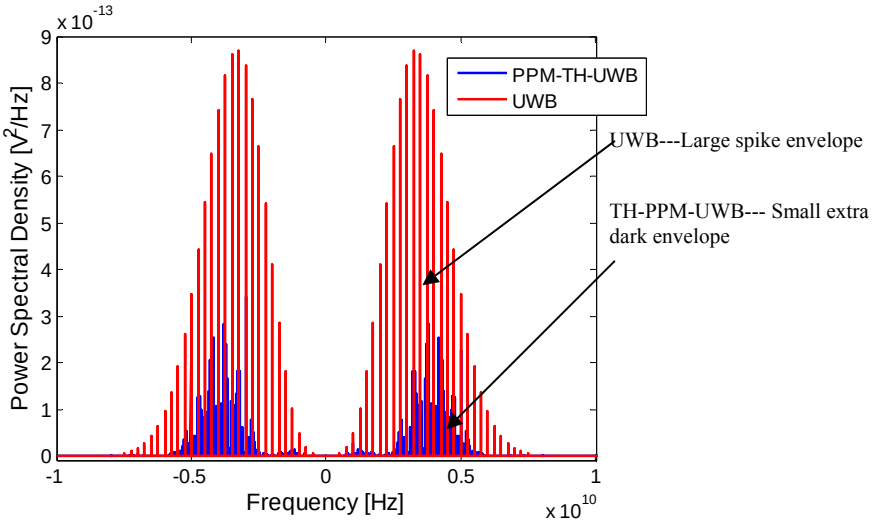

Figure 2-10. Comparison between PPM-TH-UWB and UWB.

[3] The generation of bit "0" and bit "1" has equal chance.

When N_p is larger than N_s, the above effect is more prominent. If N_p is not a multiple of N_s then several spectral lines generated by linear combination of $1/T_p$ and $1/T_s$ will fill up the power spectrum. The filled up power spectrum makes the PSD spectral lines smooth and this phenomenon is called the smoothing effect.

The extreme case when $N_p \to \infty$ corresponds to a lack of periodicity in the TH-PPM-UWB signal is represented by Equation (2-3). The time dither process can be assimilated to the random modulating signal $m(kT_s)$ and its power spectrum is given by [35]:

$$P(f) = \frac{|P(f)|^2}{T_s}\left[1 - |W(f)|^2 + \frac{|W(f)|^2}{T_s}\sum_{n=-\infty}^{+\infty}\delta\left(f - \frac{n}{T_s}\right)\right] \quad \textbf{(2-17)}$$

where $W(f)$ is the Fourier transform of the probability density w and coincides with the characteristic function of w evaluated at $-2\pi f$, where f is the frequency of the pulse:

$$W(f) = \int_{-\infty}^{+\infty} w(s)e^{-j2\pi fs}ds = \left\langle e^{-j2\pi fs}\right\rangle = C(-2\pi f) \quad \textbf{(2-18)}$$

Equation (2-17) shows that the spectrum of a random modulating PPM signal is composed of a continuous portion controlled by the term $1 - |W(f)|^2$ and a discrete portion formed by line components at frequency $1/T_s$ (i.e., at the pulse repetition frequency and harmonics).

Since $W(f)$ is the Fourier transform of a probability density function, its value at "0" is "1", that is $W(0) = 1$. Therefore, the continuous component of the spectrum is

zero at frequency zero and rises at higher frequencies. The discrete components that are weighted by $|W(f)|^2$ increase at low frequencies and decrease at high frequencies.

The following discussion will be examined the properties of NB signal.

2.2 The WLAN based OFDM Systems

A narrowband system consists of a transmitter sending a narrowband signal to a receiver through a dispersive Rayleigh-fading environment. Each of these components and the power spectral density of the signal is to be examined in detail to set the base for the narrowband detection and elimination.

2.2.1 IEEE 802.11a OFDM WLAN Transmitter Structure

A typical IEEE 802.11a OFDM WLAN transmitter structure is shown in Figure 2-11. The stream of complex valued sub-carrier modulation symbols at the output of the mapper is divided into groups of data sub-carrier. Each group is transmitted in an OFDM symbol. All data contains in OFDM symbols is carried by a data carrier and reference information is conveyed in the pilot carriers.

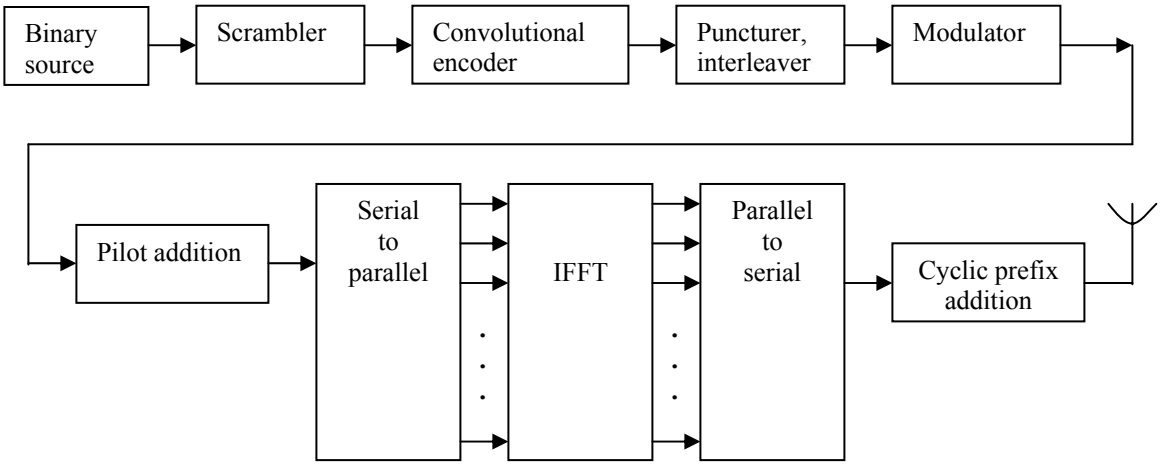

Figure 2-11. Block diagram of a typical OFDM transmitter (IEEE 802.11a Standard).

There are N_{SD} data sub-carriers and N_{SP} pilots sub-carrier for each symbol. Each symbol is constituted by a set of sub-carrier (N_{ST}) and transmitted with a duration T_S. This symbol interval consists of two parts: a useful symbol with duration T_U and a cyclic prefix with duration T_{CP}. The cyclic prefix is a copy of the last T_{CP} /T samples of the symbol part and attached in front of the symbol part when the symbol is sent. For the cyclic prefix length T_{CP} there are two possible values in the HIPERLAN/2 system: mandatory 800 ns and optional 400 ns guards. The 800 ns guard interval is sufficient to allow good performance in channels with a delay spread up to 250 ns. The 400 ns guard interval can be used for communication in small indoor environment. Numerical values for the OFDM parameters are given in *Table 2-1* [36].

Table 2-1. OFDM parameters

Parameter	Value	
Sampling rate f_s=1/T	20 MHz	
Useful symbol part duration T_U	64*T (3.2 μs)	
Cyclic prefix duration T_{CP}	16*T	8*T
Symbol interval T_S	0.8 μs (mandatory) (optional) 4.0 μs (T_U + T_{CP})	0.4 μs 3.6 μs (T_U + T_{CP})
Number of data sub-carriers N_{SD}	48	
Number of pilot sub-carrier N_{SP}	4	
Total number of sub-carrier N_{ST}	52 (N_{SD} + N_{SP})	
Sub-carrier spacing Δ_f	0.3125 MHz (1/ T_U)	
Spacing between the two outmost sub-carriers	16.25 MHz (N_{ST} * Δ_f)	

The answer to the question how to design a receive mechanism for the corresponding transmitter is covered in the following.

2.2.2 IEEE 802.11a OFDM WLAN Receiver Structure

At the front-end of the receiver, OFDM signals are subject to synchronization errors due to oscillator impairments and sample clock differences. The demodulation of the received radio signal to baseband, possibly via an intermediate frequency, involves

oscillators whose frequencies may not be perfectly matched with the transmitter frequencies. This results in a carrier frequency offset. Figure 2-12 illustrates the front end of an OFDM receiver where synchronization errors can occur.

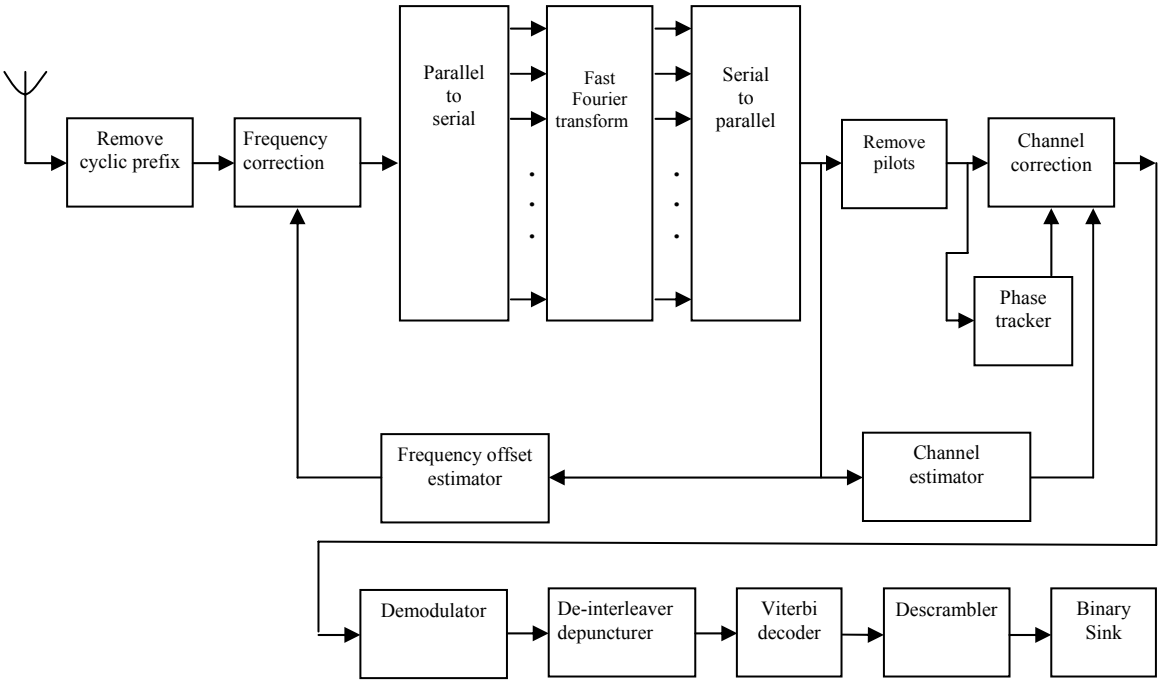

Figure 2-12. Block diagram of a typical OFDM receiver (IEEE 802.11a Standard).

In addition, demodulation usually introduces phase noise acting as an unwanted phase modulation of the carrier wave. Carrier frequency offset and phase noise degrade performance of the OFDM system. When baseband signals are sampled at the A/D converter, the sample clock frequency at the receiver may not be the same as the one at the transmitter. Not only this sample clock offset causes errors, it also makes duration of an OFDM symbol at the receiver to be different from that at the transmitter. If the symbol clock is taken from the sample clock then variations in the symbol clock will occur. Since the receiver needs to determine when the OFDM symbol begins for proper demodulation with the FFT, a symbol synchronization algorithm at the receiver is

usually necessary. Symbol synchronization also compensates for delay changes in the channel.

Channel estimation in OFDM is normally performed with the aid of pilot symbols. Since each subcarrier is flat fading, techniques from single-carrier flat fading systems are directly applicable to OFDM. In OFDM system, the pilot-symbol assisted modulation (PSAM) on flat fading channels involves the sparse insertion of known pilot symbols in the stream of data symbols. Attenuation of the pilot symbols is measured and the attenuations of the data symbols in between these pilot symbols are typically estimated/interpolated using time-correlation properties of the fading channel. After successfully achieving synchronization, the OFDM signals are passed onto the demodulator, de-interleaver and finally to the Viterbi decoder.

The distinction between UWB and OFDM signals is not only on the signal itself but also on the structure and complexity that each signal inherited. In the next several sections, detailed analysis for OFDM signal will be derived in mathematical representation, generating signal in time domain and power spectral density (PSD). The impact of NB onto the UWB is also investigated.

2.2.3 Generation of IEEE 802.11a OFDM WLAN Signals

In general, OFDM system subdivides its available bandwidth into smaller frequency bands. For each sub-band, different types of modulation can be adopted for data transmission and the IR method certainly cannot be applied. The most popular criterion, which has already studied in the IEEE 802.11a is based on the well-known Orthogonal Frequency Division Multiplexing (OFDM) method. Conceptually, OFDM

technique consists of the parallel transmission of several signals that are modulated at different carrier frequencies f_m.

The sequence binary bit stream forms the input of the OFDM modulator and is sub-divided into groups of K bits used to generate blocks of N symbols $\{d_o,.....,d_m,.....d_{N-1}\}$. The generic d_m assumes one of L possible values, which is $K = N\log_2 L$. The symbols are then in turn modulated with different carriers. To transmit the N symbols of a block in parallel, the signals modulating different carriers must be orthogonal in frequency (i.e., the cross products of these carriers are equal to zero). If T_o is the time used to transmit each symbol on the corresponding carrier, the orthogonality among different transmissions can be achieved by adopting $\nabla f = 1/T_o$, where ∇f is the equally spaced carrier. In addition, a time guard interval T_G is introduced between transmission of the subsequent blocks to prevent Inter-Symbol Interference (ISI). The total OFDM symbol duration is thus $T = T_o + T_G$ leading to a maximum symbol rate of

$$R_S = \frac{N}{T} = \frac{N}{T_o + T_G} \qquad \textbf{(2-19)}$$

The length of the guard interval is usually about 20-30% of the total symbol duration T. In general, the guard interval is used to transmit a copy of the final border section of the OFDM symbol. This guard is known as a cyclic prefix. The prefix is introduced to maintain carrier synchronization at the receiver in the presence of time-dispersive channels. The length of the cyclic prefix is obviously limited by the duration of the guard interval. At the receiver end, the cyclic prefix is firstly removed.

All modulators use the same rectangular shape $g_T(t)$ of finite duration T such that:

$$g_T(t) = \begin{cases} \sqrt{1/T} & -\mathrm{T_G} \le \mathrm{t} \le \mathrm{T_o} \\ 0 & \text{elsewhere} \end{cases} \qquad \textbf{(2-20)}$$

If $c_m = a_m + jb_m$ indicates the point in the constellation associated with symbol d_m, the OFDM signal corresponding to a block of *N* symbols is given by:

$$x(t) = g_T(t)\sum_{m=0}^{N-1}\left(a_m \cos(2\pi(f_p + f_m)t + \phi) - b_m \sin(2\pi(f_p + f_m)t + \phi)\right) \qquad \textbf{(2-21)}$$

and the corresponding complex envelope is:

$$\bar{x}(t) = g_T(t)\sum_{m=0}^{N-1} c_m e^{j2\pi f_m t} \equiv \sum_{m=0}^{N-1} c_m \varphi_m(t) \equiv g_T(t)S(t) \qquad \textbf{(2-22)}$$

in which $\varphi_m(t) = g_T(t)e^{j2\pi f_m t}$ and *S(t)* is a periodic function of period T_o.

The simplest way to implement an OFDM modulator is to adopt a digital structure using Discrete Fourier Transform (DFT) [37]. From [38], the transmission of a sampled version of the complex envelope in Equation (2-22) is:

$$\bar{x}[n] = \bar{x}(nt_c) = g_T(nt_c)\sum_{m=0}^{N-1} c_m e^{j2\pi f_m t_c} \qquad \textbf{(2-23)}$$

where t_c is the sampling period. According to Equation (2-21), *x(t)* consists of the parallel transmission of *N* signals with frequency occupancy of $2\nabla f$. It is reasonable to assume that the complex envelope in Equation (2-22) occupies frequencies in the range (-R,R), where $R = N\nabla f / 2$. The complex envelope of the OFDM signal can therefore be represented by samples taken at multiples of $t_c = T_o / N$.

$$\bar{x}[n] = g_T(nt_c)\sum_{m=0}^{N-1} c_m e^{j\frac{2\pi f_m n T_o}{N}} \qquad \textbf{(2-24)}$$

Let $f_m = m\nabla f - (N/2)$ and $\nabla f = m/T_o - N/(2T_o)$ and substitute into Equation (2-24);

$$\bar{x}[n] = g_T(nt_c)\sum_{m=0}^{N-1} c_m e^{j\frac{2\pi mn}{N}} e^{-j\pi n} = g_T(nt_c)(-1)^n \sum_{m=0}^{N-1} c_m e^{j\frac{2\pi mn}{N}} \quad \textbf{(2-25)}$$

The summation in Equation (2-25) corresponds to the *n-th* element of vector C representing the Inverse Discrete Fourier Transform (IDFT) of the vector $\{c_o,....,c_n,....c_{N-1}\}$ which can be represented as:

$$\bar{x}[n] = g_T(nt_c)(-1)^n C_n \quad \textbf{(2-26)}$$

Equation (2-26) indicates that the samples of the complex envelope of Equation (2-21) can be obtained by computing the IDFT of a set of points of the coefficients $\{c_o,....,c_m,...c_{N-1}\}$, which yields the IDFT sequence $\{c_o,....c_j,....c_{N-1}\}$. As per suggestion in [39], the serial transmission of the sequence in Equation (2-26) does not allow the reproduction of a real OFDM signal since the absence of over sampling would introduce intolerable aliasing when passing this sequence to the digital-to-analog converter. A solution to this problem is to introduce zero padding within the input sequence $\{c_o,....,c_m,...c_{N-1}\}$ before computing the IDFT.

Since the IDFT is a periodic sequence with period *N*, the introduction of a cyclic prefix in the digital domain is performed by simply appending the last $N_G = T_G/t_c$ elements of the original sequence in Equation (2-26) to the beginning of the sequence itself.

Figure 2-13 shown the first OFDM symbol which is acquired from the parameters setting in Table 2-2.

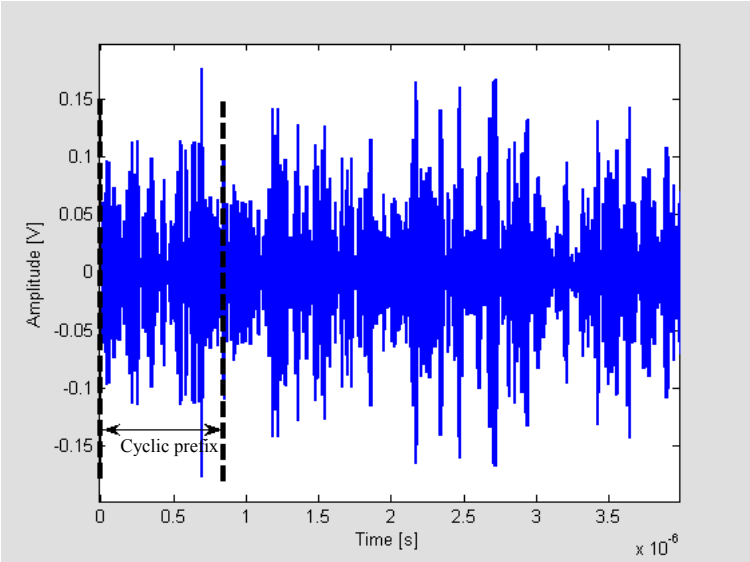

Figure 2-13. First OFDM symbol.

Table 2-2 : Key parameters of IEEE 802.1a OFDM wireless local area network.

Parameter	Value
Data rate	48 Mbps
Modulation	QPSK
Subcarriers	52
Pilot tones	4
Symbol duration	4 μs
Subcarrier spacing	312.5 KHz
Signal bandwidth	16.66 MHz

The non-impulsive nature of the OFDM signal has a bandwidth occupation about 17 MHz. Figure 2-13 also highlights the presence of the cyclic prefix at the beginning of the transmitted symbol. Spectral analysis of OFDM signal will be described in the subsequent section.

2.2.4 Power Spectral Density of the OFDM Based WLAN Signals

It is shown in (Section 2.2) that a sampled version of the complex envelope of the OFDM can be obtained by computing the IDFT of a sequence of the complex symbols $\{c_0,.....,c_j,....c_{N-1}\}$ which modulate the in-phase and in-quadrature carriers. The n-th (i.e., n must be an integer) element C_n of vector C representing the IDFT of $\{c_0,.....,c_j,....c_{N-1}\}$ is used to generate the n-th sample of $\bar{x}_k(t)$. The formation of the generic coefficient C_n is:

$$C_n = \sum_{m=0}^{N-1} c_m e^{j2\pi\frac{nm}{N}} \qquad \textbf{(2-27)}$$

The complex envelope of the signal corresponds to the set of OFDM symbols can be expressed as:

$$\bar{s}(t) \equiv \sum_{m=0}^{N-1} \bar{x}_n(t-nT) \qquad \textbf{(2-28)}$$

The hypothesis that the quantities C_n having a complex Gaussian distribution is based on the central limit theorem and on the expression (2-25). This hypothesis is valid if the number of sub-carrier N is sufficiently large. According to Gaussian properties, the expectation of C_n is zero. This implies all C_n are uncorrelated and since it is Gaussian, all C_n are independent and have the same variance σ_C^2. The total power $P_{\bar{s}}$ of $\bar{s}(t)$ is now can be computed as:

$$P_{\bar{s}} = \sigma_C^2 = \sum_{j=0}^{N-1} \sigma_{c_j}^2 \qquad \textbf{(2-29)}$$

Power spectrum density of the OFDM signal of Equation (2-29) can be computed by first introducing a random phase epoch Θ, uniformly distributed in $[0,T]$, then Equation (2-28) becomes:

$$\bar{s}(t) \equiv \sum_{m=0}^{N-1} \bar{x}_n(t - nT + \Theta) \qquad \textbf{(2-30)}$$

PSD of Equation (2-30) can be derived by first computing the autocorrelation function of $\bar{s}(t)$ and then taking the Fourier transform of the calculated autocorrelation function.

The complex envelope of an OFDM symbol defined in Equation (2-22) is rewritten here by introducing a rectangular window of duration T, where T is the OFDM symbol duration.

$$\bar{x}(t) = rect(\frac{t}{T}) \sum_{m=0}^{N-1} c_m e^{j2\pi f_m t} \qquad \textbf{(2-31)}$$

Equation (2-31) indicates that the spectrum of an OFDM symbol is a $\sin(x)/x$ function corresponding to the Fourier transform of the rectangular window, convolved with a sequence of Dirac pulses located at the sub-carrier frequency f_m. After the cyclic prefix is removed at the receiver, the spectrum centered on the m-th sub-carrier (f_m) can be expressed as:

$$P_{f_m}(f) = \frac{\sin(\pi T_o(f - f_m))}{\pi T_o(f - f_m)} = \frac{\sin\left(\frac{\pi(f - f_m)}{\nabla f}\right)}{\frac{\pi(f - f_m)}{\nabla f}} \qquad \textbf{(2-32)}$$

By extending spectrum expression in (2-32), the spectrum of OFDM in Equation (2-30) becomes:

$$P_{f_m}(f) = P_{\bar{s}} \sum_{m=0}^{N-1} \frac{\sin\left(\frac{\pi(f-f_m)}{\nabla f}\right)}{\frac{\pi(f-f_m)}{\nabla f}} \qquad \textbf{(2-33)}$$

The following two figures serve as the verification of the above PSD derivation. Figure 2-14 (a,b) shows the PSD of WLAN based OFDM signal which has central frequency at 5.2 GHz and a bandwidth equals to 16.7 MHz.

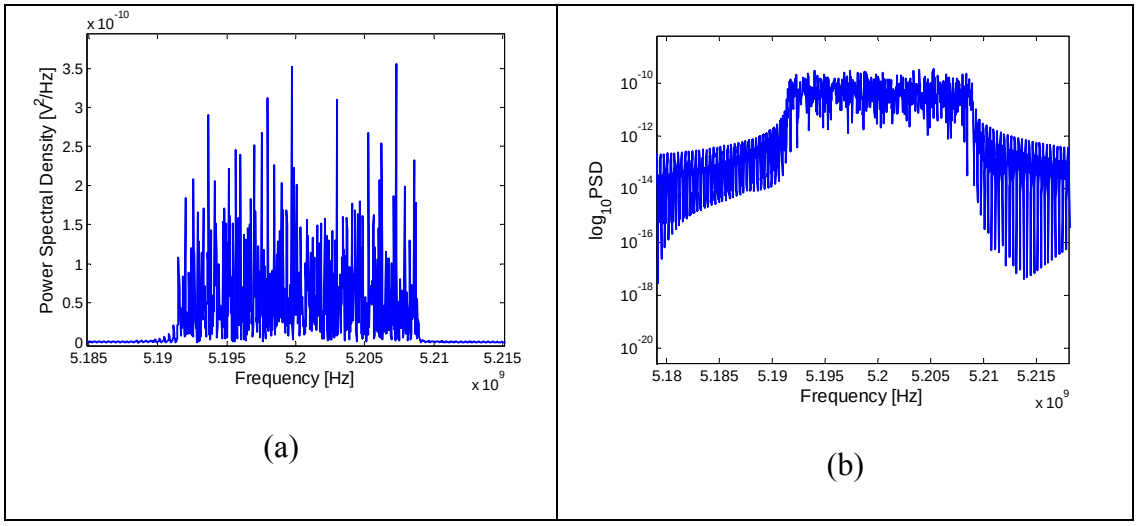

Figure 2-14. (a) PSD of the WLAN based OFDM signal, (b) PSD of WLAN based OFDM signal in logarithmic scale

Note that when comparing the bandwidth of NB, which is about 16 MHz to 3.6 GHz of the UWB, the former bandwidth is extremely small, and thus, NB signal can be treated as a tone in UWB system [25]. The impact of the NB onto the UWB systems is to be investigated in the following.

2.3 Impact of Narrowband Interference on a UWB Signal

The impact of NBI on single user UWB systems was studied in [5], [6], [7], [9], [10], [13], [40]. A DS-CDMA system is shown to resist NBI from IEEE 802.11a OFDM signals [14], where the NBI was modeled as the multiple access interference (MAI). The use of a maximal ratio combiner (MRC) can suppress MAI but not NBI [12]. Bit error

rate (BER) expressions were derived in [16] for a multi-user time hopping (TH) system operating over a pure AWGN channel (i.e., NBI is not present). These can be used as a benchmark to study the performance of NBI suppression schemes.

Many UWB radios use time-hopping to accommodate multiple users and randomize collisions in asynchronous case. Time-hopping prevents complete collision of pulse trains when users are synchronized.

Individual UWB pulse may have little energy, multiple pulses are transmitted for each data symbol is preferable. The multiple pulse train represents TH-PPM-UWB is

$$s(t) = b_{j,u}\sqrt{E_p}\sum_{j=-\infty}^{+\infty} p(t - jT_s - \eta_j - a_j\varepsilon) \qquad \textbf{(2-34)}$$

where $b_{j,u}$ denotes the j-th binary bit in the UWB stream and E_p denotes the energy per pulse. The energy per UWB bit is $N_s E_p$ where N_s is the number of redundant bit. The received signal during the j-th UWB symbol is

$$y_j(t) = x_j(t) + w_j(t) + i_j(t) \qquad \textbf{(2- 35)}$$

where $w_j(t)$ denotes additive white Gaussian noise (AWGN) with two-sided psd $N_o/2$ and $i_j(t)$ is interference.

According to [41], in AWGN environment, the optimal receiver for UWB communications is a match filter (MF) which matches to the symbol waveform, the pulse match symbol is

$$p_s(t) \cong \sum_{j=0}^{N_s-1} p(t - jT_s - \eta_j - a_j\varepsilon) \qquad \textbf{(2- 36)}$$

and the corresponding decision statistic is

$$\begin{aligned} Z_j &= \sum_{j=0}^{N_s-1}\int_0^{T_p} p(t)x_j(t + jN_cT_p)dt \\ &= S_j + W_j + I_j \end{aligned} \qquad \textbf{(2- 37)}$$

where S_j, W_j, and I_j denote UWB signal, noise, and interference components. Because the pulse *p(t)* has unit energy then the UWB signal is

$$S_j = b_{j,u}\sqrt{E_p}N_s \qquad \textbf{(2- 38)}$$

The noise term W_j is zero-mean Gaussian with a variance equals to $N_s N_o / 2$.

The interference term I_j represents aggregating effect of the modulated narrow-band signals. Assume the interference as a single tone since its bandwidth is sufficiently small compared to the UWB bandwidth, let f_i, R_i, and P_i denote the carrier frequency, rate, and power of the interferer single tone. The received signal component of the interference is expressed as

$$i_i(t) = \sqrt{2P_i}\cos(2\pi f_i t + \theta_i)\sum_{j=-\infty}^{+\infty}\bar{b}_j g_i(t - jT_i - \tau_i) \qquad \textbf{(2-39)}$$

where

- $\bar{b}_i$ is the transmitted symbol, the symbol set is normalized so that $E\left\{\left|\bar{b}_i\right|^2\right\}=1$.
- $g_i(t)$ is the normalized NBI transmit pulse shape normalized with $\frac{1}{T_i}\int_0^{T_i} g^2(t)dt = 1$.
- θ_i and τ_i denote the random carrier phase and delay. Phase $\theta_i \sim U[0,2\pi)$[4] and $\tau_i \sim U[0,T_i)$.

Because the UWB signal is time-hopping, there is a random time-offset between successive pulses of the same bit. Hence, the starting phase of the NBI carrier changes randomly from the time associated with the beginning of one pulse to that of the next. Giving a pulse duration T_p and an NB symbol duration $T_i = 1/R_i$, the probability of a

[4] "~" equivalent to uniformly distributed, "[" equivalent to inclusive and ")" equivalent to "exclusive".

symbol transition within an UWB pulse is given by T_p / T_i. From [41], the interference component is calculated as:

$$I_j = \sqrt{\frac{P_i}{2} \sum_{j=0}^{N_s-1} \bar{b}_j [P(f_i) e^{-j\phi_j} + P^*(f_i) e^{j\phi_j}]} \quad \textbf{(2-40)}$$

For a symmetric pulse shape, $P(f) = P(-f)$ is real valued and interference becomes:

$$I_j = \sqrt{\frac{P_i}{2}} \sum_{j=0}^{N_s-1} \bar{b}_j P(f_i) \cos(\pi f_c T_p + \psi_j) \quad \textbf{(2-41)}$$

The phase variable ψ_j is random in nature and uniformly distributed from [0 to 2π]. According to [40], the worse impact on UWB system from NB system is when both central frequencies are equal and less impact from NB system onto the UWB when their central frequencies are further apart. The simulation results for which central frequency equals to 4.5 GHz and 5.2 GHz for UWB and NB respectively are available in chapter 5.

2.4 Summary

In this chapter, the time-hopping pulse position technique is applied into the 2nd derivative Gaussian pulse to generate an UWB signal. The convention name for UWB signal utilizing time-hopping pulse position technique is the TH-PPM-UWB signal.

The uncoded PPM-UWB signal leaks its energy between its symbols as well as other NB existing systems. The large number of peaks in the power spectral density of uncoded PPM-UWB indicates the power dispersion. If the leaked energy is above a defined limit, the PPM-UWB signal causes an unacceptable amount of inter-symbol interference (ISI) which greatly degrades the UWB system performance and would hurt other existed NB services within the UWB operating frequency band. To alleviate the

leaking problem and to enhance the performance of UWB system, the randomness coding technique is introduced into the system called time-hopping (TH) coding. The coded TH-PPM-UWB reduces the peak value and smoothes out UWB signal PSD.

The narrowband model IEEE 802.11a is a wireless local access network (WLAN) based on OFDM modulation technique. The IEEE 802.11a divides its available bandwidth into smaller sub-bands and uniquely OFDM modulates each sub-band. The orthogonal in frequency is used to eliminate ISI. The calculated bandwidth of IEEE 802.11a signal is very small compared to the bandwidth of the TH-PPM-UWB signal.

The impact of NB signal onto UWB signal depends on two factors, one is the power level of the NB signal and the other is the spacing between two central frequencies. The poor UWB performance affected by NB is the case when power of NB is higher compared to the UWB power or both central frequencies are close to each other.

Chapter 3 Narrowband Detection in Ultra Wideband Systems

From practical perspective NB is not always active, therefore it is worth to detect the presence of NB and turn on an eliminator to cancel the negative effect of NB on UWB to improve system performance. This chapter provides mathematical analysis and simulation results in the detection of a NB in the UWB systems. One of the best detection methods is the use of an spectrogram.

3.1 The Spectrogram

The spectrogram can be understood as a power spectral density (PSD) estimation. As shown in [42], the spectrogram of the signal $f[n]$ is specified as

$$I_{n_o}^{(f)} \cong \left| \sum_{n=0}^{N-1} f[n-n_o] \exp\left(-j2\pi \frac{k}{N} n \right) \right|^2 \qquad \textbf{(3-1)}$$

where n_o denotes the start of the observation interval of length N, which is used to estimate the PSD, k represents a frequency identifier. The actual frequency under calculation is equal to k/N and its frequency resolution is equal to $1/N$ which will be computed for $k \in \{0,1,....N/2-1\}$. The successful NB detection at frequency k at time n_o (i.e., (k,n_o)) when the spectrogram value at (k,n_o) is larger than the overall average power. Here, a threshold detector is built which reports detection in the frequency range

where the narrowband is located. The rest of the discussion addresses in detail statistical properties and detection results.

3.2 Statistical Properties of a Spectrogram

An alternative form to represent expression (3-1) is

$$I_{n_o}^{(f)} \cong \left(X_{n_o}^{(f)}[k]\right)^2 + \left(Y_{n_o}^{(f)}[k]\right)^2 \qquad \textbf{(3-2)}$$

where,

$$X_{n_o}^{(f)}[k] \cong \sum_{n=0}^{N-1} f[n-n_o]\cos(\frac{2\pi k}{N}n)$$

$$Y_{n_o}^{(f)}[k] \cong \sum_{n=0}^{N-1} f[n-n_o]\sin(\frac{2\pi k}{N}n)$$

In this study, the incoming signal $f[n]$ consists of three terms, an UWB signal $y[n]$, a noise signal $x[n]$ and the NB signal $s[n]$ which are assumed all random in nature. Since $X[k]$ is the sum of N random variables (RV), it is reasonable to assume that $X[k]$ is a RV having Gaussian distribution characteristics given that N is extremely large, likewise for $Y[k]$. As the results, $I[k]$ is a RV by summing up the square of υ, in which υ is an Independent and Identical Distribute (I.I.D) Gaussian RV, where υ=1 if k=0, else υ=2. In either case, $I[k]$ has a chi-squared distribution which is given by:

$$\begin{cases} p(x;\lambda;\beta;\upsilon) = \dfrac{1}{2\beta}\left(\dfrac{x}{\lambda}\right)^{\frac{\upsilon-2}{4}} \exp\left[-\dfrac{x+\lambda}{2\beta}\right] I_{\frac{\upsilon-2}{2}}\left(\dfrac{\sqrt{\lambda x}}{\beta}\right) & \text{x} \geq 0 \\ p(x;\lambda;\beta;\upsilon) = 0 & \text{x} < 0 \end{cases} \qquad \textbf{(3-3)}$$

where $I_r(u)$ denotes the modified Bessel function of the first kind and order r. More over, λ, β and υ denote the non-centrality, scale and shape parameters of the chi-square distribution function $p(.)$.

The values of λ, β and υ depend on both the mean and the variance of $X[k]$ and $Y[k]$ according to:

$$\begin{aligned} \lambda[k] &= E\{X[k]\}^2 + E\{Y[k]\}^2 \\ \beta[k] &= \text{var}\{X[k]\} + \text{var}\{Y[k]\} \\ \upsilon &= 2 - \delta[k] \end{aligned} \quad \textbf{(3-4)}$$

It is reasonable to assume that the three terms forming the signal $f[n]$ are statistically independent, such that

$$\begin{aligned} E\{X[k]\} &= E\{X^{(y)}[k]\} + E\{X^{(x)}[k]\} + E\{X^{(s)}[k]\} \\ E\{Y[k]\} &= E\{Y^{(y)}[k]\} + E\{Y^{(x)}[k]\} + E\{Y^{(s)}[k]\} \end{aligned} \quad \textbf{(3- 5)}$$

Consequently, the expectation of expression (3-2) is equal to

$$E\{I[k]\} = \lambda[k] + \beta[k] \quad \textbf{(3-6)}$$

where,

$$\begin{aligned} \lambda[k] &= \left(\sqrt{\lambda^{(y)}[k]} + \sqrt{\lambda^{(x)}[k]} + \sqrt{\lambda^{(s)}[k]}\right)^2 \\ \beta[k] &= \beta^{(y)}[k] + \beta^{(x)}[k] + \beta^{(s)}[k] \end{aligned} \quad \textbf{(3-7)}$$

When comparing the bandwidth of NB and UWB in chapter 2, the former is considerable small and can be treated as a tone. For simplification in term of mathematical analysis, let the tone interferer signal be

$$\tilde{s}[n] = \sqrt{2E_s}\cos\left(\frac{2\pi k_n}{N} + \varphi\right) \quad \textbf{(3- 8)}$$

in which E_s, k_n, and φ denote average power, frequency and phase of the interferer.

Individual signals statistically identified from $f[n]$ are available in the next three subsections.

3.2.1 TH-PPM-UWB Signals in the Spectrogram

The TH-PPM-UWB signal term in $f[n]$ is described by

$$y[n] = \sqrt{E_p} \sum_j \delta[n - jT_s - c_j - \theta] \qquad \textbf{(3- 9)}$$

where $\sqrt{E_p}$ stands for energy per pulse, θ is a RV with distribution $P(\theta = \varsigma) = T_s$, whereas $T_s = \frac{1}{N_h}$, N_h is the cardinality of the pseudorandom to generate the TH code, and $\varsigma \in \{0,..N_h - 1\}$.

Taking the expectation of $y[n]$ yields

$$E\{y[n]y[n+m]\} = E_p \sum_{i,j} E\{\delta[n - iT_c - c_i - \theta]\delta[n + m - jT_c - c_j - \theta]\} \qquad \textbf{(3-10)}$$

assumed $y[n]$ is an ergodic stationary and its expectation depends only on the value of m, m is a time interval used to measure the expectation or mean value, i.e.,

$$E\{y[n]y[n+m]\} = E_p T_c \delta[m] \qquad \textbf{(3-11)}$$

Thus, the spectrogram of UWB signal becomes

$$E\{I^{(y)}[k]\} = E_p T_c N = \beta^{(y)}[k] \qquad \textbf{(3-12)}$$

and $$\lambda^{(y)}[k] = 0$$

3.2.2 White Gaussian Noise in the Spectrogram

The AWGN in $f[n]$ is defined by

$$x[n] = \sum_j n_j \delta[n - c_j - jN_h] \quad \textbf{(3- 13)}$$

and assuming that the pulse duration is shorter than the chip duration. The expectation of $E\{n_j\} = 0$ and $E\{n_i n_j\} = \sigma_x^2 \delta(j-n]$, where σ_x^2 denotes the noise variance. Taking the same approach as in section 3.2.1, the expectation of noise spectrogram is

$$E\{I^{(x)}[k]\} = \sigma_x^2 N / N_h = \beta^{(x)}[k] \quad \textbf{(3- 14)}$$

and

$$\lambda^{(x)}[k] = 0$$

3.2.3 Narrowband in the Spectrogram

The single tone is expressed as

$$\tilde{s}[n] = \sqrt{2E_s}\cos(\frac{2\pi k_n}{N} n + \varphi) \quad \textbf{(3- 15)}$$

Assume the NB signal having its phase (φ) constant over the spectrogram duration NT_c then its expectation can be expressed as

$$E\{X^{(s)}[k]\} = \sum_{m=0}^{N-1} \tilde{s}[m] E\{c[m]\} \cos\left(\frac{2\pi km}{N}\right) \quad \textbf{(3-16)}$$

It is easy to verify that $E\{c[m]\} = 1/N_h$ which leads to the expectation of expression (3-16) become:

$$E\{X^{(s)}[k]\} = \frac{\sqrt{E_s} N}{N_h} \left(\delta[k - k_n + N] - \delta[k_n + k]\right) \cos(\varphi) \quad \textbf{(3- 17)}$$

likewise for the $Y[k]$ component, its expectation calculation is;

$$E\left\{Y^{(s)}[k]\right\} = \frac{\sqrt{E_s}N}{N_h}\left(\delta[k-k_n+N]-\delta[k_n-k]\right)\sin(\varphi) \quad \textbf{(3- 18)}$$

It is obvious that the TH code and NB itself are independent to each other and the derivation of the expectation $E\left\{I^{(s)}[k]\right\}$ is as the following:

$$E\{s[n+m]s[n]\} = \tilde{s}[n+m]\tilde{s}[n]E\{c[n+k]c[n]\} \quad \textbf{(3-19)}$$

Since $E\left\{I^{(s)}[k]\right\}$ is a discrete Fourier transform (DFT) of $E\{s[n+m]s[n]\}$ and a multiplication of two signals in the discrete time domain is equivalent to the circular convolution of both signals in the discrete frequency domain, consequently,

$$E\left\{I^{(s)}[k]\right\} = \frac{1}{N^2} I^{(\tilde{s})}[k] \otimes E\left\{I^{(c)}[k]\right\} \quad \textbf{(3-20)}$$

where $I^{(\tilde{s})}[k]$ and $I^{(c)}[k]$ denote the spectrogram of $\tilde{s}[n]$ and $c[n]$. Thus,

$$I^{(\tilde{s})}[k] = E_s N^2 \delta[N-k_n] + E_s N^2 \delta[k_n] \quad \textbf{(3-21)}$$

The frequency k is circular which leads to the relation of,

$$\delta[-k] = \delta[N-k] \quad \textbf{(3-22)}$$

This is also hold true for

$$E\left\{I^{(c)}[-k]\right\} = E\left\{I^{(c)}[N-k]\right\} \quad \textbf{(3-23)}$$

Thus, the autocorrelation of TH code becomes,

$$E\{c[n+k]c[n]\} = \frac{1}{N_h}\delta[k] - \frac{N}{N_h^3}(1-tri(\frac{1}{N_h})) \quad \textbf{(3-24)}$$

where

$$\begin{cases} tri(x) = 1-|x| & x \in (-1,1) \\ tri(x) = 0 & \text{otherwise} \end{cases}$$

The expectation of the spectrogram is now equal to

$$E\left\{I^{(c)}[k]\right\}=\frac{N}{N_h}+\frac{N^2}{N_h^2}\delta[k]+\frac{N}{N_h^3}\left(\frac{\sin(N_h\frac{\pi k}{N})}{\sin(\frac{\pi k}{N})}\right) \quad \textbf{(3-25)}$$

Furthermore, the expectation including the effect of a periodic non-uniform sampling becomes

$$E\left\{I^{(s)}[k]\right\}=\frac{E_s}{N^2}\left[E\left\{I^{(c)}[k-k_n]\right\}+E\left\{I^{(c)}[k_n-k]\right\}\right] \quad \textbf{(3-26)}$$

Equation (3-26) shows that the time hopping (TH) code spread energy of the NB signal over the spectrogram, as the result, the code decreases the detection probability. However, the delta peak (i.e., $\frac{N^2}{N_h^2}\delta[k]$) calculated in Equation (3-25) ensures the central frequency of the narrowband signal can still be identified. The variance of NB signal can be found as

$$\beta^{(s)}[k]=\frac{E_s}{2}\left(E\left\{I^{(c)}[k-k_n]\right\}+E\left\{I^{(c)}[k_n-k]\right\}\right)-\lambda^{(s)}[k] \quad \textbf{(3-27)}$$

where $\lambda^{(s)}[k]=\frac{E_s N^2}{2N_h^2}\left(\delta[k-k_n+N]-\delta[k_n-k]\right)$

This clearly indicates that the distortion factors are N and N_h. The NB detector to be given in the following.

3.3 The Detector

A successful detection takes place at frequency k whenever the spectrogram $I_{n_o}[k]$ exceeds a threshold η. The threshold η is the average power of the receiving signal, while $I_{n_o}[k]$ is the peak power at frequency k at time n_o and k is the central frequency of the NB. The probability of this event in closed form is

$$P[k] = P\{I_{n_o}[k] > \eta\} = \int_{\eta}^{\infty} p(x; \lambda[k]; \beta[k]; \nu[k])dx \qquad \textbf{(3-28)}$$

The correct detection only occurs at $k = k_n$, such that the detection probability $P_d = P[k \mid k = k_n]$, otherwise a fail alarm is reported, where k_n is the short form of frequency k at time n. Note that the solution for expression (3-28) can not be found in a closed form. An alternative solution is to apply a Monte-Carlo simulation.

3.4 Monte-Carlo Simulation Structure and Results

Monte-Carlo simulation is a good method to find a solution when the solution can not be evaluated from a closed form expression.

3.4.1 Monte-Carlo Simulation Structure

The Monte-Carlo method is a game of chance in which a random experiment is replicated a number of times. Monte-Carlo simulation inherits a rich history spanning several centuries. The first application of Monte-Carlo of which we are aware was suggested by Laplace in 1777, who used Monte-Carlo method to estimate the value of π using a technique known as Buffon's needle [43]. A later application was developed in 1946 by Polish mathematician Stainishaw Ulam while pondering the probabilities of winning the game of Solitaire.

All Monte-Carlo simulations, including those simulated by Laplace and Ulam, are implementations of a stochastic (random) experiment designed to estimate the occurring probability of a particular event. This is facilitated through the use of two counters in the simulation program. The first counter, known as the replication counter, measures the number of replications of the random experiment and is incremented by one every time the random experiment is repeated. The second counter known as the event counter is incremented by one every time the event of interest is observed. The relative frequency, or probability estimate, of the event of interest occurring is $\hat{p} = R/N$, where R and N represent the values in the event and replication counters at the end of the simulation run.

Figure 3-1 shows a NB detector applying the Monte-Carlo simulation method to find the probability of detecting NB signal. The incoming signal $f(t)$ consists of UWB, NB and AWGN signals; these are 3 major components of the communication system under studying. The signal is then passed to the periodogram (or spectrogram) block to estimate its power. The average (or a threshold value) and maximum power extracting from the periodogram is to be used later for detection. The detector compares average power with the maximum power at the narrowband central frequency. A switch enable is on when the maximum power is greater than the threshold and off otherwise. The event and replication counters serve as the probability evaluation. The event counter is the correct counter, this counter only increments by one when the maximum power at the NB central frequency greater than the average power. The following simulation results serve as a sanity check and validation for the expression (3-28).

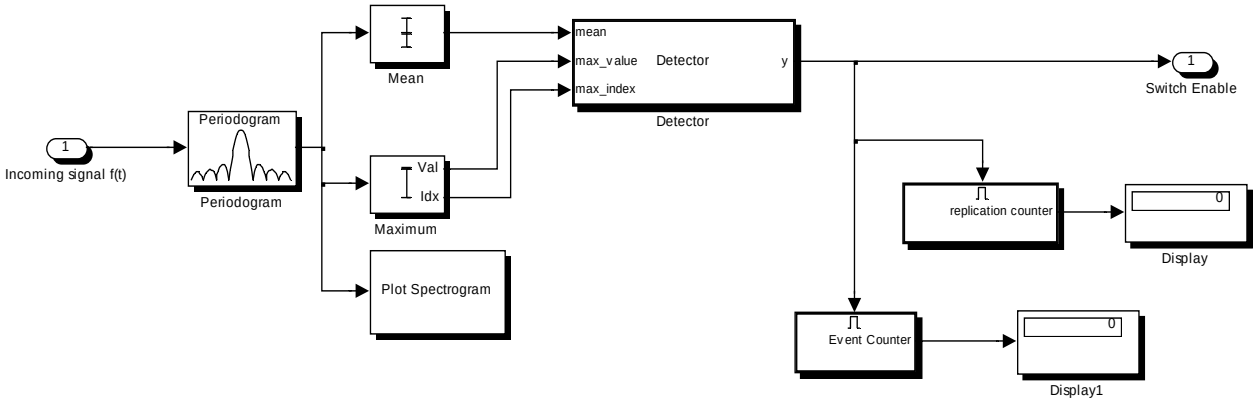

Figure 3-1. Narrowband Detector block.

3.4.2 Simulation Results

There are 3 assumptions for the system in the simulation. (a) there is no inter-symbol-interference (ISI), (b) channel estimation and system synchronization are perfect and (c) there is only one OFDM signal active at 5.1925-5.2075 GHz.

This UWB system was constructed using Time Hopping-Pulse Position Modulation (TH-PPM) technique which inherents the following characteristics. The system transmitting power is 0.04 mW acquiring a speed at 50 Mbps with a chip time T_c = 1 ns and a PPM shift factor of 0.5 ns. The simulate pulse shape is a 2^{nd} order derivative Gaussian pulse having a bandwidth (BW) of 4 GHz. Communication channel model is a IEEE standard channel having four different types: CM1, CM2, CM3 and CM4.

Up to this time, there is no regulation specifying exact transmitting power of the OFDM signal, except there is a maximum power mandate of 50 mW [44]. This power level is about triple digits higher than the regulated UWB power (i.e., 0.039mW). For the purpose of simulation, the NB power is set from 5 times smaller to 10 times higher than the UWB power. The results show that if the NB power less than UWB power,

there is a almost no significant change in term of UWB system performance. However, there is a slight effect on the performance when the two power levels are equal and a noticeable effect when the NB power is greater than the UWB power.

The following five figures show the spectrograms for various NB to UWB signal power ratios using CM2, SNR=14. The frequency displays is in normalized scale at 6.3 GHz, and the amplitude is measured in Watts. Figure 3-2 shows a fail detection when the NB signal is about 5 times smaller than the UWB signal. The power at which NB taking place is smaller than the overall average power therefore the detection fails. This results remain unchanged as long as the NB power is less than the UWB power.

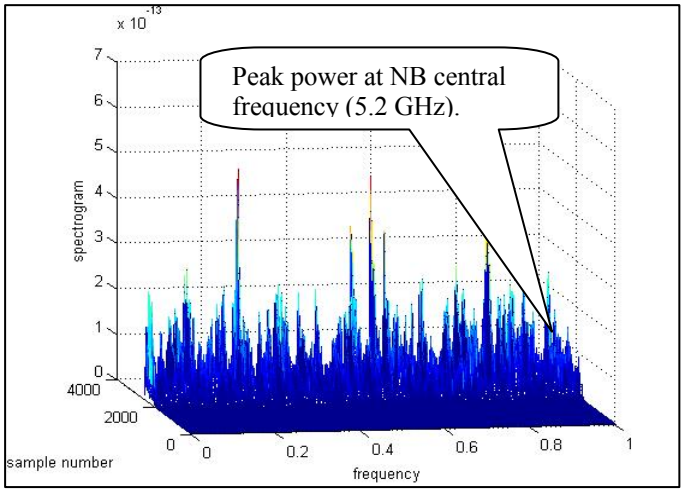

Figure 3-2. Spectrogram of data, NB power = 0.2x UWB power, fail detection.

When the power of NB and UWB are equal, detection results are about equal chance. Figure 3-3 shows two typical snap shots when NB and UWB are equal in power, it is about 50% chance to detect the NB signal. In these figures, k is the arrival time and f_o is the frequency at which the periodogram attains its maximum. It can be verified that the theoretical power for NB approximately equal to $8.935x10^{-9}\ mW$ with $N = 512$ and $N_h = 3$.

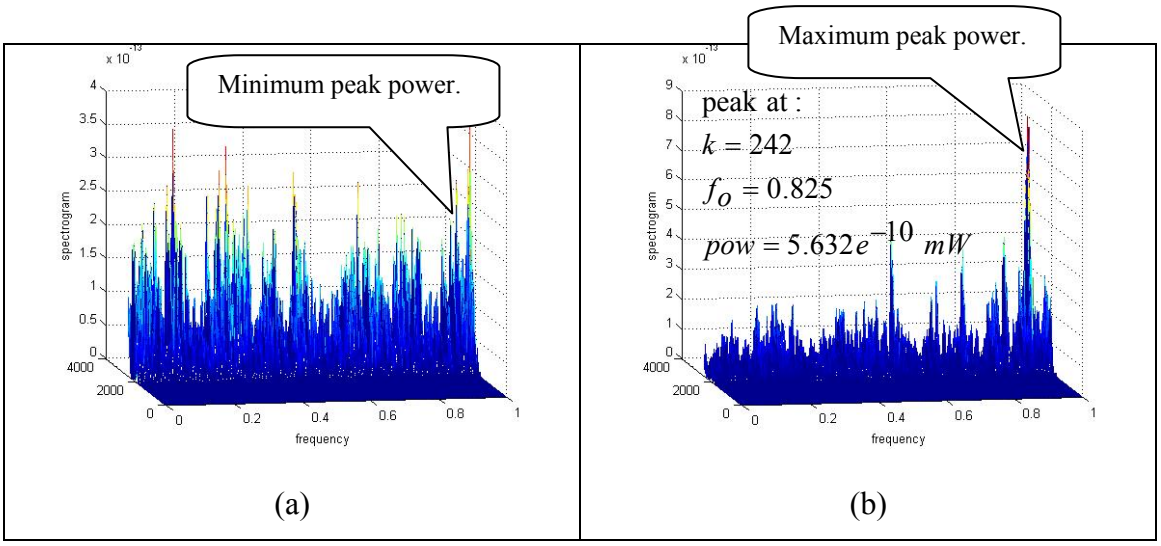

Figure 3-3. Spectrogram of data, NB power=UWB power, (a) fails detection, (b) successful detection.

Simulation results and theory results are close to within 6.5% marginal offset. This proves that the assumption treating NB signal as a tone is valid.

The next two figures show the results in the case of NB power having 5 times and 10 times larger than the UWB power. In Figure 3-4, the maximum power peak at NB frequency is significantly different than the overall average power, the detection outcome is always successful.

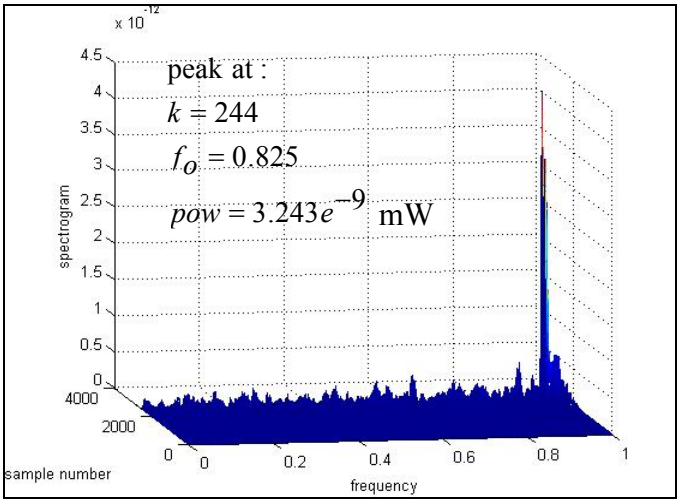

Figure 3-4. Spectrogram of data, NB power =5x UWB power, successful detection.

Similar to Figure 3-4, the maximum peak power at the NB central frequency is far leading the overall receiving signal power, the NB is always detected in Figure 3-5.

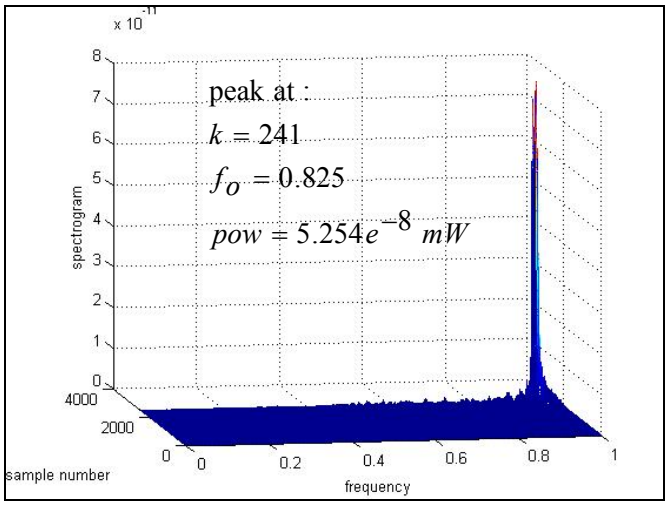

Figure 3-5. Spectrogram of data, NB power = 10x UWB power, successful detection.

Table 3-1 summarizes detection probability for various NB to UWB power ratios. The convergence with its confident interval is ranged from 60,000 to 150,000 bits. The determination of the confident interval is determined using *ttest* command from Matlab with a mean equal to 75,000 bits.

Table 3-1 Different Power Ratios and Detection Probabilities.

Power ratio OFDM /UWB	Detection Failure (%)	Correct Detection (%)
1/5	99.8	0.2
1	43	57
5	0.9	99.1
>10	0	100

3.5 Summary

Using spectrogram technique, the task to identify the NB signal standing out in the UWB signal becomes easier. This is the best approach to detect NB signal in UWB. Simulation results show that when the power of NB equal to UWB signal, the probability of detection has an equal chance. A significant improvement in successful detection when the NB power is 5 times larger than the UWB power. Simulation results show that NB signal can be treated as a tone in UWB system.

Chapter 4 Narrowband Interference Cancellation Circuit and On-Chip Implement Methodology

The aim of this chapter is to discuss and analyze the NB cancellation circuit in time domain. First, the NB cancellation circuit topology will be presented and the analysis will be performed on the circuit thereafter. Subsequently, part of the NB cancellation circuit, the NB central frequency estimation will be presented. A brief introduction of FPGA and the method to implement an adaptive filter are to be given at the end of the chapter.

4.1 Introduction

Many digital signal processing techniques have been investigated to suppress or mitigate narrowband interference (NBI) in the wideband system [21, 22, 23, 24, 25]. These techniques were introduced mainly for spread spectrum systems (i.e., wide bandwidth) and in principle, these can be applicable to UWB. In general, NB suppression is achieved using either linear or non-linear prediction digital filters. However current digital technology does not allow for a cost effective realization of a complete digital UWB system. Therefore it is necessary to investigate techniques which are either pure analog or a combination of analog and digital. This chapter describes the time-domain techniques which perform narrowband interference rejection in the radio frequency (RF) front end. This does not necessarily mean the circuit is entirely analog. In fact, digital techniques can be used with the sampling rates commensurating with the

narrowband interferer bandwidth rather than the UWB signal bandwidth. The proposed NBI cancellation circuit is given in the following section.

4.2 Time Domain Narrowband Cancellation Circuit

Figure 4-1 illustrates a circuit block diagram for a combination analog and digital interference eliminator that performs time domain mitigation in the receiver RF front end. The circuit was previously presented in [25], [45] and similar to a circuit introduced in [26]. These circuits attempt to estimate a narrowband interferer signal in the digital form and then cancel the interference in the analog form. The advantage of this approach comes from the fact that the sampling and digital processing occur at a rate commensurate with the narrowband signal bandwidth rather than the UWB bandwidth, which is relatively higher.

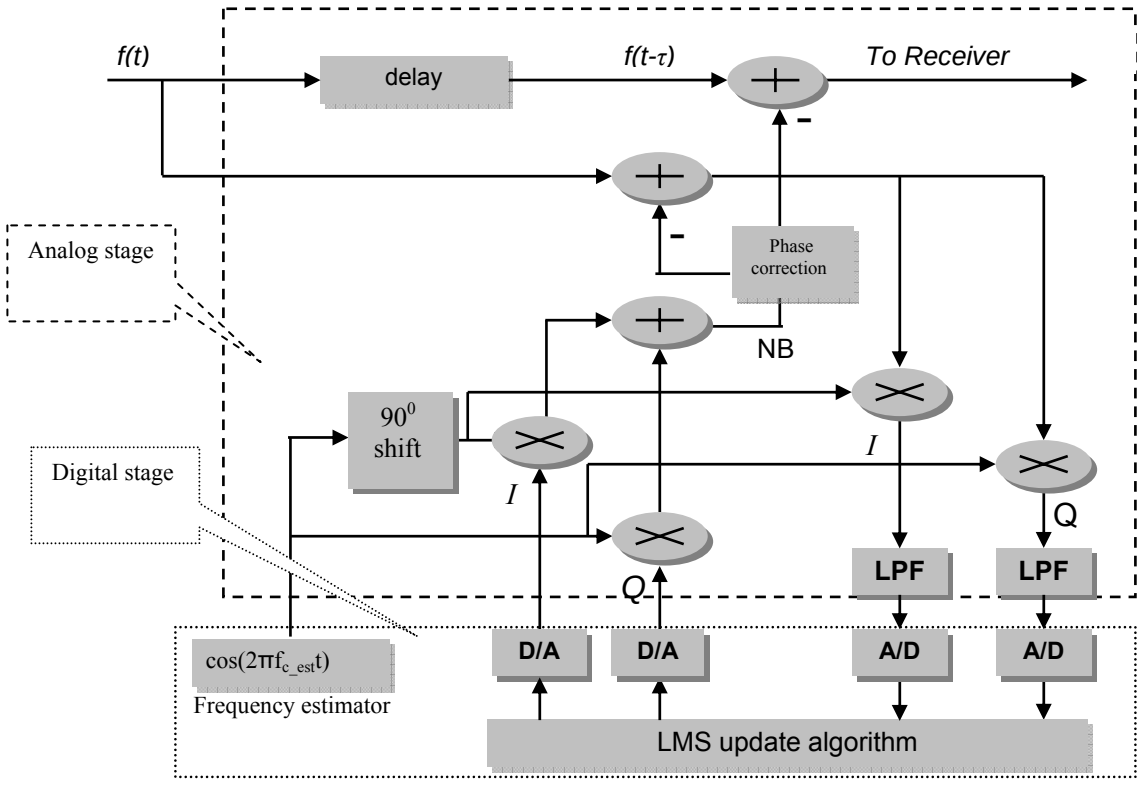

Figure 4-1. Time Domain Front End NB Cancellation Circuit.

There are two stages in the cancellation unit: digital and analog stage. A mixer is required in the analog stage. The mixer down-converts the incoming signal into an inphase (I) and quadrature (Q) representations allowing the digital signal processing to be performed. The NB signal estimating from the digital stage must be up-converted in order to cancel the interference in the analog stage. The NB central frequency f_{c_est} is obtained from the frequency estimator (see the next section of this chapter). An analysis of the ability to perform this frequency estimation is given in Section 4-3, in which the method of moment and maximum likelihood estimator are examined.

Considering the operation of the digital portion in Figure 4-1. After the down-conversion, the signal is lowpass filtered, sampled, and passed to a digital least mean squares (LMS) update algorithm. In this digital stage, the circuit performance is directly related to the strength of the narrowband interferer compared to the noise it observes (i.e., the interference to noise ratio (INR)). INR of the mitigation circuit is determined by the thermal noise in the system and the noise contributed from the UWB signal. It was shown in [25] and [45] that after lowpass filtering, the noise contributed from UWB signal can be modeled as additive white Gaussian noise (AWGN). As the results, the combination of the UWB signal and thermal noise can be modeled as Gaussian noise.

After the signal is down-converted and sampled, the narrowband interference is estimated using digital filtering techniques. The LMS algorithm is used along with a multiple tap LMS filter to estimate the interference by successively updating the weights of the I and Q channels. A brief detailed introduction to the LMS theory to be given in the following section.

4.2.1 The Least Mean Squares Theory

The origin of LMS is attributed to Windrow and Hoff in the late 1960 [46], [47]. The LMS is based on the estimation of the gradient toward an optimal solution using statistical properties of the input signal. Figure 4-2 shows a typical structure of the LMS adaptive filter.

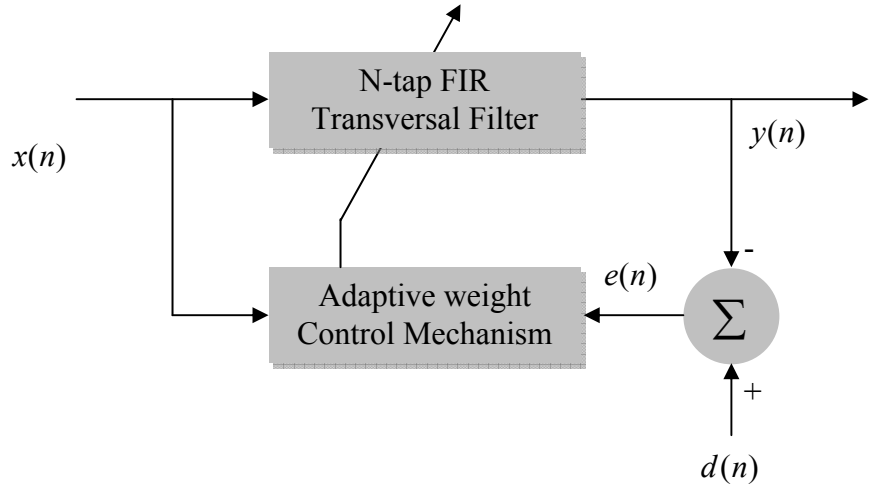

Figure 4-2. LMS Adaptive Filter Block Diagram.

The LMS filter is responsible for estimating the transmitting signal denoted as $y(n)$ from the noisy receiving signal $x(n)$ at the receiver by training the filter coefficients. The training coefficients are to be used to remove the noise as much as possible from the receiving signal to achieve the maximum estimation level. Detail of the estimation will be presented in the following.

A significant feature of the LMS algorithm is its simplicity. The N-tap filter weights are updated with each new sample as required to meet the desired output. The computation required for the updating is graphically illustrated in Figure 4-3 and numerically in Equation (4-3).

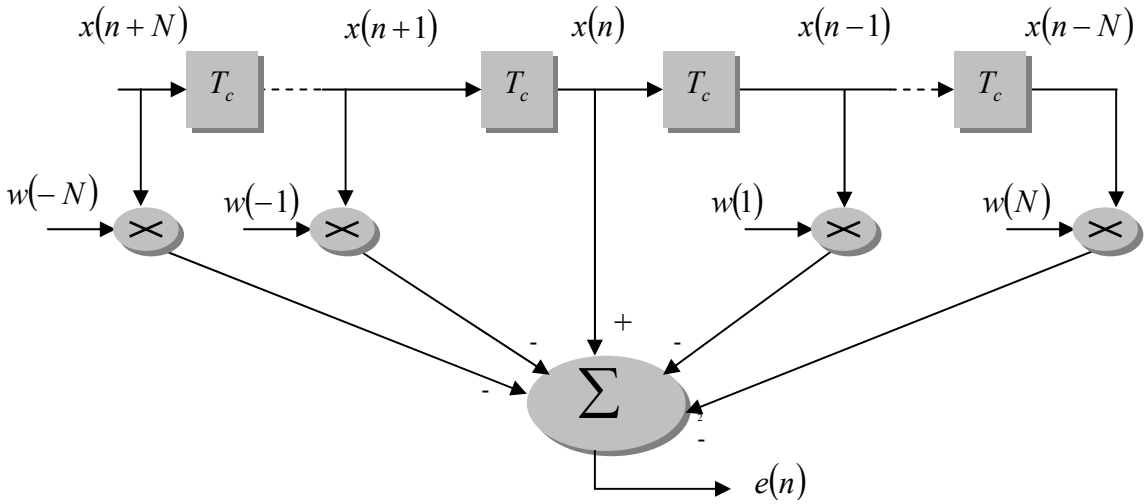

Figure 4-3. Multi- tap Adaptive Filter.

The LMS algorithm computation is given by the following Equations [48]:

1. Compute the estimate of the interferer, $y(n) = w(n)x^T(n)$ **(4-1)**
2. Compute the error signal, $e(n) = d(n) - y(n)$ **(4-2)**
3. Calculate the new filter weights, $w(n+1) = w(n) + \mu T_c x(n) e(n)$ **(4-3)**

In the above steps, $x(n)$ is the current received signal value, $w(n)$ is the vector of filter coefficients $[w(-N).....w(-1), w(1).....w(N)]$ and x is the vector of past and future received signal values $[x(n+N).....x(n+1), x(n), x(n-1).....x(n-N)]$ for $N \neq 0$ where x^T is the transposed version of x. The value μ denotes a learning rate and T_c is the sample time. The output $y(n)$ represents the residual narrowband interference and noise. The value of $d(n)$ represents the estimate of the interferer. The weights are updated every sample of the received signal and the output of the LMS multi-tap update algorithm is the estimate of the interferer, $d(n)$. The estimated NB value is then up converted and subtracted from the delay and phase offset version of the received signal. The rate of

convergence of the LMS algorithm is directly related to the filter length N and the weight update parameter μ. The choice of μ and N are to be discussed in Section 4-5.

The method to implement the digital LMS adaptive filter in FGPA will be addressed in sections 4.4 and 4.5. The following section presents the method to estimate the NB central frequency.

4.3 Frequency Estimation

Other fundamental component of the narrowband interference cancellation circuit is the ability to estimate the interferer frequency. The following discussion examines two frequency estimations taken from Kay [58]. The first technique uses a method of moments and the second technique uses the maximum likelihood estimator.

4.3.1 Method of Moments

In this method, the received discrete time signal is assumed to be

$$y[n] = A\cos(2\pi f_o n + \phi) + x[n] \qquad (n = 0,..., N-1) \qquad \textbf{(4-4)}$$

where $x[n]$ is zero mean white noise with variance σ^2, A is an amplitude, f_o is the frequency to be estimated. The phase ϕ is considered to be uniformly distributed between $(0,2\pi)$ and is independent of $x[n]$. Making this assumption allows $s[n] = A\cos([2\pi f_o n + \phi])$ to be treated as a realization of a wide sense stationary (WSS) random process. WSS implies the mean of the function is equal to zero and its autocorrelation depends only on the time when the function being observed. To verify this assumption, the mean and autocorrelation of $s[n]$ are examined.

The expectation and autocorrelation of $s[n]$ are computed as follow:

$$\begin{aligned} E\{s[n]\} &= E\{A\cos(2\pi f_o n + \phi)\} \\ &= \int_0^{2\pi} \frac{1}{2\pi} A\cos(2\pi f_o n + \phi) d\phi \\ &= 0 \end{aligned} \tag{4-5}$$

and the autocorrelation is given by:

$$\begin{aligned} r_{ss}[k] &= E\{s[k]s[n+k]\} \\ &= \mathrm{E}\left\{\mathrm{A}^2\cos(2\pi f_o n + \phi)\cos(2\pi f_o (n+k) + \phi\right\} \\ &= \mathrm{A}^2 E\left\{\frac{1}{2}\cos(4\pi f_o n + 2\pi f_o k + 2\phi_1) + \frac{1}{2}\cos(2\pi f_o k)\right\} \\ &= \frac{1}{2}A^2\cos(2\pi f_o k) \end{aligned} \tag{4-6}$$

The autocorrelation of the white noise, $x[n]$ is given by $r_{xx}[k] = \sigma^2\delta[k]$ and using the result of Equation (4-6), the autocorrelation of the received signal $r_{ss}[k]$ becomes:

$$r_{ss}[k] = \frac{1}{2}A^2\cos(2\pi f_o k) + \sigma^2\delta[k] \tag{4-7}$$

In order to estimate the frequency using this method $r_{SS}[k]$ is used:

$$r_{ss}[1] = \frac{1}{2}A^2\cos(2\pi f_o) \tag{4-8}$$

This allows the estimation to be performed without knowledge of the noise variance. An estimate of the frequency is then given by:

$$\hat{f}_o = \frac{1}{2\pi}\cos^{-1}\left(\frac{\hat{r}_{ss}[1]}{A^2/2}\right) \tag{4-9}$$

where the autocorrelation $r_{SS}[1]$ is estimated as

$$\hat{r}_{ss}[1] = \frac{1}{N-1}\sum_{n=0}^{N-2} y[n]y[n+1] \tag{4-10}$$

In Equation (4-9), the term representing the average power of the sinusoid, $A^2/2$, must be also estimated.

The amplitude estimation is given by:

$$\frac{A^2}{2} = \frac{1}{N}\sum_{n=0}^{N-1} y^2[n] \tag{4-11}$$

and the frequency f_o is finally estimated as:

$$\hat{f}_o = \frac{1}{2\pi}\cos^{-1}\left[\frac{\frac{1}{N-1}\sum_{n=0}^{N-2} y[n]y[n+1]}{\frac{1}{N}\sum_{n=0}^{N-1} y^2[n]}\right] \tag{4-12}$$

Note that the estimate of f_o is a normalized frequency of the signal such that the estimate found for f_o is between 0 and 0.5. It is shown in [58] that for a high SNR, this method has an expected value which is equal to f_o. The author also provides an expression for the variance of the estimation that highlights limitations of this method. The variance of this estimation decreases rapidly for increasing block size at f_o=0.25 while the variance slowly decreases at f_o close to 0 or 0.5. This results from the use of the $\cos^{-1}$ function of Figure (4-4) in the estimation. Observe that the slight variations in the value of $y[n]$ near 0 and large variation near the points -1 and 1, this is due to the steepness of the curve near those two values. In the next section, the method of maximum likelihood will be presented.

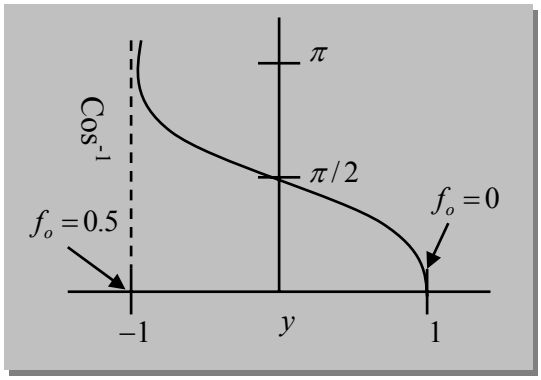

Figure 4-4. Invert cosine computation.

4.3.2 Method of Maximum Likelihood

The second frequency estimation technique is the maximum likelihood estimator (MLE) derived from the probability density function (PDF) of the received signal. Again the received signal is taken as

$$y[n] = A\cos(2\pi f_o n + \phi) + x[n] \qquad (n = 0,..., N-1) \tag{4-13}$$

which results in the PDF of $x[n]$ is

$$\begin{aligned} P_w &= \frac{1}{(2\pi\sigma^2)^{\frac{N}{2}}} \exp\left[-\frac{1}{2\sigma^2} \sum_{n=0}^{N-1} (x[n])^2 \right] \\ &= \frac{1}{(2\pi\sigma^2)^{\frac{N}{2}}} \exp\left[-\frac{1}{2\sigma^2} \sum_{n=0}^{N-1} (y[n] - A\cos(2\pi f_o n + \phi))^2 \right] \end{aligned} \tag{4-14}$$

where $A > 0$ and $0 < f_o < 0.5$. The maximum likelihood estimate of f_o is then found by maximizing the argument of the exponential in the PDF with respect to f_o. According to [58], the following expression needs to be minimized:

$$\begin{aligned} J(A, f_o, \phi) &= \sum_{n=0}^{N-1} (y[n] - A\cos(2\pi f_o n + \phi))^2 \\ &= \sum_{n=0}^{N-1} (y[n] - A\cos\phi\cos(2\pi f_o n) + A\sin\phi\sin(2\pi f_o n))^2 \end{aligned} \tag{4-15}$$

by letting

$$\begin{aligned} c &= [1 \;\; \cos 2\pi f_o ..... \cos 2\pi f_o (N-1)]^T \\ s &= [1 \;\; \sin 2\pi f_o ..... \sin 2\pi f_o (N-1)]^T \end{aligned} \tag{4-16}$$

and transforming J into a quadratic using the following transformation

$$\begin{aligned} \alpha_1 &= A\cos\phi \\ \alpha_2 &= A\sin\phi \end{aligned} \tag{4-17}$$

leads to the following relationship

$$\begin{aligned} J'(\hat{\alpha}_1, \hat{\alpha}_2, f_o) &= (y - \alpha_1 c - \alpha_2 s)^T (y - \alpha_1 c - \alpha_2 s) \\ &= (y - H\alpha)^T (y - H\alpha) \end{aligned} \quad \textbf{(4-18)}$$

where $\alpha = [\alpha_1 \alpha_2]^T$ and $H = [cs]^T$. It was shown in [58] that the solution of Equation (4-18) is given by:

$$\hat{\alpha} = \left(H^T H\right)^{-1} H^T y \quad \textbf{(4-19)}$$

which results in

$$\begin{aligned} J'(\hat{\alpha}_1, \hat{\alpha}_2, f_o) &= (y - H\hat{\alpha})^T (y - H\hat{\alpha}) \\ &= \left(\mathrm{y} - \mathrm{H}(\mathrm{H}^{\mathrm{T}} H)^{-1} H^T y\right)^T \left(\mathrm{y} - \mathrm{H}(\mathrm{H}^{\mathrm{T}} H)^{-1} H^T y\right) \\ &= \mathrm{y}^{\mathrm{T}} (I - H(H^T H)^{-1} H^T) y \end{aligned} \quad \textbf{(4-20)}$$

and $I - H(H^T H)^{-1} H^T$ is an idempotent matrix. In order to estimate the frequency f_o, Equation (4-20) needs to be minimized or accordingly the following must be maximized:

$$\mathrm{y}^{\mathrm{T}} (I - H(H^T H)^{-1} H^T) y \quad \textbf{(4-21)}$$

Substitute H definition into Equation (4-21) yields

$$\begin{bmatrix} c^T y \\ s^T y \end{bmatrix}^T \begin{bmatrix} c^T c & \mathrm{c}^{\mathrm{T}} s \\ s^T c & \mathrm{s}^{\mathrm{T}} s \end{bmatrix} \begin{bmatrix} c^T y \\ s^T y \end{bmatrix} \quad \textbf{(4-22)}$$

Finding the maximum value of Equation (4-21) according to f_o determines the MLE estimate for f_o. The frequency estimation results and discussions are available at section 5.5. The following sections describe the implementation of the digital LMS adaptive filter in FPGA devices.

4.4 Hardware Implementation of The LMS Adaptive Filter

Digital signal processing (DSP) unit is fast moving up to the next level in the digital world, one example is it now can be integrated on a single field programmable gate array (FPGA) device. The objective in this section is to find an adaptive algorithm that is suitable for high-speed implementation on Altera® FPGA platform, in particular, the Stratix family devices. This section starts with the introduction to the FPGA technology and followed by the method to design and integrate the pipeline LMS in FPGA devices.

4.4.1 FPGA Technology

In the late 1970s, FPGA idea was introduced and the first FPGA XC2000 series was invented by Xilinx® in 1985. The advantage of FPGAs is that they combine the performance that can be achieved by Application-Specific Integrated Circuit (ASIC) with the flexibility of programmable microprocessors. With this merit FPGAs demolishes the balance of gate array market and have been taking a significant portion of the standard cell market.

Conceptually, a programmable FPGA consists of three key elements as illustrated in Figure 4-5:

- The *Programmable logic cells* provide functional elements to construct user logics.
- The *Programmable Input/Output* (*I/O*) *blocks* provide interface between the package pins and the logic cells.
- The *Programmable interconnects* provide routing paths to connect the inputs and outputs of the logic cells and between the cells.

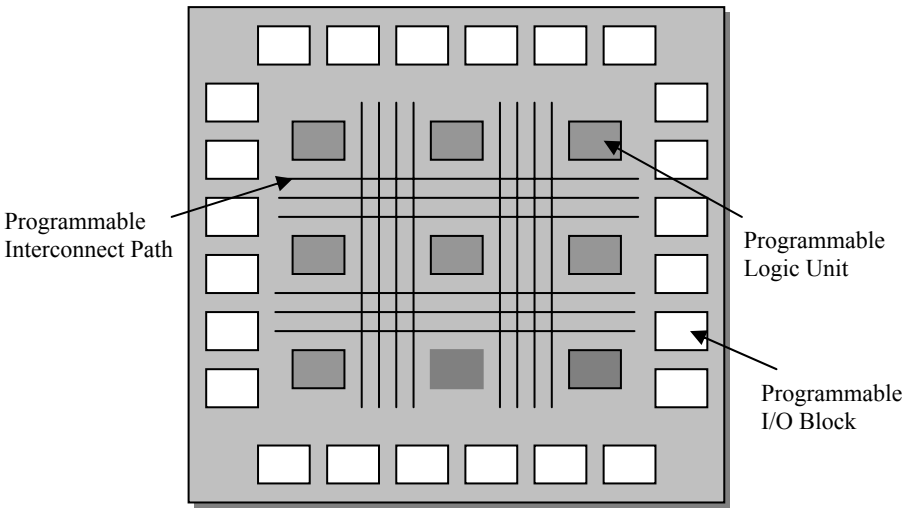

Figure 4-5. Conceptual structure (symmetrical array) of FPGAs.

In the past decade, FPGAs such as the Altera Stratix II family have grown in capacity up to 20 millions gates in a single device. FPGA has also improved in speed and increased in functionality. It now contains high-speed embedded arithmetic units, multipliers and an abundance of registers with clock speed up to 450 MHz [51]. It is not only capable of implementing high-speed DSP applications, but also can deliver system-on-chip (SoC) solutions. These advantages have inspired many DSP designers to shift their designs from the custom ASIC implementation to the more flexible FPGA platforms, thereby reducing design cost and time-to-market and overcoming the unforeseen changes or iterations needed during the design period.

The requirement for DSP algorithm sampling rate ranges from 8 kHz in speech applications to more than 7.5 GHz in Ultra-Wideband signal processing. The implementation of DSP algorithms on microprocessors (μP) or DSP processors is often proved unsatisfactory because they are unable to meet the high computational and sampling rate requirements for most of today real-time applications. As a result, majority of the high-speed applications are implemented in ASIC or FPGA devices

where parallelism and pipelining techniques can be used to improve speed and increase computation tasks of the design. Table 4.1 shows the performance comparison between a DSP processor and an FPGA device reported by Berkeley Design Technology Inc. [50].

Table 4-4-1. DSP vs. FPGA Performance.

Comparison Category	Altera Performance Advantage
Altera FPGAs vs. DSP processors	10x DSP processing power per dollar
High-performance FPGAs comparison: Altera's Stratix II FPGAs vs. Xilinx's Virtex-4 FPGAs	Up to 1.8x and on-average 1.2x higher performance
Low-cost FPGAs: Altera's Cyclone II FPGAs vs. Xilinx's Spartan-3 FPGAs	Up to 2x and on-average 1.5x higher performance

FPGA technology is still 10 times slower than their ASIC counterparts. The reason is that the FPGA designs are limited by the physical reality imposed by the device layout. In the context of DSP implementations, the speed of a DSP circuit is governed by the number of Multiply and Accumulate (MAA) operations per second. For an ASIC implementation, it is typical to opt for the fastest adder and multiplier available, such as the Carry-Look-Ahead (CLA) based adder and Wallace tree multiplier. Most FPGA vendors have opted for the Carry-Ripple Adder (CRA) as it is highly common and can be easily implemented in the technology. However, the CRA is usually slower than the CLA adder when implemented in an ASIC. The second aspect causing the poor speed performance in FPGA technology is the interconnect which can contribute up to 60% to the total signal propagation delay in an FPGA device. In contrast, interconnect in an ASIC design is just a relatively small portion of the total signal propagation delay (although this is changing as technologies get smaller and smaller size). Even considering the inefficient FPGA implementation of fast arithmetic functions in a DSP system, the programmability of FPGAs allows circuits to be

optimized to specific system needs, whereas it is necessary to design an ASIC implementation to be generic in order to justify its high development costs.

The FPGA marketplace is volatile, it is one of the fastest growing segments of the semiconductor industry. Nowadays many companies involved change their technology rapidly and it is somewhat difficult to predict which products will be the most significant for high-speed implementations when the industry reaches a stable state. For this reason, this work concentrates on devices with dedicated fast carry logic and carry chain features, which can be used for high-speed arithmetic implementations. These features can be found in the Altera Stratix family series and Xilinx Virtex family FPGA devices. The underlying structure common to all Altera devices are the Logic Element (LE) embedded in routing resources. This LE is based on a 4-input Look-Up-Table (LUT). A LUT is a small one-bit wide memory array, where the address lines for the memory are the inputs of the logic block and the one bit output from the memory is the LUT output. Rose and Sangiovanni-Vincentelli [51] have demonstrated that the use of a LUT with 4 inputs provides the best implementation density for a range of functions. A detailed description of the Stratix device can be found in [49], the Stratix series dedicated carry hardware is available for the construction of fast adders.

Next section shows the design methodology used to implement the FPGA based adaptive filter from algorithmic specifications.

4.4.2 FPGA Design Flow

The FPGA is divided into two parts; the algorithmic and the architectural part. This design approach attempts to optimize both the algorithmic and architecture for high-speed implementation. At the beginning of the design flow, the adaptive filter LMS

was simulated against different operational environments to determine key parameters such as step size and filter length for the best performance. A great portion of this work was spent on improving the algorithmic performance at this stage. Information such as the word-length required for a stable filtering operation was obtained by using the *Fixed-Point Block Set DSP* tool and *Signal Compiler* both from Altera associated with *Simulink* in Matlab.

To design an algorithm that can be efficiently implemented on hardware, knowledge regarding particular technology and processor architecture layout is vital. The bit-true models from the parameterized cores provide information on the minimum number of pipelining registers required to fulfil the sampling rate requirement. The pipeline version of the LMS algorithm was re-simulated in *Simulink* using the same operational environments to examine the impact of pipelining on the LMS algorithm. The simulation results from *Simulink* were also used to validate the post-synthesis simulation results from the FPGA implementation.

Before the key filter parameters which are established from *Simulink* simulations, are used in VHDL description, an architectural version of the LMS based algorithm needs to be carefully chosen or designed to reduce system critical paths, hardware resources and system output latency. This high level design is based on the knowledge of component size, performance, and predictable speed and area of the optimized cores. The cores used in the design flow were developed in *Simulink digital signal processing (DSP) library* and allowed accurate estimation of speed and performance. This library is a hierarchical library of components expressed structurally in VHDL which are optimized for the Stratix family. The components are parameterized for word-length, among other objects offer high speed operation. These cores are pre-implemented and

verified in the system, subsystem and component level which are created from lower level macros. The *Simulink DSP library* provides a series of specialized arithmetic function circuits for DSP applications, including a pipelined multiplier. The benefit of using these optimized cores is that they offer outstanding performance and device utilization, often more than 10 times better than generic HDL descriptions.

The functionality of VHDL code is confirmed before performing synthesis to a circuit netlist. The synthesis process uses specific synthesis constraints (i.e., timimg, area, and component relative location in the chip) to implement and optimizes the VHDL register-transfer-level into primitive blocks. The Synplify[5] tool is used because of its ability to specify component attribute values using complicated function calls (sub-routine). The FPGA independent netlist generated from the synthesis is converted into the specific Stratix FPGA device during Place and Route using *Altera Signal Compiler* tools. If the timing and speed requirements are not met, it is necessary to re-design the architecture or algorithm. Re-simulation of a post-synthesis VHDL version of the actual FPGA design ensures the functionality is maintained throughout the design flow.

The configuration bit stream generated after the Place and Route process is then downloaded from the terminal via the Peripheral Component Interconnect (PCI) bus to the hardware such as the EP1S80 DSP chip which is mounted onto a Stratix DSP S80 Development board. This Stratix DSP S80 is a PCI-based FPGA board that is used to validate the design and system performance. This design flow and implementation procedure, depicted in Figure 4-6, is used to design, implement and validate in this project.

[5] Synplify tool is the tool used to convert model descriptive language into hardware synthesizable code, see Figure 4-6.

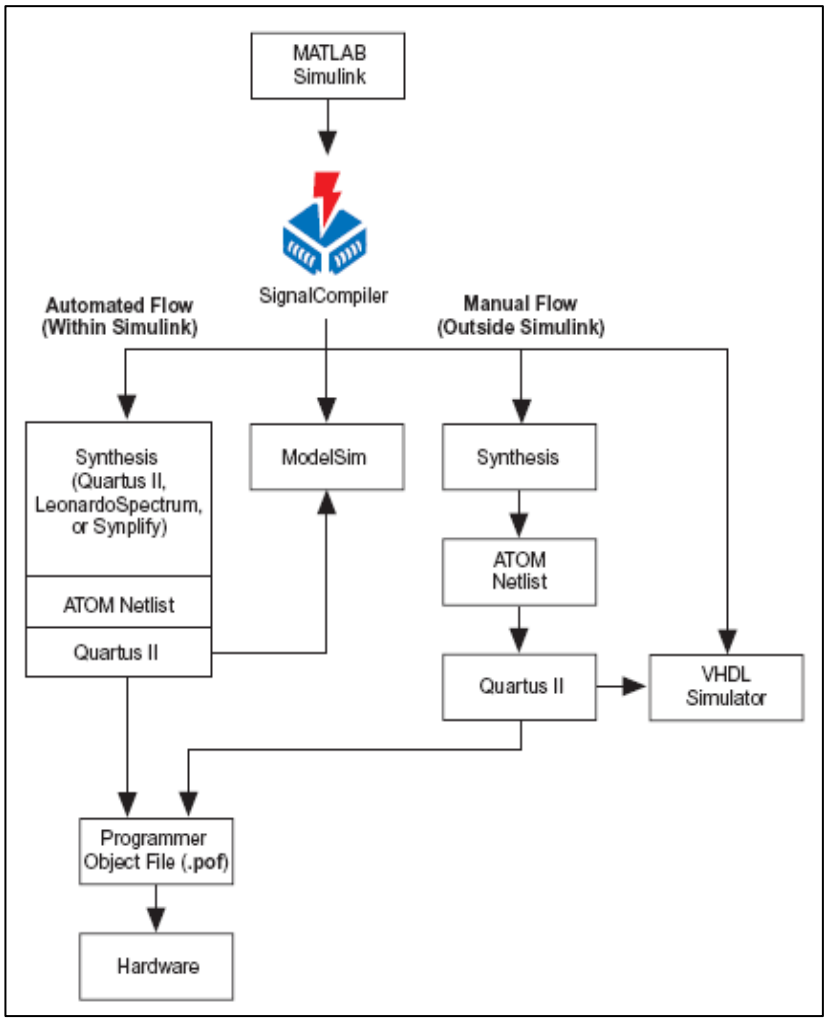

Figure 4-6. DSP Builder Design Flow.

4.4.3 Pipelined Adaptive LMS Filters Design

The pipelining technique is applied in the FPGA design to minimize latency or computational delay. Pipelining has the ability to exploit parallelism in which computations are carried out simultaneously. In adaptive LMS structure, the longest delay comes from the error feedback, it is necessary to find a solution minimizing this delay. The best approach in such case in the design is pipelining.

4.4.3.1 Pipelined Enabled LMS Based Algorithm

In the past fifteen years, rapid advances in digital technology are moving in a fast pace, the demand for complex algorithms to be implemented for real-time has grown. Meanwhile, researchers have realized that the throughput rate of the LMS algorithm is still sufficient for the high-speed DSP solution for today applications, in particular for Ultra-Wideband technology. Therefore, concurrency techniques have been introduced into the standard LMS algorithm to increase the sampling rate [52]. In return, this has inevitably changed the characteristics of the basic LMS algorithm.

The capability of pipelining is to be able to exploit parallelism. Pipelining depends heavily on the algorithm and implementation platforms such as ASIC, FPGA or DSP processors. Even if a parallel adaptive filter structure can be implemented in a parallel processor architecture, a long critical path in the feedback loop may limit the throughput rate. It is important to investigate pipelining as a technique to reduce critical paths and improve system throughput. However, pipelining technique of the LMS adaptive filter is a problem as it introduces latency to the error feedback loop. The adaptation algorithm, therefore, needs to be modified to enable the pipelined implementation. This results in the development of the three main approaches for pipelined LMS techniques based on look-ahead LMS [55], delayed LMS [53] and coefficient classification [54] algorithms. These algorithms act to ensure a stable convergence of the pipelining filters.

Similar to [52], the pipelined paths structure of the finite-impulse response LMS adaptive filter is shown in Figure 4-7. Detailed description is to be presented thereafter.

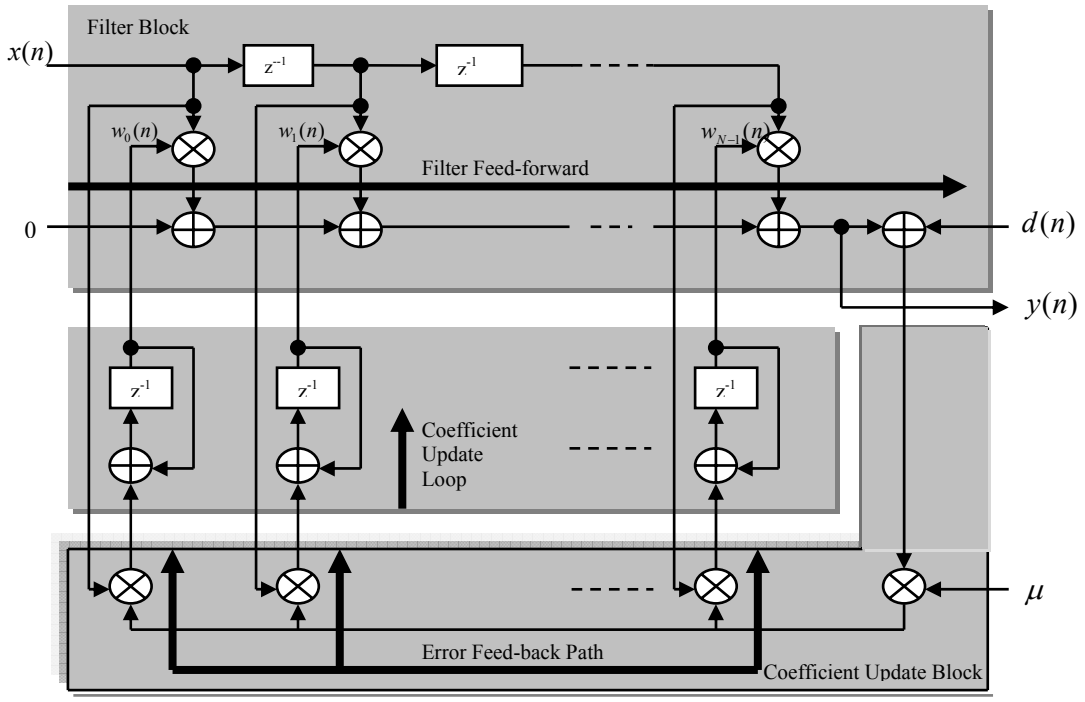

Figure 4-7. Pipeline path- FIR-LMS Adaptive Filter.

4.4.3.2 Filter Feed-forward Path (FFFP) and Error Feedback Path (EFP)

Pipelining of the filter block and the error signal feedback path is relatively simple but resulting in an increase in the latency of the circuit. The increase in latency forces the reference input $d(n)$ and input data $x(n)$ to be delayed by the same amount in the pipeline stage. This results in a mismatch in timing of the coefficients and the next set of the incoming signal for filter arithmetic processing. The late arrival of the coefficients due to the pipelining effect (i.e., latency), will deteriorate filtering performance mostly in the convergence behavior. The coefficient update loop to be presented in the following section.

4.4.3.3 Coefficient Update Loop (CUL)

Most of the problems come from the recursive loop when the coefficient adaptation loop is pipelined. This is due to the delay along the loop not only prolongs

convergence time but also dramatically increases latency and results in a poorer estimating performance. Decreasing pipelining by one in the loop will doubles filter convergence time.

There are three solutions to implement an adaptive filter with minimum amount of delay introduced from coefficient update loop: Delayed LMS, A Look-Ahead and Coefficient Classification adaptive filters. Each of these three methods is to be presented in the following sections.

4.4.3.4 Delayed LMS Adaptive Filter

The study of the Delayed LMS (DLMS) algorithm was carried out by Long [53] who investigated the effect of the coefficient adaptation delay in the LMS filter. The work shows the delay in the coefficient adaptation has only a slight influence on the steady-state behaviour of the LMS algorithm if the step size is within certain bounds. Usually a smaller step size compared to the standard LMS algorithm must be applied. Major drawbacks of the DLMS algorithm are the reduction in convergence speed for stationary signals and poorer tracking performance for non-stationary signals. The DLMS structure is shown in Figure 4-8 [58].

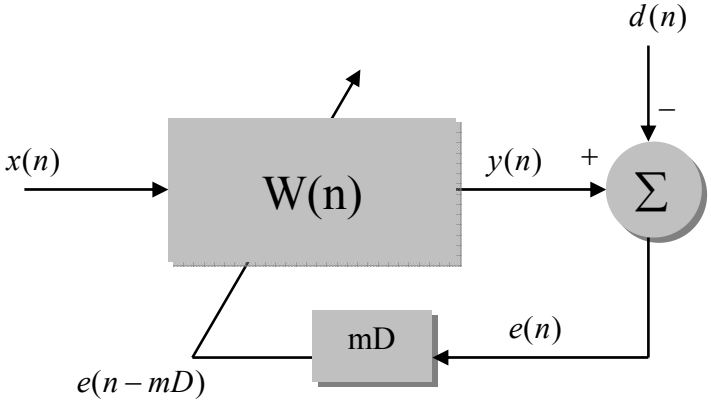

Figure 4-8. DLMS Structure.

where D and m in the figure are unit delay and a positive integer. The DLMS algorithm is calculated as the followings:

$$w(n+1) = w(n) + \mu e(n-mD)x(n-mD) \quad \textbf{(4-23)}$$

$$e(n-mD) = d(n-mD) - y(n-mD) \quad \textbf{(4-24)}$$

$$y(n-mD) = w(n-mD)x^T(n-mD) \quad \textbf{(4-25)}$$

and stability condition can be roughly estimated by the following expression:

$$0 < \mu < \frac{2}{(N-2m-2)P_{T_{in}}} \quad \textbf{(4-26)}$$

where N stands for the filter length and $P_{T_{in}}$ is the tap-in power[6]. Using the DLMS algorithm, pipelining registers can be inserted into the error feedback path in front of the adaptation loop, thus reducing the critical path in the long feedback loop in the recursive system.

4.4.3.5 Look-Ahead Transformation of LMS

Using the look-ahead technique, a finer grain pipelining can be achieved according to [55]. However, a direct implementation of the look-ahead transformation would result in increasing hardware complexity. The conventional look-ahead technique transforms a given serial algorithm into an equivalent pipelined version for the same input-output mapping. For adaptive filters, the exact input-output mapping is not required, therefore an approximate form of a look-ahead transformation is preferred for pipelining as it uses less hardware.

The Relaxed Look-Ahead LMS algorithm (RLA-LMS) is employed to develop fine-grain pipelined architecture for the LMS filtering [56], the structure of RLA-LMS is

[6] Extra power that unit delay *m* introduced.

shown in Figure 4-9. It results in a smaller hardware overhead which would not be possible with conventional look-ahead technique. Considering the first-order recursive loop, such as the LMS algorithm in Equation (4-3), the computation time of the first-order recursion is lower bounded by a single addition. In order to increase the throughput of the adder, m_2-step look-ahead is applied. This is equivalent to expressing $x(n)$ in terms of $x(n-m_2D)$, which gives:

$$w(n+1) = w(n-m_2D) + \mu \sum_{i=0}^{m_2-1} e(n-i)x(n-i) \qquad \textbf{(4-27)}$$

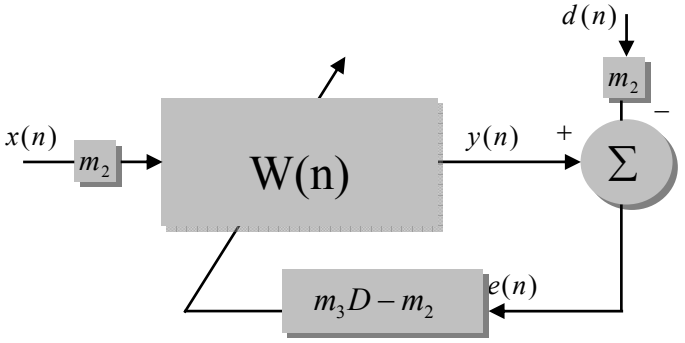

Figure 4-9. RLA-LMS Structure.

This transformation results in m_2 registers being introduced into the recursive loop. These registers can be used for fine-grained pipelining of the adder to any desired level. An increase in the level of pipelining (m_2) results in more hardware overhead. This can be reduced by applying the relaxed look-ahead technique, as shown in Equation (4-28), if the gradient estimation is relatively constant over a number of samples (m_3) in the error feedback path of the LMS filter. This is known as the delay relaxation [56].

$$w(n+1) = w(n-m_2D) + \mu \sum_{i=0}^{m_2-1} e(n-m_3D-i)x(n-m_3D-i) \qquad \textbf{(4-28)}$$

Note that when $m_2 = 0$ and $m_3 = m$, the equation is reduced to the DLMS algorithm. Therefore the DLMS algorithm is a special case in the stochastic form of look-ahead transformation.

The pipelining enabled LMS is essential for high-speed LMS based digital signal processing. Increasing the number of pipelining delays in the algorithm reduces the critical path but it increases the output latency and hardware complexity. The impact of an increased output latency may severely impair the performance. The increased hardware complexity can also possibly increase the critical path of the pipelined architecture and offset the effort of pipelining to improve system throughput.

4.4.3.6 Coefficient Classification of Adaptive Filter

The third modified adaptation algorithm is the coefficient classification conducted by Okello [54]. The technique is based on the pipeline concept of tree structure with up-sampling and down-sampling the signal before and after filtering as illustrated in Figure 4-10.

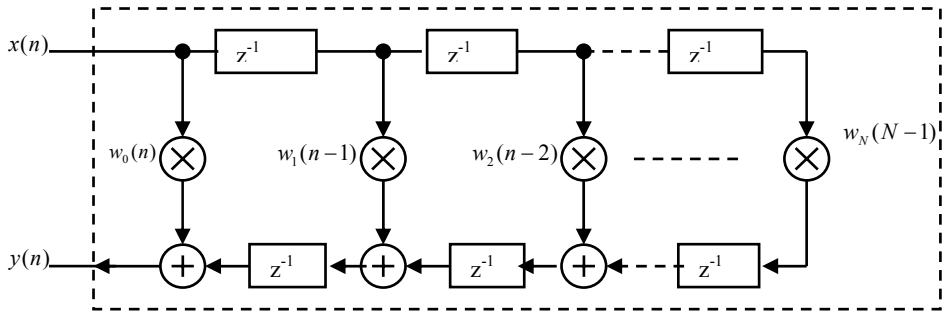

Figure 4-10. Pipelining architecture.

The odd and even coefficients are grouped separately to allow for retiming of the up-sampler. Figure 4-11 shows the modified version of Figure 4-10 in which the number of coefficients is assumed to be odd.

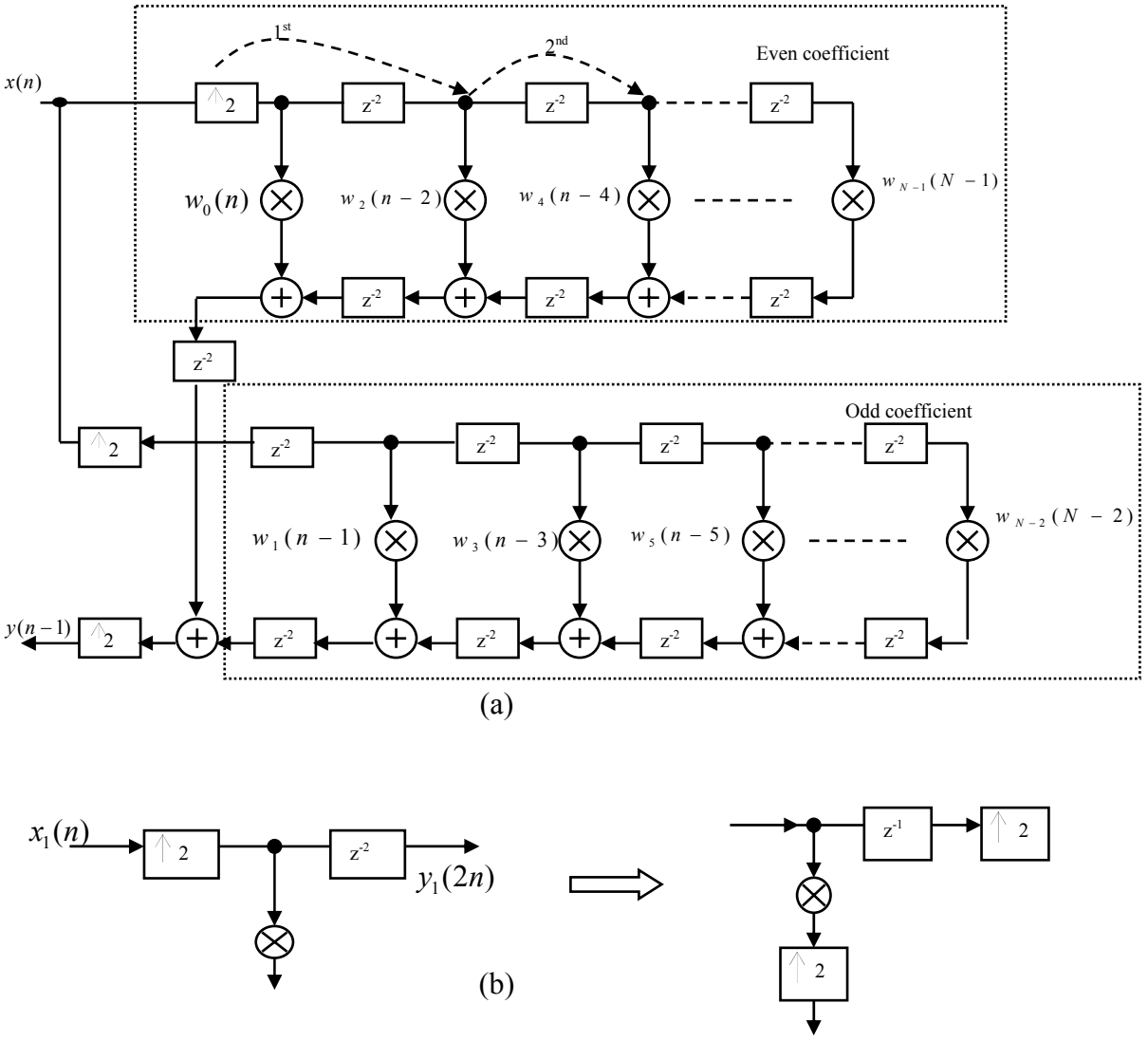

Figure 4-11. (a) Classification of coefficient, (b) Retiming the up-sampler.

Viewing only the even coefficient section, the time execution for the up-sampler circuit can be reduced by 1 cycle for each coefficient multiplication and addition (i.e., from z^{-2} down to z^{-1}) as illustrated in Figure 4-11 (b). The final pipeline architecture for coefficient classification in a form of tree structure is shown in Figure 4-12 [54] and the update coefficient is given by:

$$w(n+1) = w(n) + \mu e(n-2)x(n-2) \qquad \textbf{(4-29)}$$

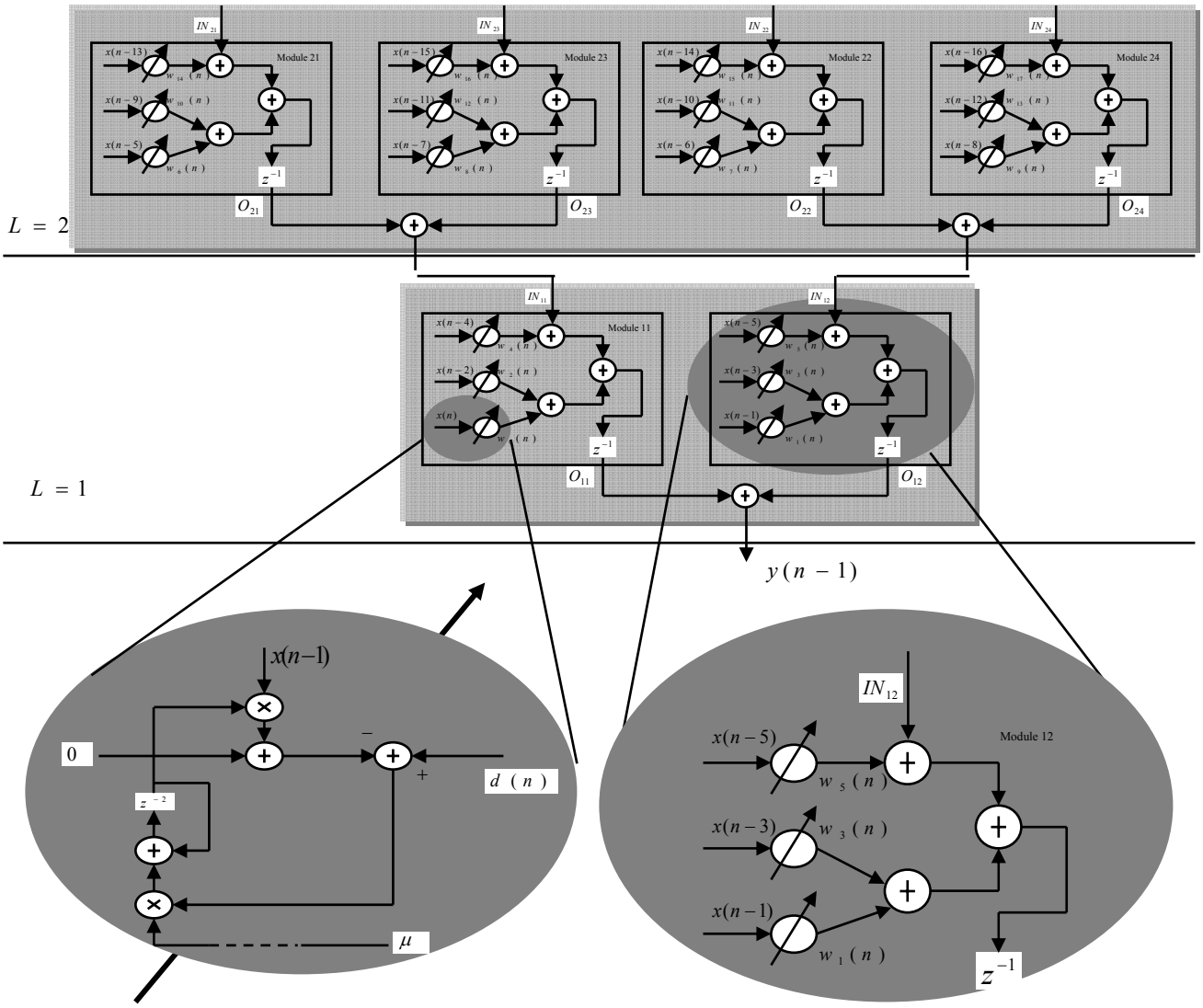

Figure 4-12. Two levels (L =1,2) pipelined coefficient classification using a tree structure.

The method of coefficient classification appears under tree levels structure, where all the coefficients in the same level have the same coefficient delay.

The maximum number of levels Max_L is given by:

$$Max_L = l(N) = \text{ceil}\{\log_2\{1 + 0.5 \otimes ceil(N/3)\}\} \qquad \textbf{(4-30)}$$

where ceil(y) is the smaller integer not less than y (i.e., ceil(0.235)=0.2 < 0.235) and N is the filter length. This maximum level can be achieved if each module has a

maximum of three coefficients as shown in Figure 4-12. Each level L has 2^L modules, whereas each module m_{L_j} with a module number L_j has the filter coefficients with a coefficient delay equal to the level number. The arbitrary numbering of the modules is such that their first coefficients are in an increasing order. The coefficients w_{L_j} in each module j (i.e., j=0,1,….., 2^L) are given in a more general form as

$$w_{L_j} = \lfloor w_{\alpha_{L_j}} \quad \mathrm{w}_{\gamma_{\mathrm{L_j}}} \quad \mathrm{w}_{\beta_{\mathrm{L_j}}} \rfloor \tag{4-31}$$

where $w_{\alpha_{L_j}} = j - 1 + 3\sum_{l=1}^{L-1} 2^l$, $w_{\gamma_{L_j}} = \alpha_{L_j} + 2^L$ and $w_{\beta_{L_j}} = \alpha_{L_j} + 2^{L+1}$. The input signals of the multipliers with coefficients $w_{\alpha_{L_j}}$, $\mathrm{w}_{\gamma_{\mathrm{L_j}}}$ and $\mathrm{w}_{\beta_{\mathrm{L_j}}}$ are $x(n-\alpha_{L_j}+L-1)$, $x(n-\gamma_{L_j}+L-1)$ and $x(n-\beta_{L_j}+L-1)$ respectively.

Table 4-2 shows the comparison of computational complexity between different architectures for the adaptive FIR filter when the correction factor is in consideration. T_M and T_A are the multiplication and addition time, N is the filter length, m_1 is the unit delay and m_2 is the number of step to look-ahead and Sum_A, S_{r2} are defined as:

$$Sum_A = \sum_{i=0}^{l(N)-1} 3.5 \otimes 2^i + T_{na} \tag{4-32}$$

where

$$T_{na} = \begin{cases} (\psi_N - 0.5) \otimes \psi_N + R_m & \psi_N \neq 0 \\ floor(R_m) & \text{otherwise} \end{cases} \tag{4-33}$$

and

$$\psi_N = floor\left(\frac{N_{Max_L}}{2^{l(N)}}\right) \tag{4-34}$$

N_{Max_L} is the upper bound of the maximum number of level and R_m is the remaining number of coefficients is given by:

$$R_m = N_{Max_L} - 2^{l(N)} \otimes \psi_N \tag{4-35}$$

The number of adders S_{r2} within the filtering section using the tree-structure is given by:

$$S_{r2} = \sum_{i=0}^{l(N)-1} 2 \otimes 2 + T_{ra} \tag{4-36}$$

in which

$$T_{ra} = \begin{cases} 2^{l(N)}\, floor\left(\frac{\psi_N}{2}\right) + R_m & \psi_N \neq 0 \\ 0 & \text{otherwise} \end{cases} \tag{4-37}$$

Table 4-2. Comparison of the characteristics of different architectures.

Architecture	Critical Path	Latency	Number of hardware elements		
			Adder	Multiplier	Delay Element
Ideal LMS (Conventional implementation)	$2T_M + NT_A$	1	$2N$	$2N$	$2N$
DF-DLMS (Long [57])	$T_M + T_M$	N	$2N$	$2N$	$6N$
TF-DLMS (Meye [62])	$T_M + 2T_A$	N	$2N+1$	$2N$	$9N$
DLMS-CT2 (Douglas [63])	$T_M + 2T_A$	N	$3N+1$	$5N$	$6N$
RLA-LMS (Shanbhag [56])	T_A / m_2	m_1	$2N+1+N$ (LA-1)	$2N$	$2m_1 + m_2 + 3N$ +LA-1+ $2^{m_2} Nm_2$
CC-LMS (Okello [58])	$T_M + 2T_A$	1	$N+3l(N)+Sum_A+1$	$2N+2l(N)+1$	$2N+3l(N)+\sum_{i=1}^{l(N)} 2^i + 1$
			$N+S_{r2}+1+3l(N)$		

In comparison to other modified pipelining adaptive algorithms, the coefficient classification method achieves a high throughput with only two delays. The maximum delay after a change in the last coefficient which seen at the output of the coefficient classification is significantly reduced. The optimum delay achieved by re-arranged the

time delay is shown in Figure 4-11 and classified the even and odd coefficients into two different stages is shown in Figure 4-12. The number of delay elements is reduced noticeably making the coefficient classification architecture far much more advantageous than the other proposed architectures. In [54], the authors demonstrated the reliability of the coefficient classification by carrying out a number of simulations. The pipeline coefficient classification architecture is not only reliable for FIR adaptive filter but is also well suited with the IIR adaptive filter.

Next section shows the procedure finding optimum parameters in the LMS adaptive filter using *Simulink*® platform. This is a part of the hardware implementation design where the design could be tested in the *Matlab/Simulink* platform before hardware implementation.

4.5 Pipeline LMS Adaptive Parameters Optimization

A set of thorough simulations was conducted in this section to determine optimum adaptive algorithm for narrowband estimation, timing and speed requirements for FPGA implementation. The choice for optimum adaptive filter was carried out by a numerous simulation trials on different types of modified adaptive algorithms. Performance was measured by the mean square error (MSE) and mean square deviation (MSD) with three filter lengths (N=16, 32, 64) and a fixed step-size μ of 0.03125. Figure 4-13 show simulation results in graphical form: The length N is equivalent to the number of filter's coefficient. The concept of filter length is interpreted in a different way between the adaptive and non-adaptive filter. The adaptive filter length converges at a certain point and mainly depends on the characteristics of the signal whereas the length of non-adaptive filter never converges and its performance proportional to the filter

length. The study of each filter convergence factor represents by the learning curve. The curve indicates the convergence region, thus the selection of the convergence factor would become much easier. The choice of filter length and step-size is to be discussed later in the following section.

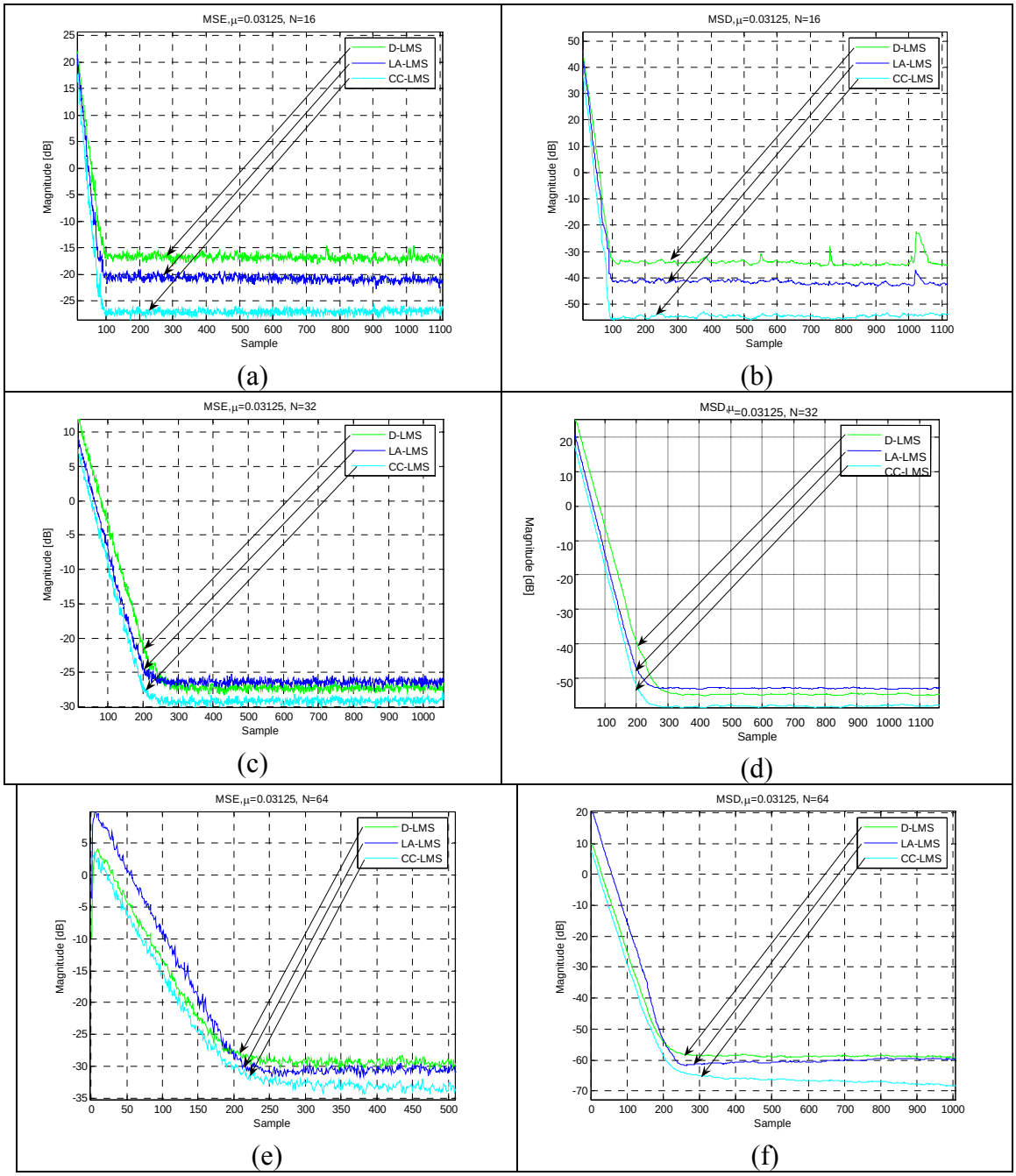

Figure 4-13. Learning curves for the (a, c, e) Mean square error, (b, d, f) Mean square deviation.

Simulation results show that the Delay LMS and Look-ahead LMS having similar performance. However, the Coefficient Classification is better in term of speed and estimation capability. The filter performance measurement is based on the mean square error between the desired and estimated signals.

There are a number of factors in the pipeline LMS NB estimator which need to be determined for an optimal NB estimating operating. These include:

(i) Variation of the input signal power;

(ii) Filter length, N;

(iii) Step size, μ;

Variation of the input signal power affects the rate of convergence, steady-state performance and stability of the estimator output. The modified pipeline LMS coefficient classification algorithm known as a technique independent of the input signal power and capable of optimizing the speed of convergence while maintaining the desired steady-state performance. The procedures which are used to decide the key parameters of the pipeline LMS filter will be described in the following section.

4.5.1 Effect of Filter Lengths on Estimator Performance

Filter length N is the main parameter which can be used to trade computational complexity with filtering performance. An increase in the filter length requires additional hardware which possibly degrades system throughput rate (i.e., introduce more delay) whereas a short filter may have an unsatisfactory filtering performance. Unlike the non-adaptive digital filter, in which its performance proportional to the filter length, however, the adaptive filter length require carefully choice. There is a more

complicated relationship in adaptive filters such as coefficient weight vector noise which can affect the filter steady-state performance. Filtering performance needs to be examined with respect to the effect of filter length on the convergence rate and steady-state performance (i.e., SNR improvement).

Figure 4-16 shows a narrowband estimation with analog to digital converter (ADC) at a sampling rate equals to 6 times the narrowband bandwidth, pipeline coefficient classification adaptive technique was applied. Five filter lengths of 8, 16, 32, 64 and 128 weight taps were investigated. The step size of each filter was fixed at $\mu =$ 0.03125.

Simulation results shown in Figure 4-14 indicate that a 32 weights filter is sufficient to achieve a reasonable convergence. When comparing convergence speed of the filter length to the same level of MSE, a long filter length exhibits slower convergence than a short filter length. Longer filter length offer advantage of higher improvement in SNR. Filter length with more than 64-weight taps experience very little improvement. A 64-weight tap pipeline LMS estimator is found to be a good compromise between convergence performance and hardware complexity.

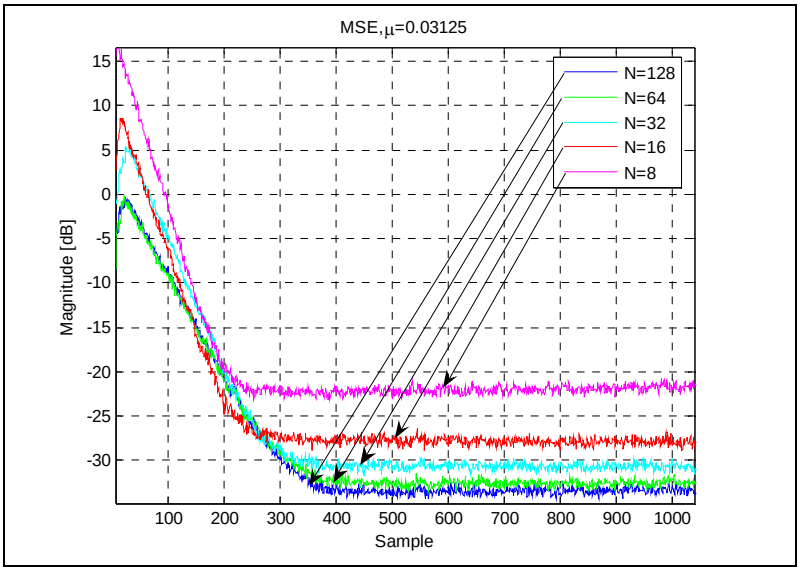

Figure 4-14. Effect of filter length N with ADC sampling rate equal to 6 times NB bandwidth, step-size μ = 0.03125.

Next section covers step size which is the last convergence factor of the pipelined LMS filter.

4.5.2 Effect of Step Size of The Filter on Estimator Performance

Step size governs the convergence speed within a certain stability region. A large step size speeds up adaptation process but produces more internal adaptation noise in the algorithm due to larger misadjustments. An optimal step size must be sought to give best performance for the NB estimator. Multiplication of the step size with an error term (i.e., $e(n)x(n)$) in the algorithm can be replaced by a bit-shift operation using shift registers in hardware. This structure avoids the use of a true multiplier which requires extensive hardware to implement. A 4-bit shift register structure is shown in Figure 4-15. This multiplier comes with the restriction of the value of μ is compromised to the rise power of $\frac{1}{2}$, such as 0.5, 0.25, 0.125, 0.0675, 0.03125. In general, μ is computed as $\left(\frac{1}{2}\right)^n$ where n is a positive integer.

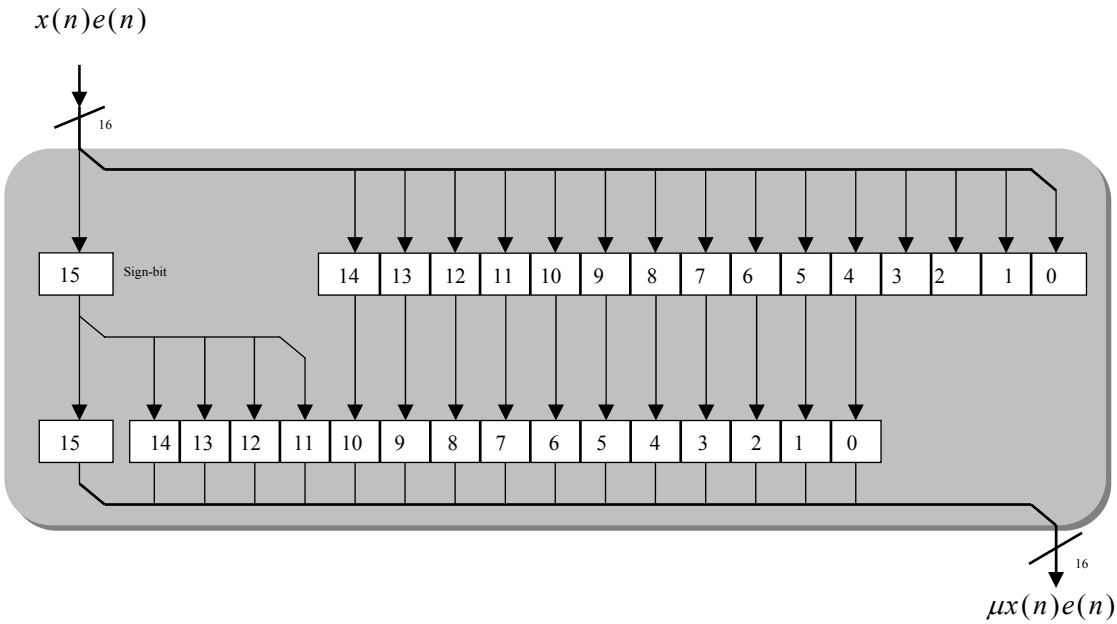

Figure 4-15. Example of 4-bit shift to perform multiplication by μ.

Simulation results shown in Figure 4-16 clearly indicate that a large step size producing considerably more adaptation noise (i.e., poorer interference to noise ratio (INR) improvement) while a small step size results in a long convergence time. The optimal result in terms of convergence speed and steady-state performance lies inside the step size ranging from 0.03125 to 0.0675 for $N = 64$.

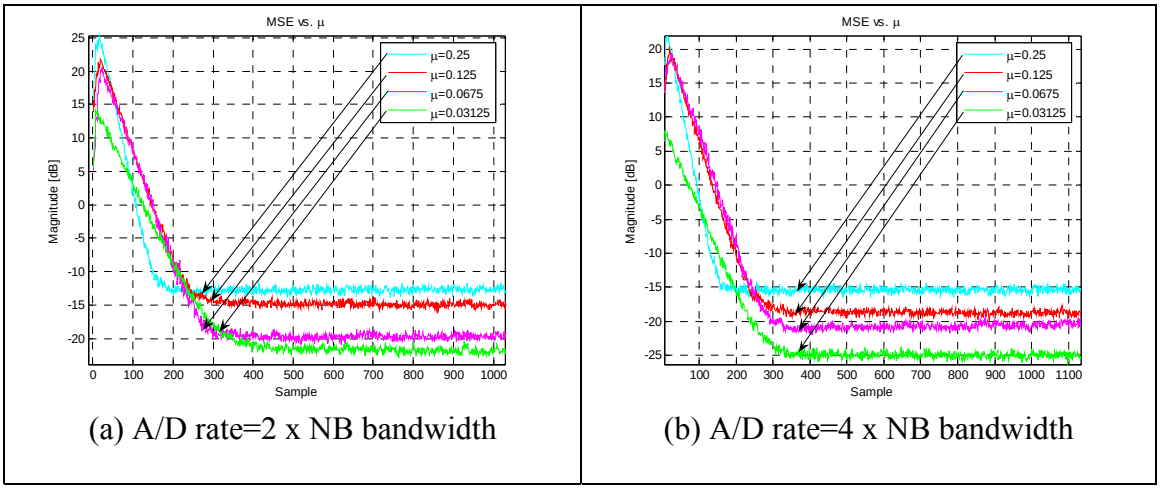

(a) A/D rate=2 x NB bandwidth

(b) A/D rate=4 x NB bandwidth

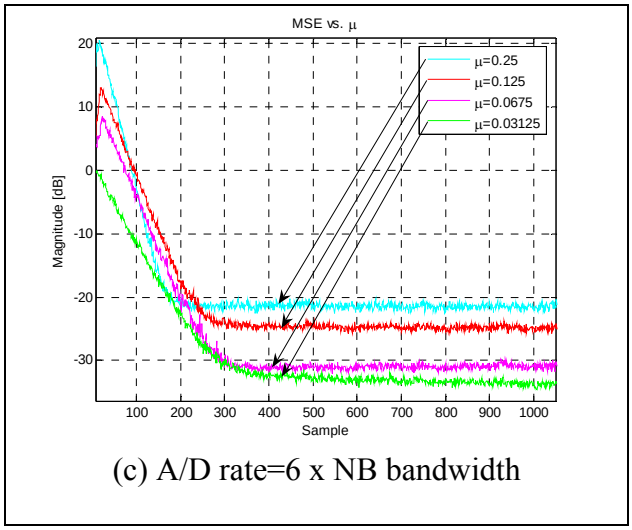

(c) A/D rate=6 x NB bandwidth

Figure 4-16. Effect of step size on different A/D converter rates for a 64-tap pipeline coefficient classification LMS filter.

4.6 Summary

This chapter presents the NBI cancellation circuit using a combination of digital and analog processings. The sampling rate commensurates with the NB bandwidth rather than the NB frequency or UWB bandwidth. The NB estimation takes place in digital form using a LMS adaptive filter. This chapter also reviews characteristics of the LMS-based algorithms, the Stratix FPGA family and the methodology to implement LMS adaptive filter in FPGA technology. The overall aim is to choose an algorithm that offers the best INR enhancement for the NB estimation. In addition, it is important to determine suitable pipeline hardware platforms on which high speed pipelined algorithms can be implemented.

A study of adaptive filters shows that the LMS algorithm is a good choice due to its stable performance and high speed capability. The processing speed of the algorithm can be further improved by adopting its pipelined versions. These pipeline enabled LMS

algorithms provide a better solution for adaptive filter when integrated in the front-end of UWB receivers where high-speed processing is crucial.

DSP chips are not compatible in the UWB system since they only operate in the megahertz range. FPGA devices provide an optimum solution for high speed signal processings. In addition, FPGA offers a great flexibility in term of cost effective, size efficiency, and reprogrammability. High speed capability and abundant registers in the Stratix family FPGA are ideal for implementing pipelined LMS filters. Among these pipelined algorithms, the RLA-LMS and DLMS algorithms require pipelining of the adder in the dynamic adaptation loop, which cannot be achieved by using the Stratix FPGA. Furthermore, the RLA-LMS and DLMS algorithms require a large FPGA area for the coupling terms that are used to compensate for the pipelining effect. This may result in a longer critical path, especially for the interconnect delay associated with the critical path. Obviously, the Coefficient Classification based algorithm is a better choice for FPGA implementation since it noticeably reduces latency and offers higher speed.

This chapter also describes frequency estimation using the method of Moment and method of Maximum likelihood. The need to estimate frequency of carriers in the gigahertz range requires extremely high sampling rate. However it is possible to perform the estimation of the interferer frequency using an intermediate frequency at lower sampling rates.

Chapter 5 Simulation Set-Up and Results for NB Cancellation

In this chapter, first the simulation set-up is described and followed with the simulation results. The chapter ends with analysis and discussion of the simulation and its results.

5.1 Simulation Set-Up

A simulation model was constructed on personal computer (PC) equipped with *MATLAB Simulink®* and *Altera DSP Library*. *MATLAB Simulink®* was used to generate the UWB signal $y(t)$ and the NB signal $s(t)$ presented in Chapter 2. *Simulink* was used to develop the NB detector presented in Chapter 3. The *Altera DSP* library was used to construct a pipelined LMS algorithm described in Chapter 4. The block diagram of the simulation is shown in Figure 5-1 below.

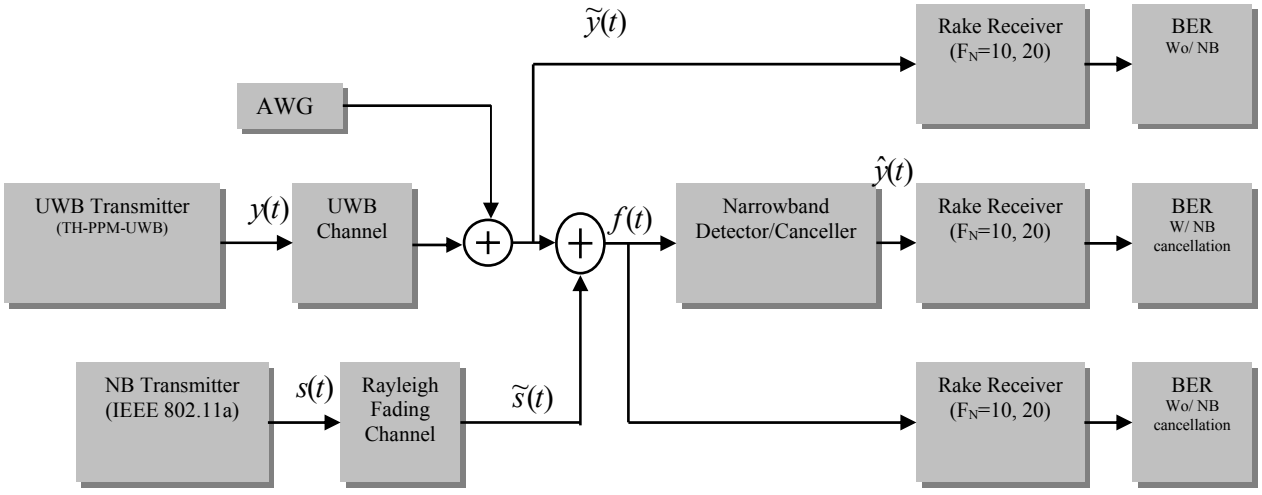

Figure 5-1. Simulation block diagram.

As shown in the simulation block diagram, the signal $y(t)$ after passing through UWB communication channel plus AWGN becomes $\tilde{y}(t)$. The NB signal $s(t)$ after passing through NB communication channel becomes $\tilde{s}(t)$. Signal $f(t)$ is the result of the addition between $\tilde{y}(t)$ and $\tilde{s}(t)$. The NB signal is being detected from $f(t)$ and cancelled if it is detected. Signal $\hat{y}(t)$ is the UWB signal recovered after NB cancellation. The symbol F_N denotes the number of fingers of the rake receiver.

Figure 5-1 shows three methods to collect the results. The top block *BER Wo/NB* provides the results when there is no narrowband signal added into the UWB system. The central *BER W/NB cancellation* block gives the results after the NB is cancelled from the UWB system. The *BER Wo/NB cancellation* gives the results without NBI cancellation. These simulation results are available in section 5.4.3.2 to be compared with the NB detection analysis in Chapter 3.

Details how to construct UWB and NB transmitters are available in Chapter 2. Other simulation building blocks such as UWB channel, Narrowband canceller and Rake receiver will be briefly described in the following sections.

5.2 Construction of the UWB Channel in *Simulink*

The Figure in 5-2 stimulates the UWB indoor dense multi-path channel. The impulse response is calculated based on the 4 UWB channel models (CM1-CM4) from IEEE P802.15 as described in Appendix A. This block also adds the white Gaussian noise $w(t)$ as shown in Figure 5-2.

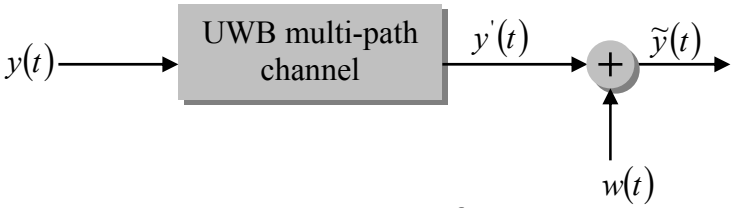

Figure 5-2. A block diagram of UWB channel.

System functions (S-functions) are used to construct this UWB multi-path channel block. S-functions in *Matlab* provide a powerful mechanism to extend the capabilities of *Simulink*®. The functions allow user to add custom built blocks to *Simulink* models. A S-function built UWB channel interface in *Simulink* is shown in Figure 5.3 which can stimulate any 4 channel realizations.

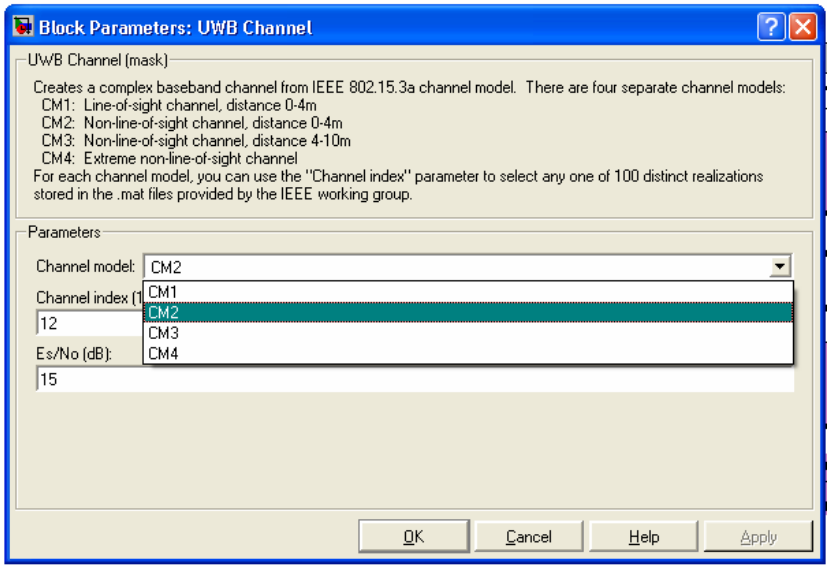

Figure 5-3. S-function UWB Channel.

The use of S-function to build UWB channel is illustrated in Figure 5-4. The channel also includes several built-in block functions such as pseudorandom generator to generate additive white Gaussian noise and functions to calculate signal to noise ratio.

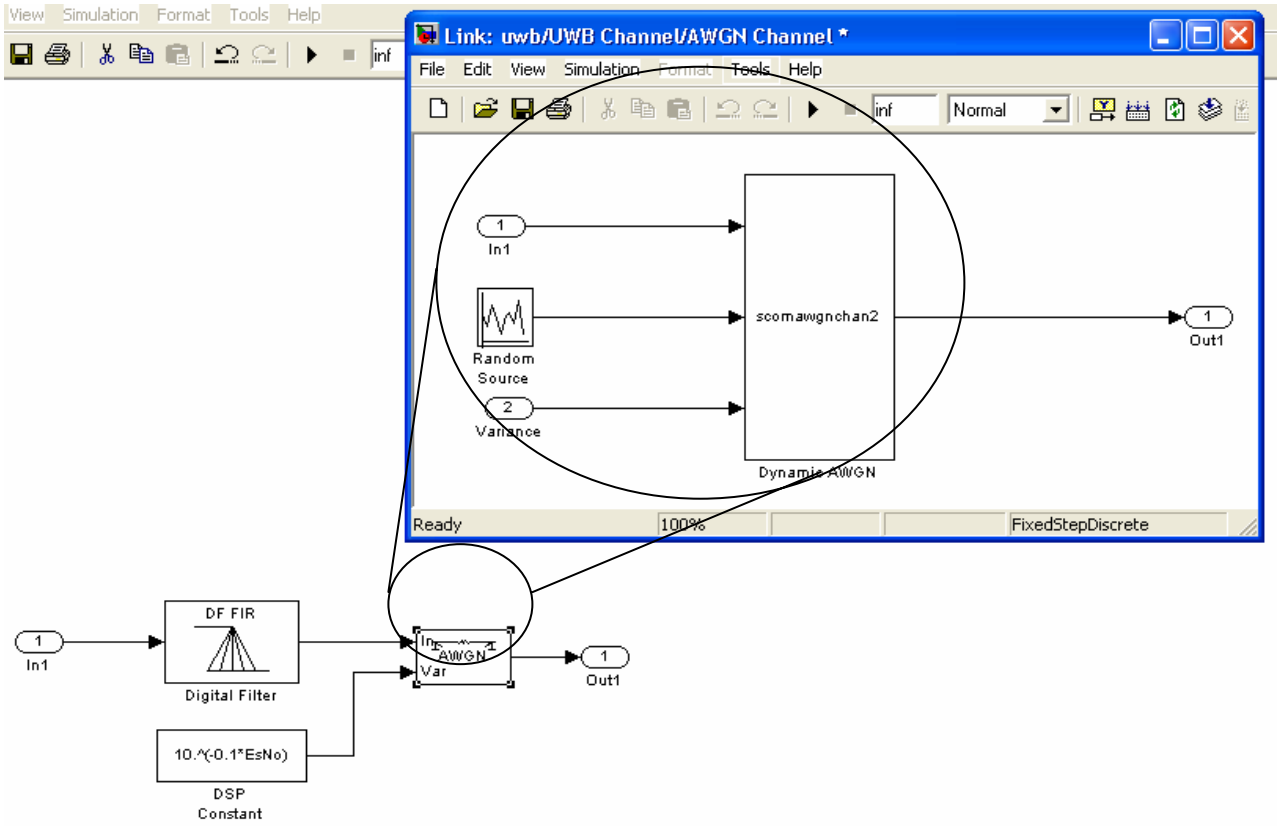

Figure 5-4. UWB channel.

Regarding how much noise to be injected into the system, the signal energy of $y'(t)$ is required to be known prior. However, this assumption is not applicable to UWB channel models in IEEE P802.15. When the signal passes through the channel, its energy is reduced. If this reduction exhibits a fixed relation with the original signal then signal energy of $y'(t)$ can be calculated based on the signal energy of $y(t)$. If only one realization of the UWB multi-path channel is used in simulation, then the reduction is a fixed relation because the lost factor could be found. However, for simulation accuracy, a sufficient number of channel realizations must be used. Every time a simulation is run, the channel realization must be re-calculated.

Although using the same channel model defined with same statistical parameters, the channel realization of every simulation is generated randomly using the same statistical parameters. Therefore the exact relation of this change cannot be obtained. The solution for this is using an average value of the signal energy of $y'(t)$. In this simulation, 100 realizations of one channel model were calculated and this average signal energy of $y'(t)$ was used to decide how much noise is to be added. The channel responses are shown in Figure 5-5 according to the parameters measured by the IEEE P802.15 group shown in Table 5-1. The parameters in the table are defined in Appendix A.

Table 5-1. Parameter setting for the IEEE UWB channel model.

Scenario	$\Lambda(1/ns)$	$\lambda(1/ns)$	Γ	γ	$\sigma_{\zeta_1}(dB)$	$\sigma_{\xi_2}(dB)$	$\sigma_g(dB$
CM1 LOS (0-4 m)	0.0233	2.5	7.1	4.3	3.39941	3.3941	3
CM2 NLOS (0-4 m)	0.4	0.5	5.5	6.7	3.3941	3.3941	3
CM3 NLOS (4-10 m)	0.0667	2.1	14	7.9	3.3941	3.3941	3
CM4 Extreme NLOS multi-path channel	0.0667	2.1	24	12	3.3941	3.3941	3

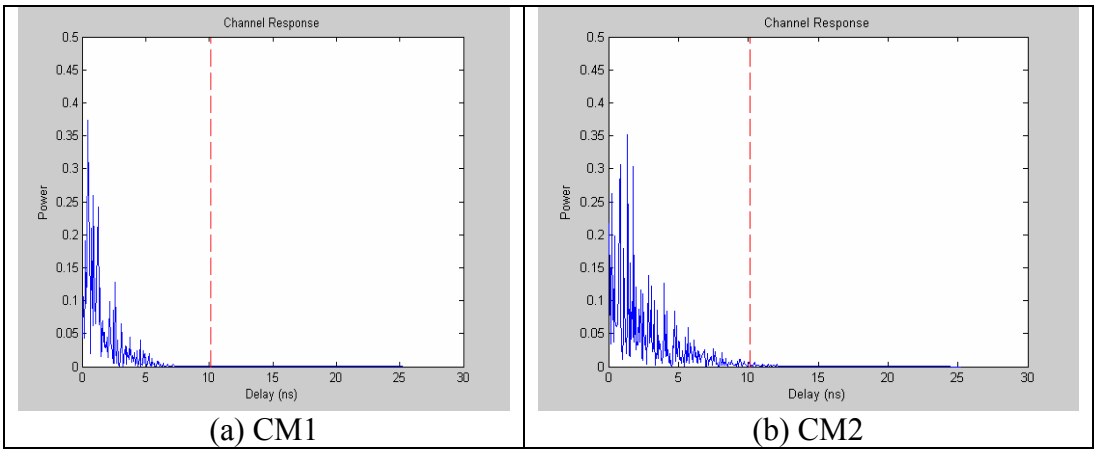

(a) CM1 (b) CM2

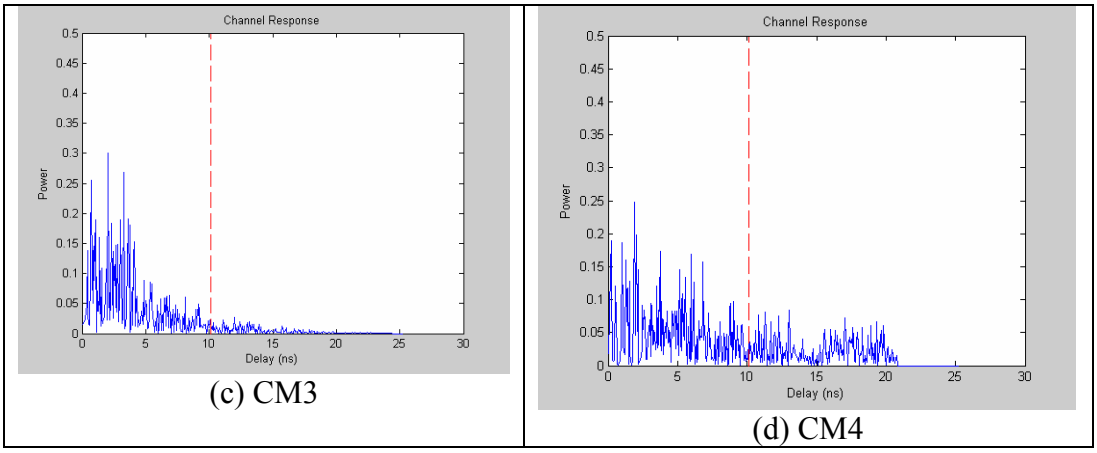

Figure 5-5. Channel realization of 4 different types of UWB channel.

5.3 Construction of the Narrowband Canceller Block

Figure 5-6 shows the implementation of the narrowband cancellation block. The structure was implemented in *Matlab/Simulink*® and *Altera DSP*® block. The *Altera DSP* blocks are embedded using VHDL language. This is similar to the S-function in *Simulink* which is embedded using C language. The difference between these two blocks is the *Altera DSP* can be used to program into any of Altera family FPGA devices while the S-function can not. The inter-connection between the *Simulink* and the *Altera DSP* blocks must follow certain rules and these rules depend on the functions of each *Altera DSP* block.

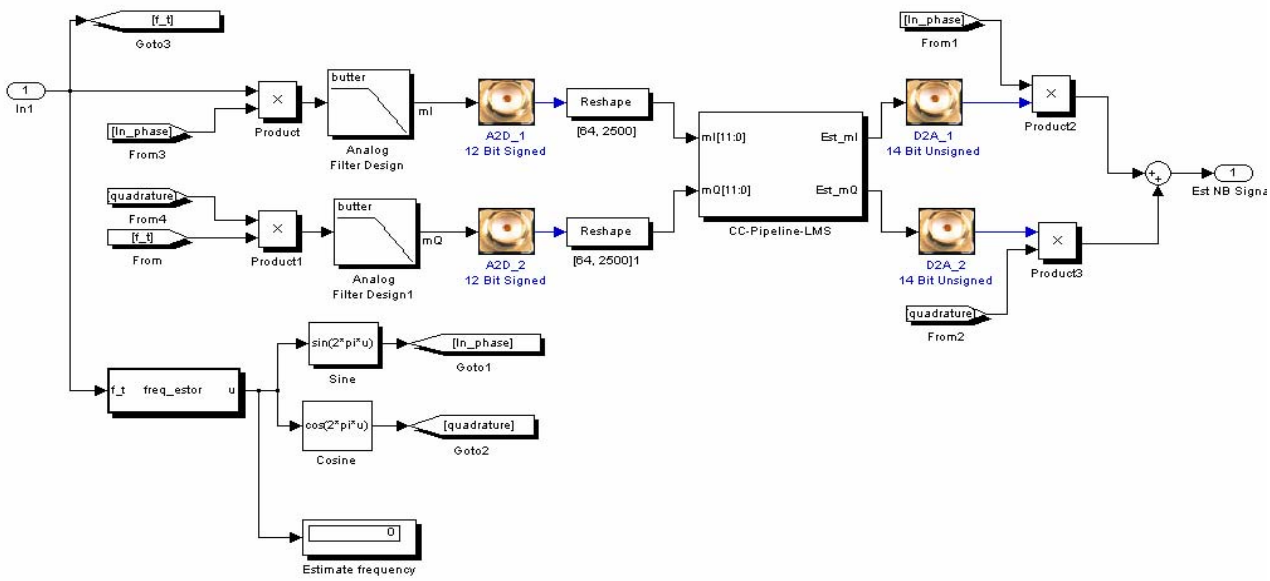

Figure 5-6. Narrowband cancellation structure in Simulink block.

In Figure 5-6, the *Altera DSP* built-in function provided the 12-bit ADC and 14-bit DAC. The other functions came from the existing built-in and custom function (S-function) from *Simulink* library. The pipeline Coefficient Classification LMS (CC-Pipeline-LMS) was fully implemented using *Altera DSP* built-in functions.

The construction of the CC-Pipeline-LMS consisted of several important steps. The implementation of the re-loadable coefficients ultilized *dual-port memory (M4K)* blocks as shown in Figure 5-7. The data stored in *M4K* memory block were interchangeable while reading the past coefficient values and replacing with the new coefficients. The multiplier was implemented by an *8-bit shift register* as shown in Figure 5-8. The 8-bit shift register performs exactly the same way as the 4-bit shift register described in section 4.5.2 except it processes 8 bits per instruction. The correspond *bit level sum of product* is shown in Figure 5-9. The Bit Level Sum of Products block calculates a sum of the multiplication of one-bit input by signed integer fixed coefficients. This block applies the equation:

$$q = a(0)C_o + a(i)C_i + ... + a(n)C_n \qquad \textbf{(5- 1)}$$

where $a(i)$ is the one-bit input data, C_i are the signed integer fixed coefficients and n is the number of coefficients between 1 to 8. Table 5-2 lists the *bit level sum of products* block parameters.

Table 5-2. Bit Level Sum of Products Block Parameters.

Name	Value	Description
Number of coefficients	1-8	Choose the number of coefficient
Coefficient bit width	2-51	Specify the bit width as a signed integer
Coefficient value	User defined	Specify the coefficient values as signed integers
Register inputs	On or Off	When turned on, a register is added on the input signal.

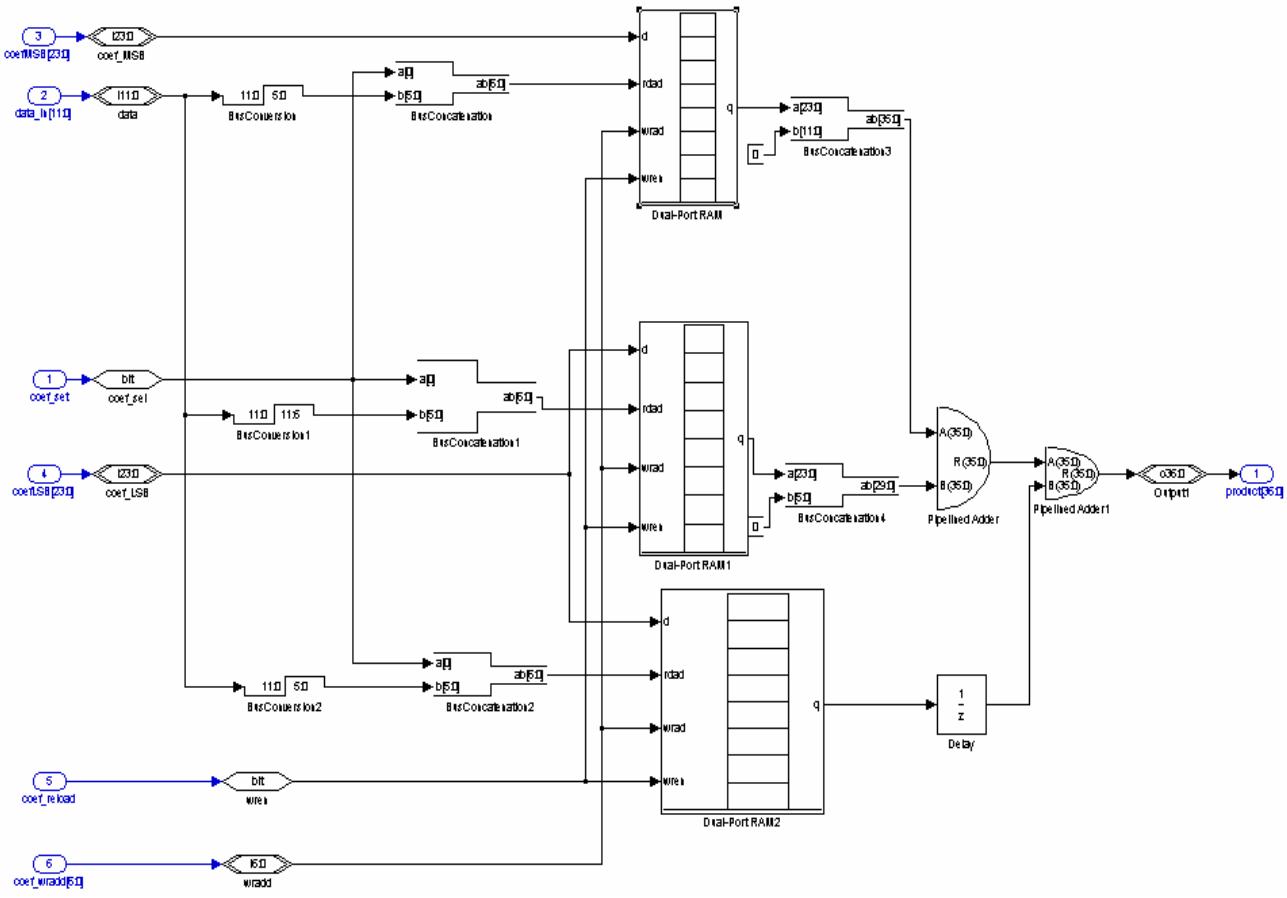

Figure 5-7. Coefficient re-loadable architecture.

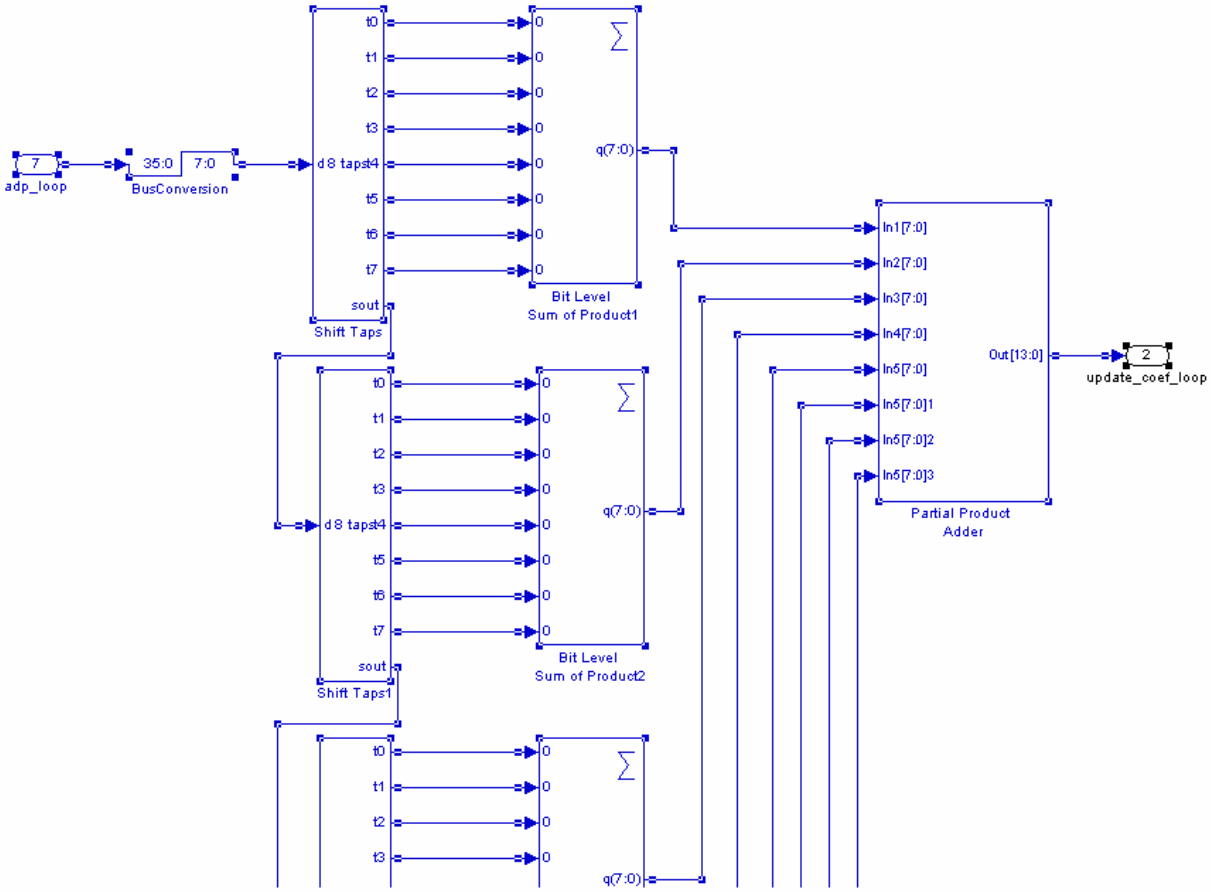

Figure 5-8. 8-bit shift register.

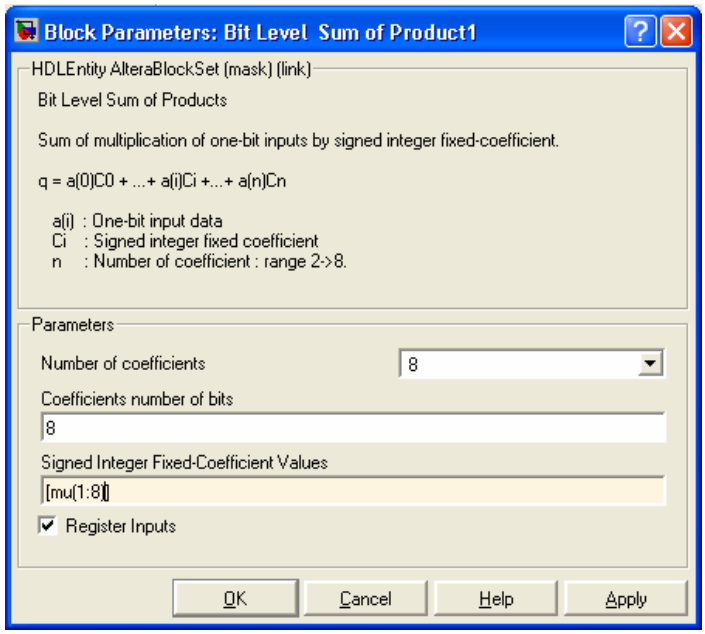

Figure 5-9. Bit level sum of product.

The adder simply uses the built-in *Pipeline Adder* from *Altera DSP* library as shown in Figure 5-10a. The pipelined Adder specification is listed in Table 5-3. This *Pipeline Adder* block also offers subtract operation.

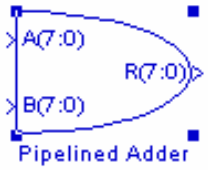

Figure 5-10. Pipelined Adder.

Table 5-3. Pipelined Adder specification.

Name	Value	Description
Bus Type	Signed integer, Signed Fractional, Unsigned integer	Choose the bus number format that use for counter
Number of bits.[]	1-51	Specify the number of bits to the left of the binary point
[].Number of bits	0-51	Specify the number of bits to the right of the binary point for the gain
Pipeline	0-4	Choose the number of pipeline levels
Direction	ADD,SUB	Choose whether the block is used as an adder or subtractor
Use Control Signal	On or Off	When turn on, the rst (reset), ena (clock enable), cin (carry in), and add_su (addition when logic value 1, subtraction when logic value 0) signals are added to the block

5.4 Construction of The Rake Receiver and the BER Block

This section describes constructions of the communication receiver and the bit error rate calculation block in *Simulink*.

5.4.1 The Rake Receiver

The procedure to construct Rake receiver is similar to the implementation of other block functions. The customized S-function is used to implement the Rake receiver. Detailed description and analysis of the Rake receiver is given in Appendix B. Figure 5-11 shows a simplified Rake receiver model. The receiver consists of a parallel bank of correlators (i.e., Match Filter in Figure 5-11), followed by a combiner using either Selection Diversity (SD), Equal Gain Combining or Maximal Ratio Combining (MRC) method (i.e., Pilot Seq, Channel estimation, N-Selective MRC from Figure 5-

11). Each correlator is locked on one of the different replicas due to multipath of the transmitted symbol.

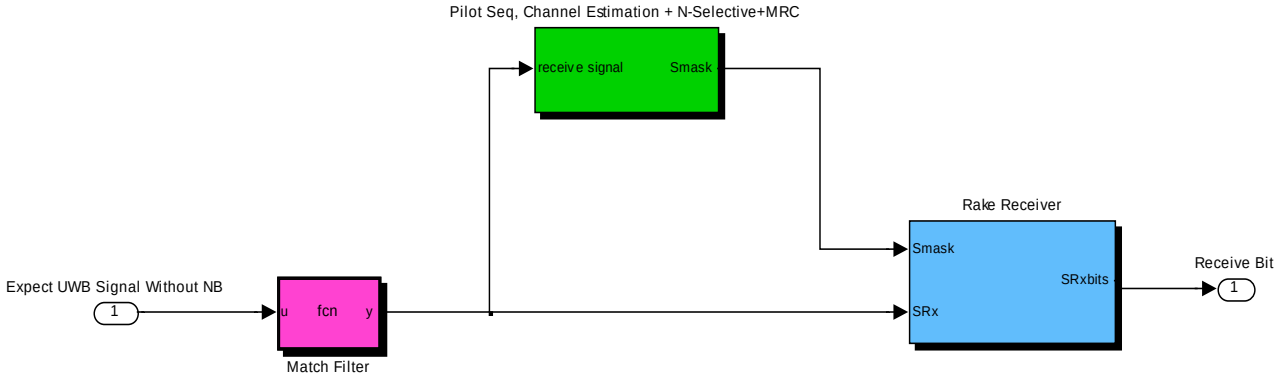

Figure 5-11. Rake Receiver.

The *Expect UWB Signal Without NB* represents either signal $\tilde{y}(t)$, $\hat{y}(t)$ and $f(t)$ as shown in Figure 5-1 and the *Receive Bit* is nothing more than the estimation of the transmitted bit.

5.4.2. The BER Block

The bit error rate (BER) is used to measure performance of the system under operation. The BER block compares the transmitted bits with the received bits and expresses their difference in percentage with respect to the total number of transmitting bits. The BER block shows in Figure 5-12 is taken from the *Simulink* library. One input port is for the transmitted bits and the other is for the received bits. The output port provides three pieces of information, one is the total number of transmitted bits, one displays number of error bits (i.e., the difference between transmitted and received bits) and one is the number of error over the total transmitting bits express in percentage.

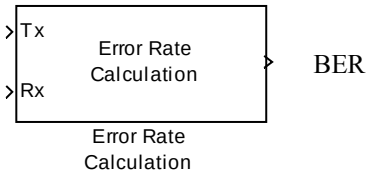

Figure 5-12. BER Simulink Block.

The collection of the simulation results is to be briefly described and discussed in the following section.

5.5 Simulation Results

This section verifies the frequency estimation theory described in section 4.3 and validates the entire system performance.

The frequency estimation performance is measured in terms of the mean and variance of the estimated NB central frequency. The cancellation performance is measured in terms of bit error rate (BER) as a function of SNR. Due to lengthy program runtime required to simulate frequency estimation, the simulation results were the average of 75 runs. Simulation results for the system performance and frequency estimation were obtained from 100,000 information bits.

5.5.1 Frequency Estimation

5.5.1.1 Method of Moment Results

It was mentioned in section 4.3.1 that as f_o approaching to zero, the variance is expected to increase. Figure 5-13a compares the effect of the changing in sampling rate on the variance of the estimated NB central frequency with a known signal amplitude at the central frequency of 5.2 GHz. Figure 5-13b shows the results calculating the mean of the estimated NB central frequency for 3 different sampling rates. The 3 sampling rates under studied varied from 2, 4 and 6 times of the NB central frequency. For simplification, the sampling rate expressed as $F_s = 2x,4x$ and $6x$. As SNR increases, the mean converges toward the correct value. However, at SNR=14, the estimation is still considerably poor for $F_s = 2x$ and $F_s = 6x$. Per discussion in section 4.3.1, this phenomenon is the result of the values near the asymptote slope of the inverse cosine

diverging from the true value. Note that the best performance is at $F_s = 4F_c$ as this is the focal point of the inverse cosine function shown in Figure 4-4 as expected since $f_o = 1/4$ when $F_s = 4F_c$. The following analysis therefore only examines $f_o = 1/4$ for the method of moment.

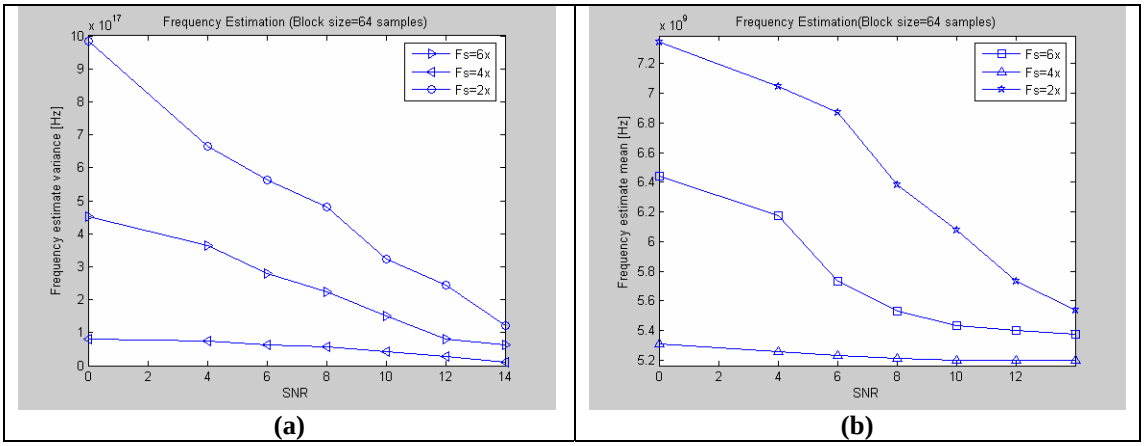

(a) **(b)**

Figure 5-13. Method of Moments Estimation (a) Variance of estimated frequency vs. SNR, (b) Mean of estimated frequency vs. SNR.

Figure 5-14 shows the mean and variance of the NB frequency estimation as a function of different sample sizes and SNR for the method of moments.

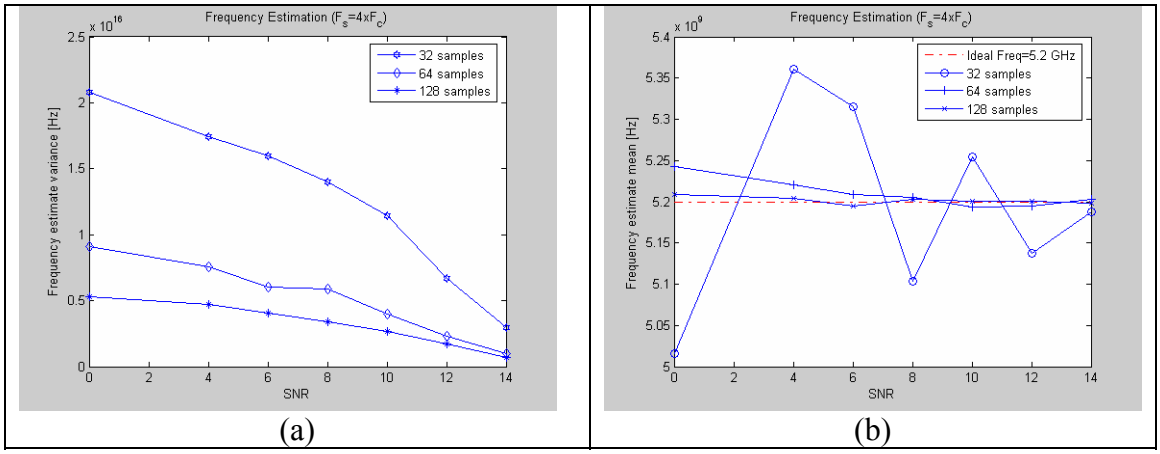

(a) (b)

Figure 5-14. Method of Moment Estimation (a) Variance of estimated frequency vs. Block size for $F_s = 4F_c$, (b) Mean of estimated frequency vs. Block size for $F_s = 4F_c$.

The precise results of the data processing are dependent to the number of samples taken into the calculation. In the other word, more sample takes into the

calculation, the results approach to the ideal frequency which is 5.2 GHz. The frequency estimation results using different number of samples can be seen from Figure 14 [a, b]. The estimate results evaluated with 32 samples are considered worse than the one taken 64 samples or 128 samples. As expected, the variance of the estimated frequency decreases with the increase in sample size and SNR. In addition, the mean slightly fluctuates at 5.2 GHz and more obvious for the smaller sample sizes (i.e., 32 samples). These simulation results were the average of 75 runs. Running the simulation over a larger number, says 100 or 150, would likely bring the mean values even closer to the actual frequency.

5.5.1.2 Method of Maximum Likelihood Estimation Results

The following discussion and results are for Method of maximum likelihood estimation presented in section 4.3.2. The increase in sample size expects to reduce the variance of the estimated frequency. In other word, the more samples take into the calculation the better estimation results would be. Plots of the variance and the mean of the estimated frequency for the increasing in sample size at a sampling rate of $F_s = 6F_c$ are presented in Figure 5-15.

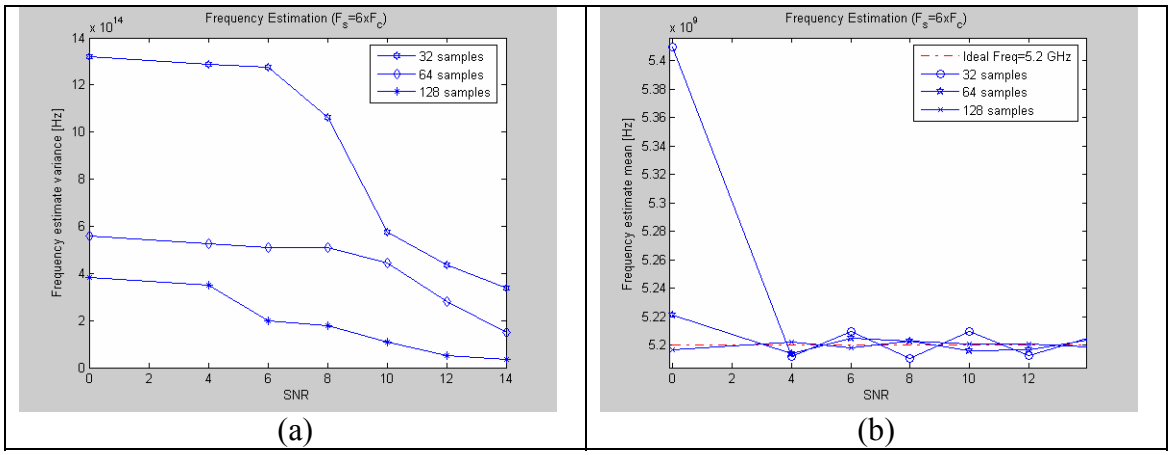

Figure 5-15. Method of Maximum Likelihood Estimation (a) Variance vs. Block size for $F_s = 6F_c$, (b) Mean vs. Block size for $F_s = 6F_c$.

Different from the method of moment estimation, the MLE does not experienced a large fluctuation in the mean estimated frequency as the sampling rate increases but it does exhibit similar types of increase in variance.

In comparison between the two methods, the MLE offers an estimation having lower standard deviation. This suggests that MLE should be the method of choice. However, the MLE is computational intensive simply because of this method requires matrix inversion. As the sample size increase, matrix inversion becomes more complex: This is a drawback in system implementation. For the high SNR scenario, it may be acceptable to use the method of moment to estimate frequency.

5.5.2 Narrowband Cancellation Performance

The results to be presented in this section attempt to quantify the performance of the narrowband canceller in term of bit error rate. Before presenting the results, it is important to provide some general assumptions and definitions used in the simulations. There are three main assumptions for the system: (a) there is no inter-symbol-interference, (b) channel estimation and system synchronization are perfect and (c) there is only one OFDM signal active at 5.1925-5.2075 GHz.

The UWB system was constructed using TH-PPM technique which inherents the following characteristics: the system is transmitting 40 μW of power acquiring a speed of 50 Mbps with a chip time $T_c = 1$ ns using a PPM shift factor of 0.5 ns. The pulse shape is a 2nd order derivative Gaussian pulse having a bandwidth of 4 GHz. CM2 and CM3 channel models from IEEE P802.15 are used.

During the estimation period, the NB estimate algorithm needs time to process causing delay and phase difference for the estimated signal. System calibration must be

performed to ensure correctness of the system performance. In the following sub-sections, simulation calibration was carried out to determine sample delay and phase difference of the estimated signal with respect to the transmitting signal using the Monte-Carlo technique.

5.5.2.1 Simulation Calibrations

In order to cancel out the NB interference effectively, the transmitted signal and the estimated NB signal must be aligned. The system must be calibrated by adjusting or configuring the system to the desired parameter settings. Sample delay and phase offset between the transmitted signal and the estimated narrowband signal are calculated using Monte-Carlo method. The explanation of this method is provided in Chapter 3.

Delay calculation is based upon the cross correlation between the two signals. The cross correlation was found to vary with time therefore it is difficult to determine the correct delay. The Monte-Carlo method was applied to the delay determination process, each delay value was injected into the system until the correct delay value was found. The correct delay value corresponding to the smallest BER. The incorrect delay contributes additional noise into the system: thus the BER is larger compared to the correct delay. The delay calibration shows in Figure 5-16a.

Same procedures were applied to the phase offset determination. Figure 5-16b shows the phase offset calculation vs BER.

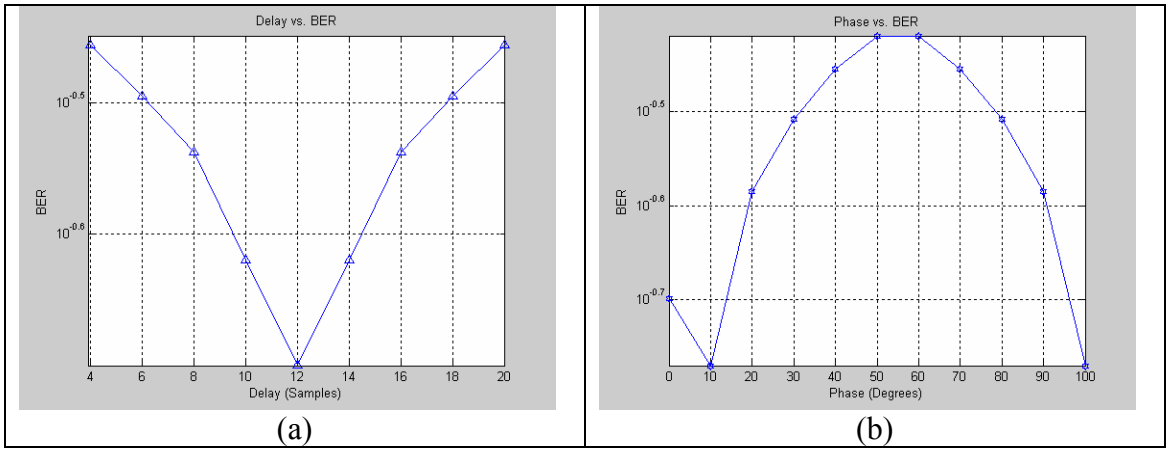

Figure 5-16. (a) BER vs. Delay, (b) BER vs. Phase Offset.

Figure 5-16a indicates 12 sample adjustment yielding the lowest BER value. The 10 and 100 degree phase shift of the estimated narrowband having the lowest BER value are clearly shown in Figure 5-16b. Theoretically, the 45 degree phase shift causes the worse mismatch between the two signals especially in QPSK modulation technique [60] (i.e., the sub-carrier for OFDM symbol is QPSK, see section 2.2). The phase offset measured at 10 degree and the 55 degrees causes the worse mismatch.

The phase shift measurement also reveals another optimum point at 100 degree. The case happened because the signals after down/up conversion are in the form of sine and cosine which having the half cycle at 90 degrees. However, the cosine and sine wave are different by 90 degrees, interchange these two functions after the baseband conversion results in no change of the estimated NB. Thus 100 degrees results from the 90 plus 10 degrees phase shift. The optimum choice either 10 or 100 degrees phase offset is appropriate. The value of system calibration was chosen 12 samples for system delay and 10 degree phase shift between the transmitted and estimated NB signal. The delay and phase offset values were used to set for the delay and phase offset as indicated

in Figure 4-1. The following results were obtained after applied these two calibrate parameters into the simulations.

5.5.2.2 NB Cancellation Results

NB cancellation performance was measured by the bit error rate (BER) and average cancellation gain. BER is the measurement of number bit errors out of the total bit being transmitted. In this simulation, 100,000 bits of data were sent. The average cancellation gain collected from taking the nature logarithm of the ratio of the average between the *NB without cancellation* and the *NB with cancellation* (see section 5.1, Figure 5.1) in dB scale. For example, if X_{av} stands for the average of the *NB without cancellation* and Y_{av} stands for the average of the *NB with cancellation*, then the average cancellation gain is calculated as $-10\log_{10}\left(\frac{Y_{av}}{X_{av}}\right)$. The reason to take the negative of the average cancellation gain is because the results from *NB with cancellation* supposed to be better than the results from *NB without cancellation* in the negative direction.

The collected results include BER without NB interference, BER with NB cancellation and BER without NB cancellation. The average cancellation gain signifies how well the system performs. Since UWB system is power-limited (i.e., transmitted power limited to -41.3 dBm) or energy efficient, extending the SNR to 14 dB is sufficient to determine system performance. Increasing SNR in simulations is equivalent to increase power at the receiver in real applications.

Following figures present the results for channel type 2 and 3 (i.e., CM2, CM3) and imperfect channel estimation using Rake receivers of 10 and 20 fingers. The reason to have 10 and 20 fingers is it is easy to compare with the simulation set-up in [60]. The

author in [60] simulated UWB systems with various interference sources including the ideal UWB system using 10 and 20 fingers. The ideal UWB systems means there is no NB interference and channel estimation is perfect. Figure 5-17 to Figure 5-22 show simulation results of NB cancellation for channel type 2 and Figure 5-23 to Figure 5-28 for channel type 3. The pipelined coefficient classification NB canceller was set with a convergence rate μ of 0.03125 and a filter length $N = 64$.

a) Results with channel type 2 (CM2):

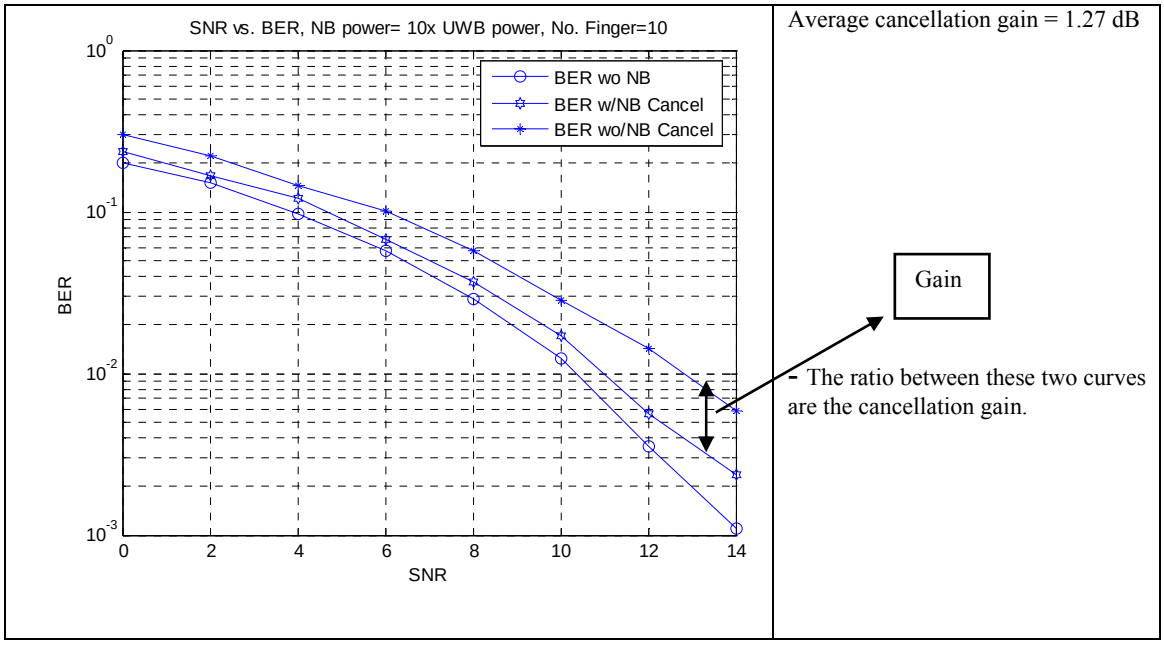

Figure 5-17. SNR vs. BER when NB power = 10 times UWB power, Number of Rake Finger =10.

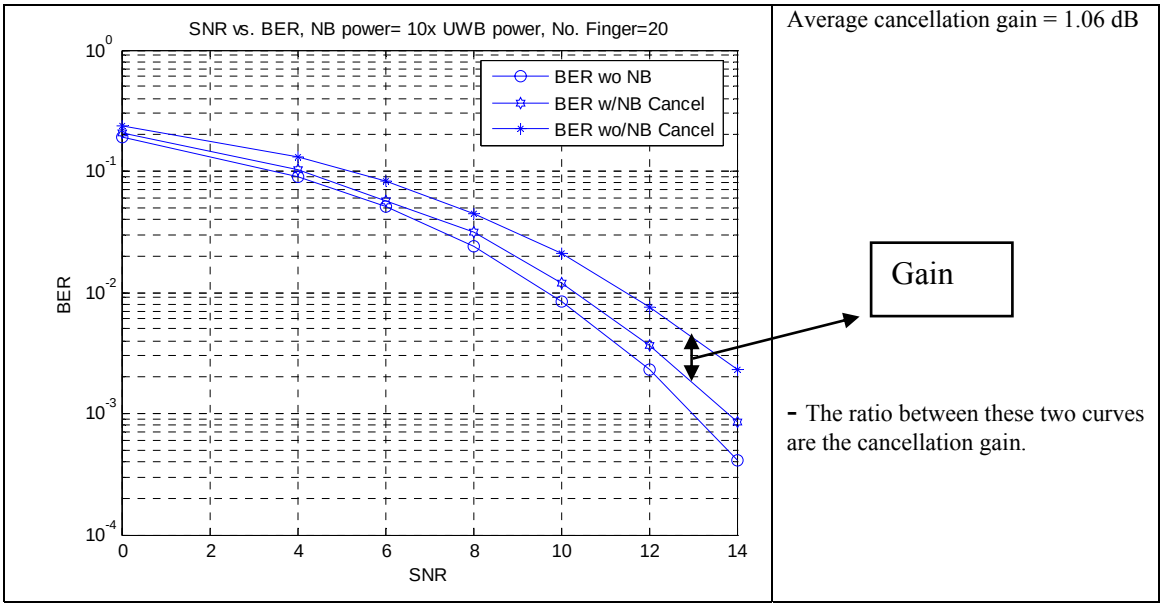

Figure 5-18. SNR vs. BER when NB power = 10 times UWB power, Number of Rake Fingers =20.

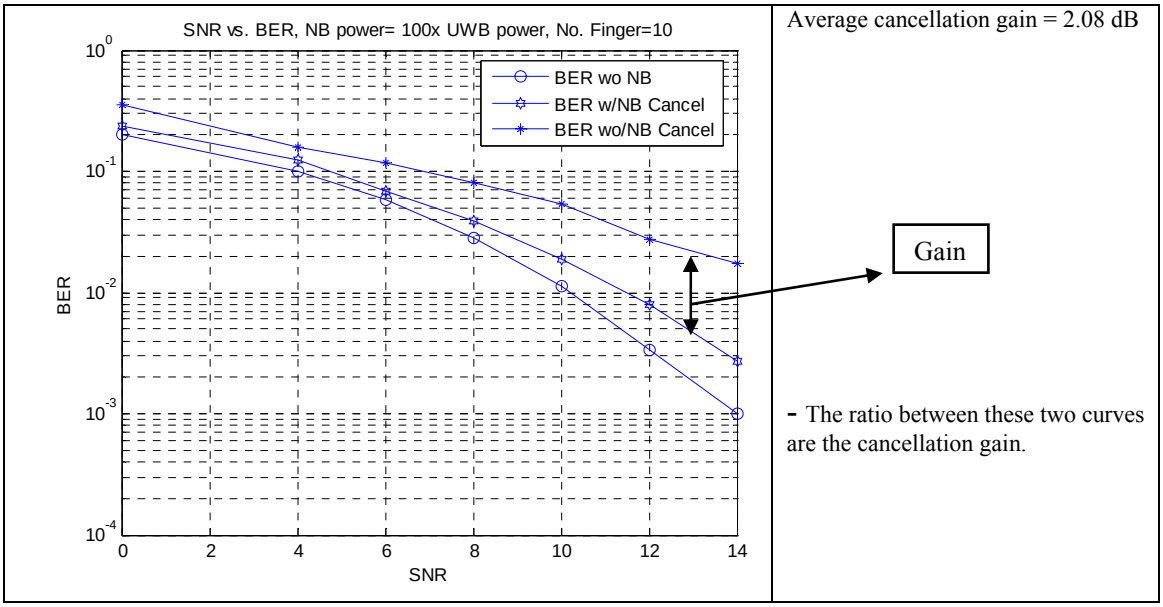

Figure 5-19. SNR vs. BER when NB power = 100 times UWB power, Number of Rake Fingers =10.

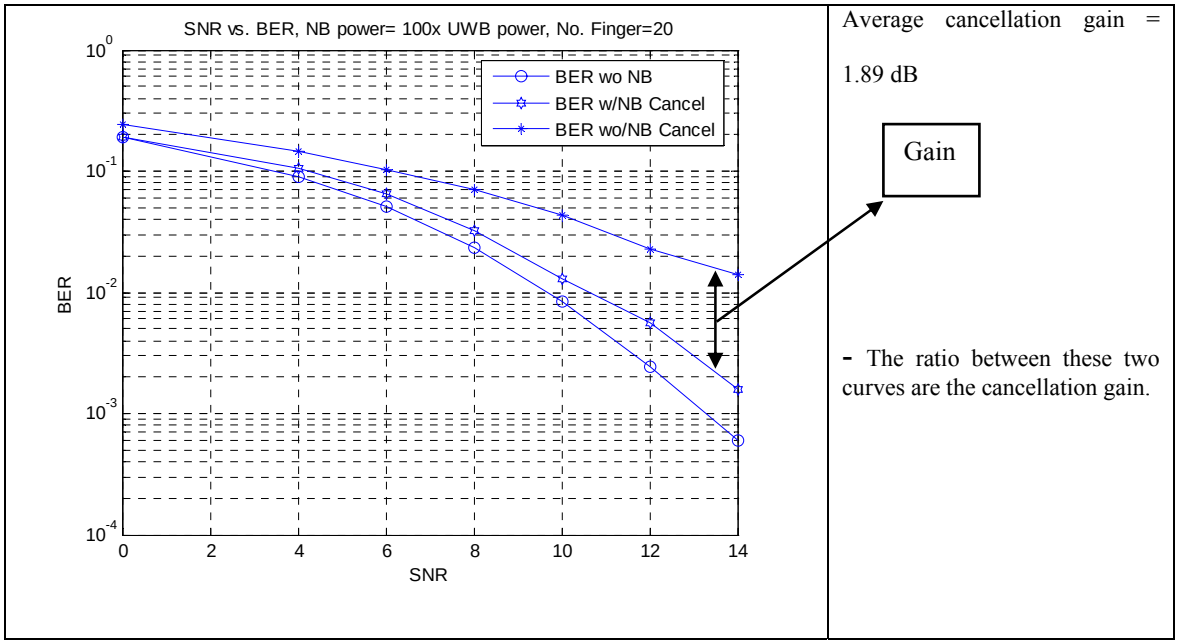

Figure 5-20. SNR vs. BER when NB power = 100 times UWB power, Number of Rake Fingers =20.

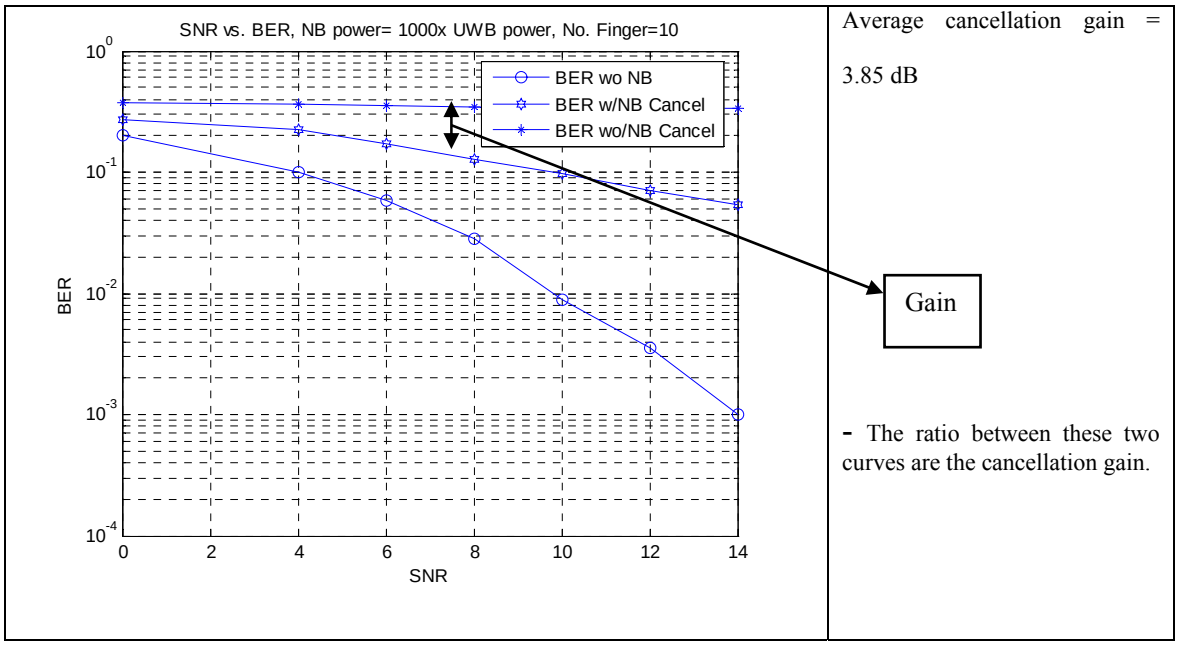

Figure 5-21. SNR vs. BER when NB power = 1000 times UWB power, Number of Rake Fingers =10.

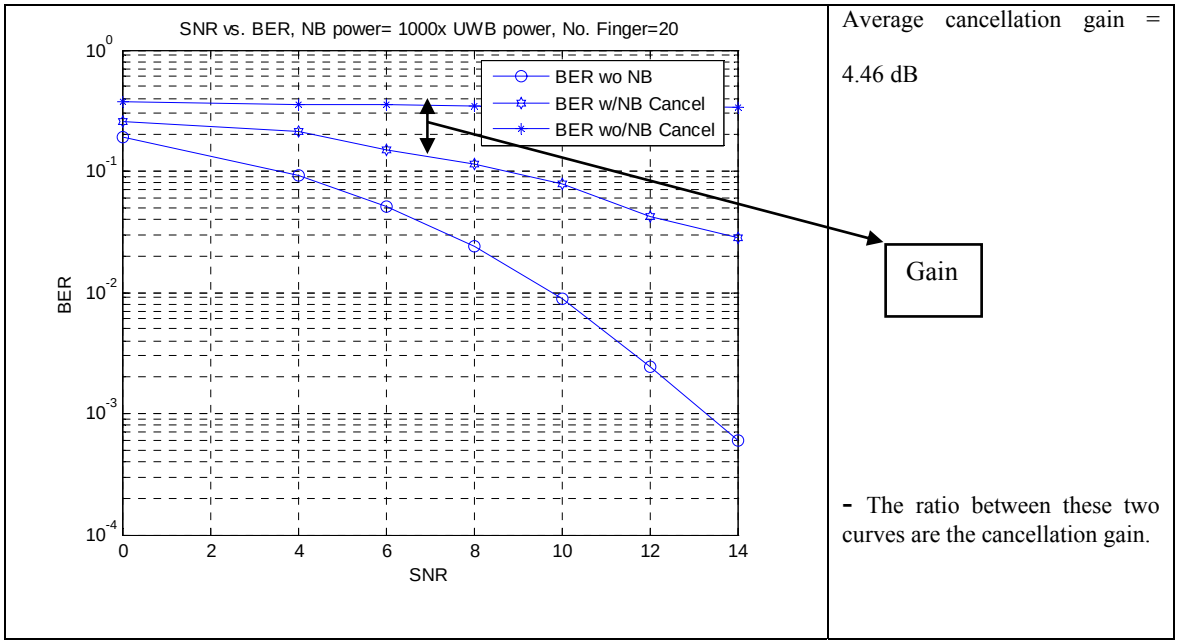

Figure 5-22. SNR vs. BER when NB power = 1000 times UWB power, Number of Rake Fingers =20.

b) Results with channel type 3 (CM3):

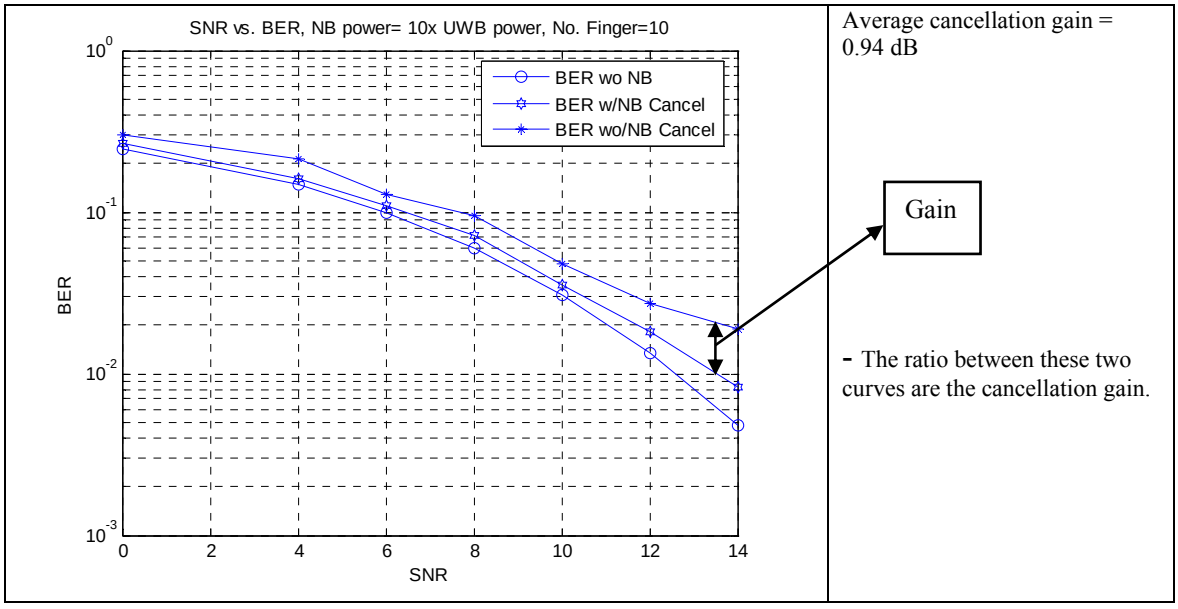

Figure 5-23. SNR vs. BER when NB power = 10 times UWB power, Number of Rake Fingers =10.

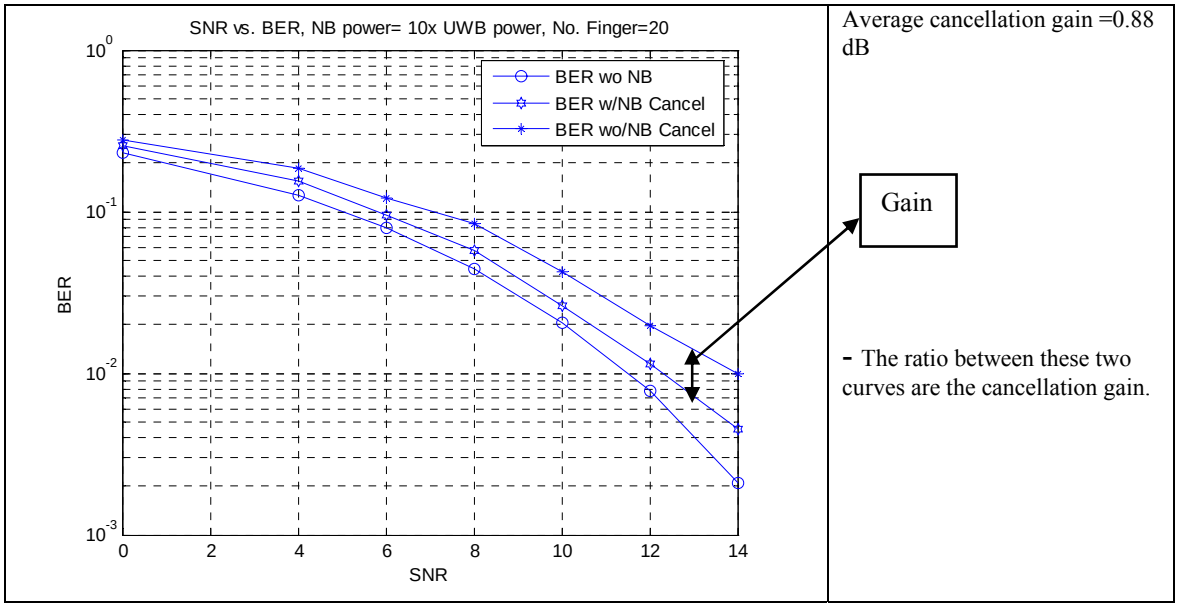

Figure 5-24. SNR vs. BER when NB power = 10 times UWB power, Number of Rake Fingers =20.

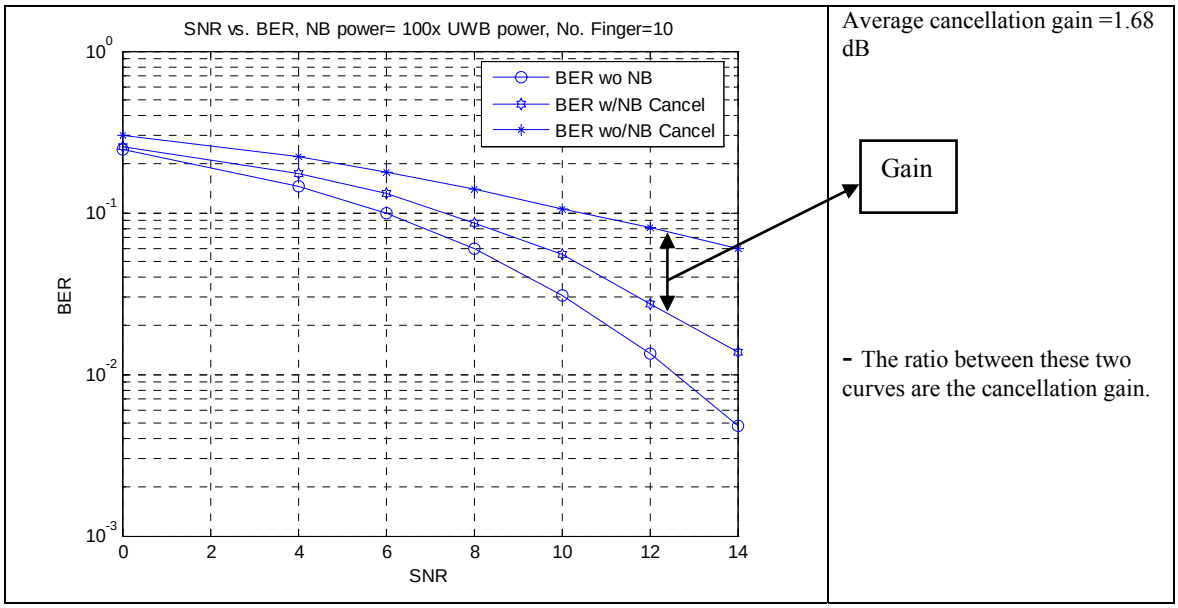

Figure 5-25. SNR vs. BER when NB power = 100 times UWB power, Number of Rake Fingers =10.

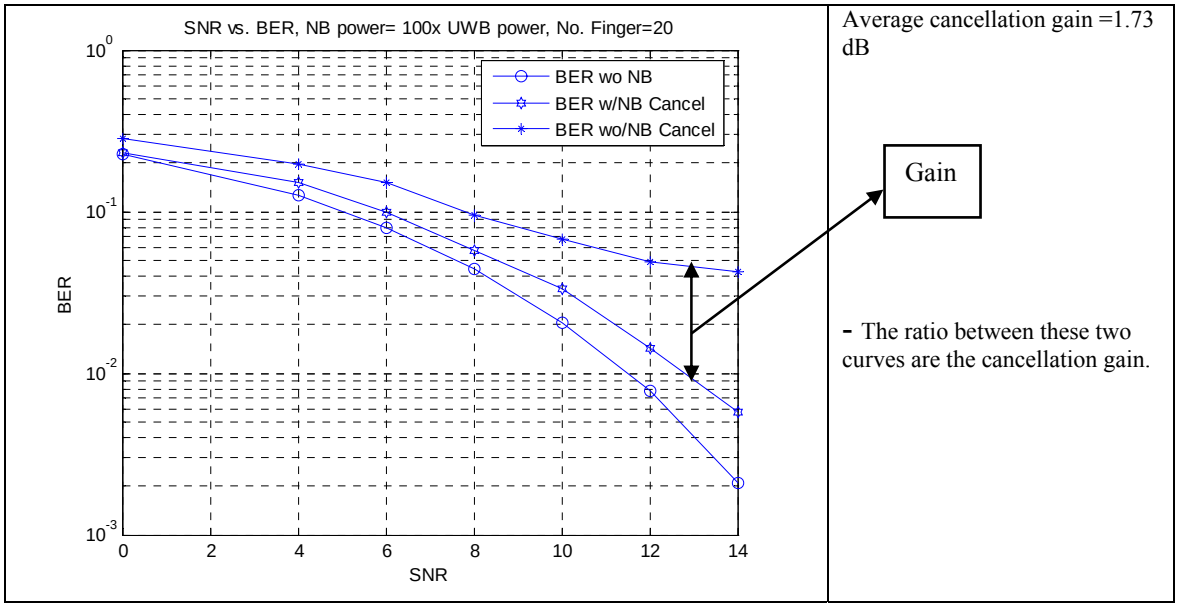

Figure 5-26. SNR vs. BER when NB power = 100 times UWB power, Number of Rake Fingers =20.

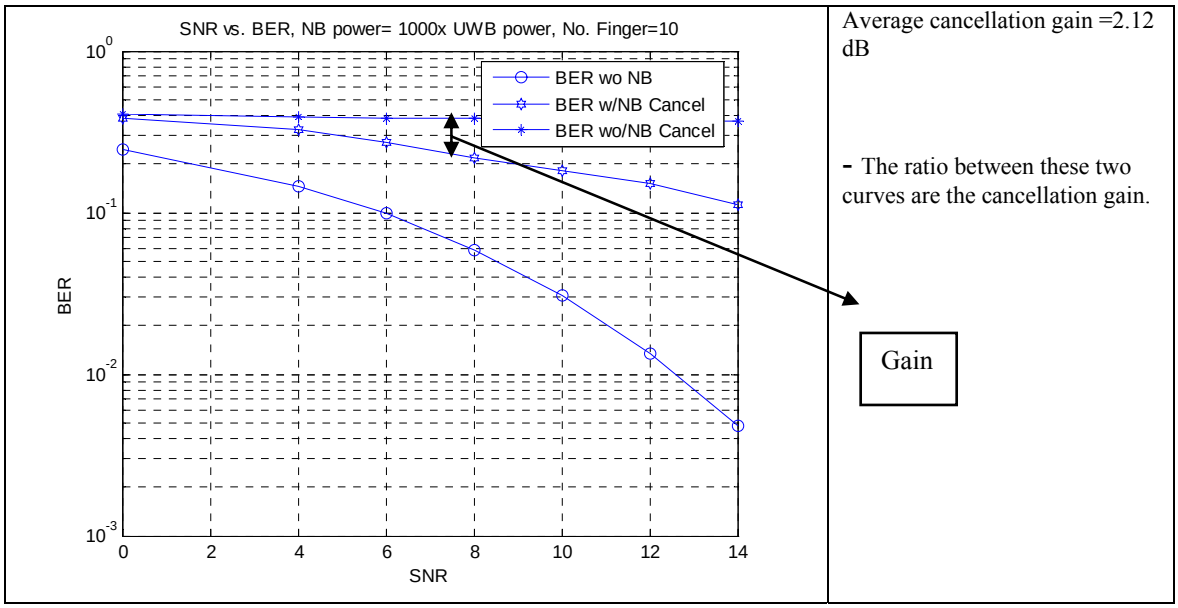

Figure 5-27. SNR vs. BER when NB power = 1000 times UWB power, Number of Rake Fingers =10.

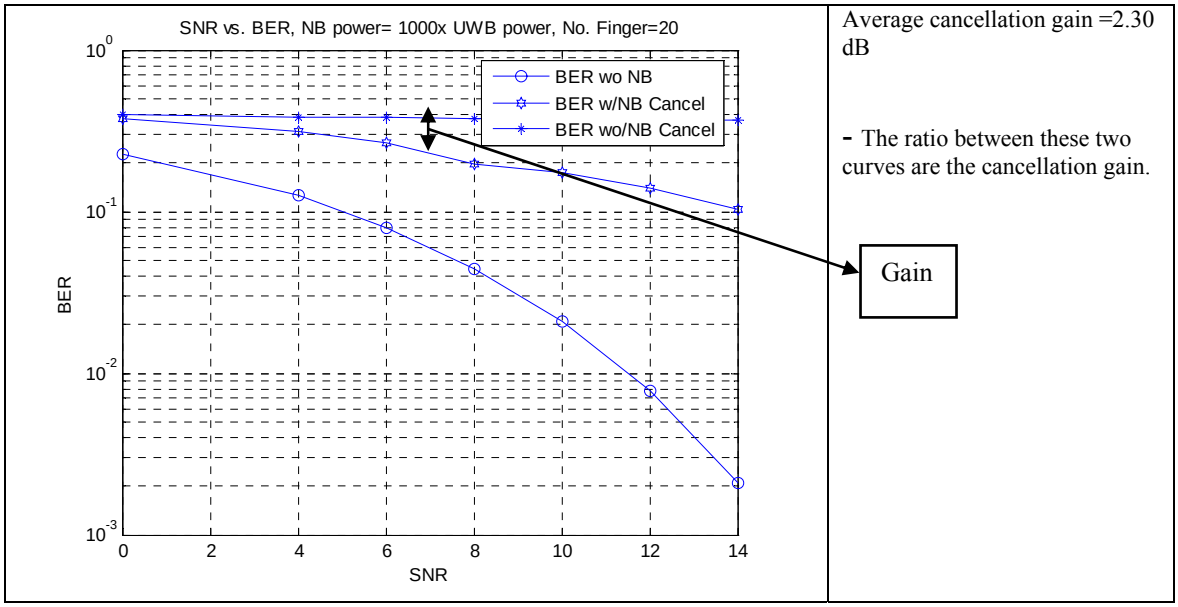

Figure 5-28. SNR vs. BER when NB power = 1000 times UWB power, Number of Rake Fingers =20.

For the same parameters setting, NB cancellation improves system performance for the same NB power strength as the number of receiver fingers increases (i.e., from 10 to 20). However, the performance decreases as more multipaths in the communication channel as seen in the results between CM2 and CM3. The NB cancellation performance is inversely proportional to the number of multipaths and proportional to the strength of the NB signal. The cancellation gain is a measure of the capacity of the cancellation circuit to notch out the NBI power from the UWB system. The cancellation gain is inversely proportional to the NB power. Table 5-3 (a,b) summarize NB cancellation performance.

Table 5-3a. Simulation results for channel type 2 (i.e., CM2)

NB / UWB power	Number of finger	Average cancellation gain (dB)
10	10	1.27
	20	1.06
100	10	2.08
	20	1.89
1000	10	3.85
	20	4.46

Table 5-3b. Simulation results for channel type 3 (i.e., CM3)

NB / UWB power	Number of finger	Average cancellation gain (dB)
10	10	0.94
	20	0.87
100	10	1.68
	20	1.73
1000	10	2.12
	20	2.30

The NBI cancellation circuit was implemented in the Altera DSP board, model EP1S80 and the cancellation results were displayed on the Tektronix oscilloscope, model TDS 210. The following sections consist of hardware implementation results and discussion of the results.

5.5.2.3 Hardware Set Up and Implementation Results

The results shown here only serve as a sanity check for the NBI cancellation implementation, not for the complete UWB transceiver. Figure 5-29 shows the hardware implementation. The NB and UWB signals were generated in the *Matlab/Simulink* platform and converted from decimal integer into hex string format. The converted signal was then saved in the system memory. The data stored in the memory were in turn fed into the NB canceller hardware based *Simulink* building block. The cancellation system was then programmed through a parallel port into the Altera FPGA device using *Signal Compiler* conversion tools.

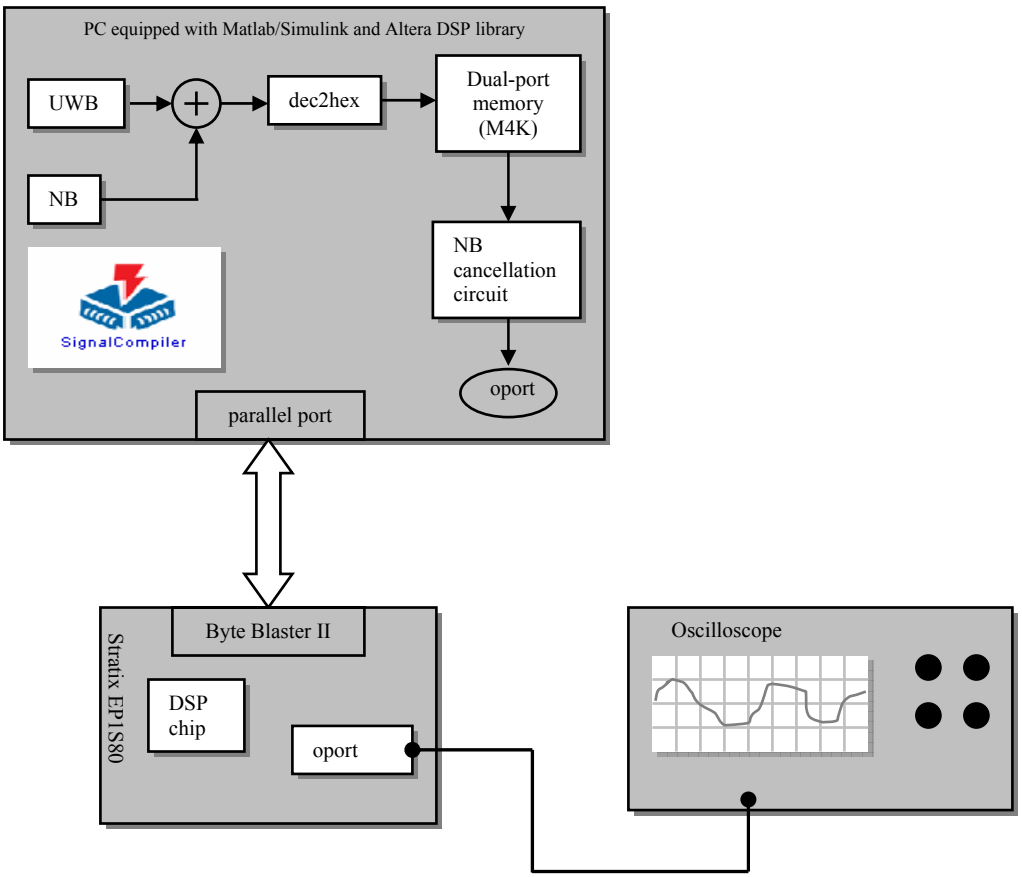

Figure 5-29. Hardware setup of FPGA implementation.

The setup for hardware implementation is quite different from the software simulation (i.e., run on Matlab platform). The processing data must be in hex string format instead of decimal integer using in software. The *dec2hex* converts decimal integers into a hex string. This block was fully customized using S-function. The converted data were stored in the memory of the system using the *dual-port memory (M4K)* from the Altera DSP library and were used as the input data for the NB cancellation circuit. The NB cancellation circuit performs NB cancellation. The process is described previously in section 4.2.

The *oport* is an output port from the Stratix II board, it send data through a serial cable to the display devices. In our case, the outputs were displayed on the oscilloscope.

The tool used to convert the Simulink block into hardware synthesizable code is the *Signal Compiler* from Altera FPGA development tool kit. Further details on *Signal Compiler* are available in section 4.4.2. The interface of Signal Compiler is shown in Figure 5-30.

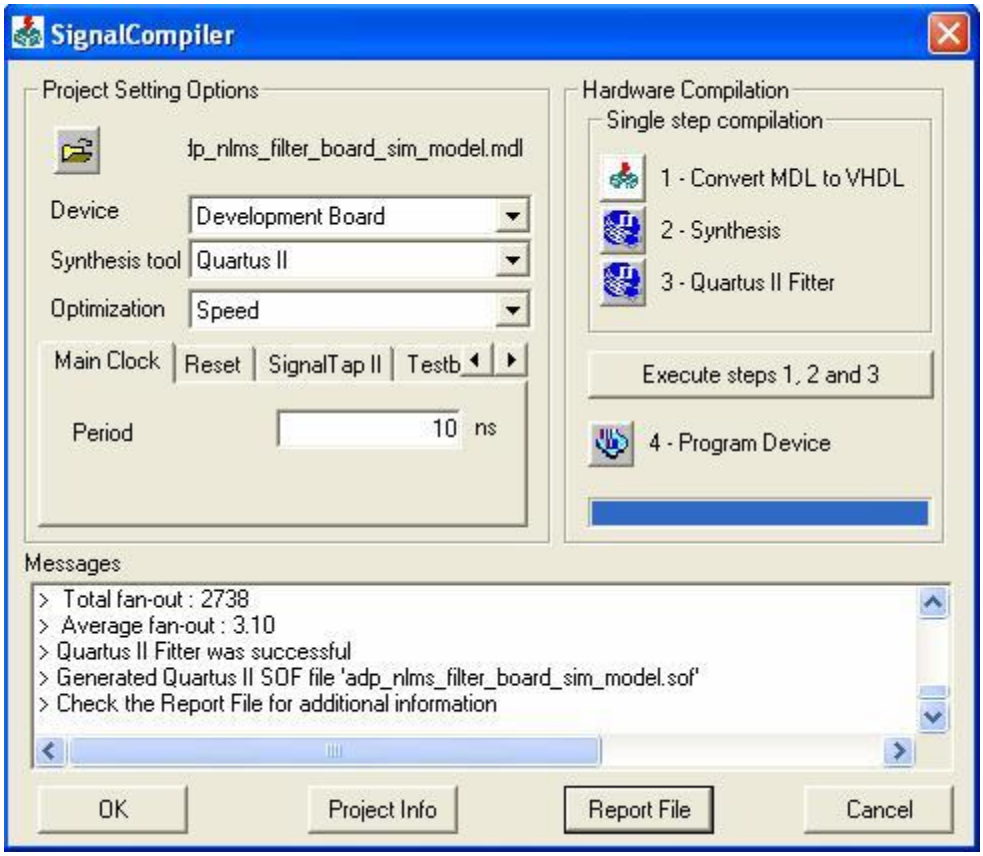

Figure 5-30. Signal Compiler interface.

The successfully compiled *Simulink* block was converted into hardware code using a conversion function available from the *Signal Compiler* shown as "1-Convert MDL to VHDL" in Figure 5-30. Table 5-4 summarizes the hardware resource of the implementation cancellation system.

Table 5-4. NB cancellation resource usage.

Resource	Usage
Total logic elements	976
- Combinational with no register	351
- Register only	40
- Combinational with a register	585
Logic element usage by number of LUT input	935
- 4 input functions	144
- 3 input functions	103
- 2 input functions	612
- 1 input functions	9
- Combinational cells for routing	67
Logic elements by mode	1114
- Normal mode	814
- Arithmetic mode	162
- Qfbk mode	0
- Register cascade mode	0
- Synchronous clear/load mode	54
- Asynchronous clear/load mode	84
Total registers	625
Total logic cells in carry chains	172
I/O pins	72
Total memory bits	880015
Total PLLs	1
Maximum fan-out mode	Clock
Maximum fan-out	883
Total fan-out	2738
Average fan-out	3.1
Worse-case tsu	4.21 ns
Worse-case tco	18.05 ns
Worse-case th	0.34 ns
Clock setup	9.64 ns

The inter-connection between the PC and FPGA board through parallel cable between the parallel port of the PC to the Byte Blaster II port of the FPGA development board. After the synthesizes process, the implemented cancellation system in *Matlab/Simulink* platform ready to program into the FPGA device. As mentioned in section 4.4, synthesizing process converts model descriptive language (MDL) into hardware synthesizable code (VHDL). The output from the *D/A* terminal on the FPGA

device was connected to the oscilloscope. Figure 5-31 shows the hardware implementation setup and the result is shown in Figure 5-32.

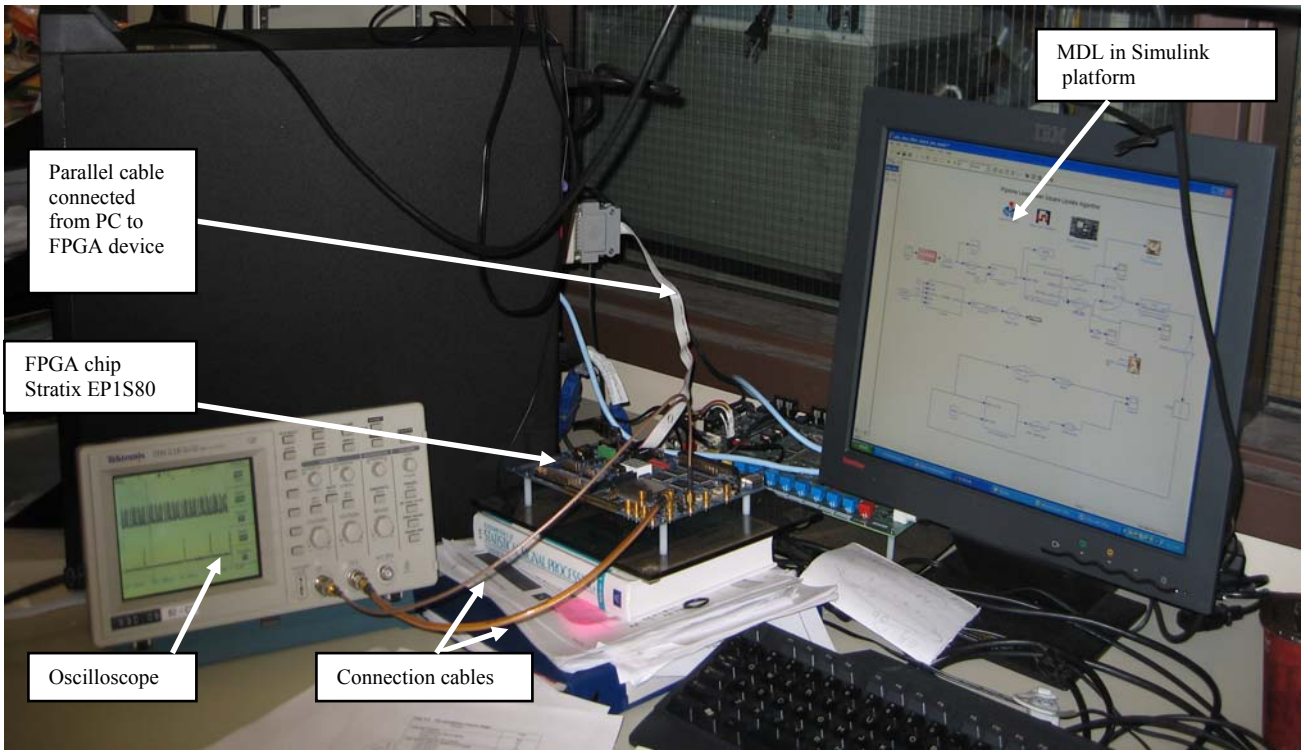

Figure 5-31. Hardware Setup.

Hardware performance of the NBI cancellation system was measured by comparing the transmitted UWB waveforms with the NB interfered UWB waveforms after passing through the NBI cancellation block. The results were collected on the oscilloscope as illustrated in Figure 5-32 to Figure 5-34. Figure 5-32 shows the UWB waveforms and the interfered UWB waveform from NB and AWGN signals. Figure 5-33 shows the UWB and the estimated UWB waveforms after notching out the power of the NB signal. The Figure 5-34 shows the delay measurement between the UWB and estimated UWB waveforms after cancelling out the NBI powers. The results were based on the NB power equal to 10 times of the UWB power. The speed of the DSP processor in the FPGA device was 103.7 MHz.

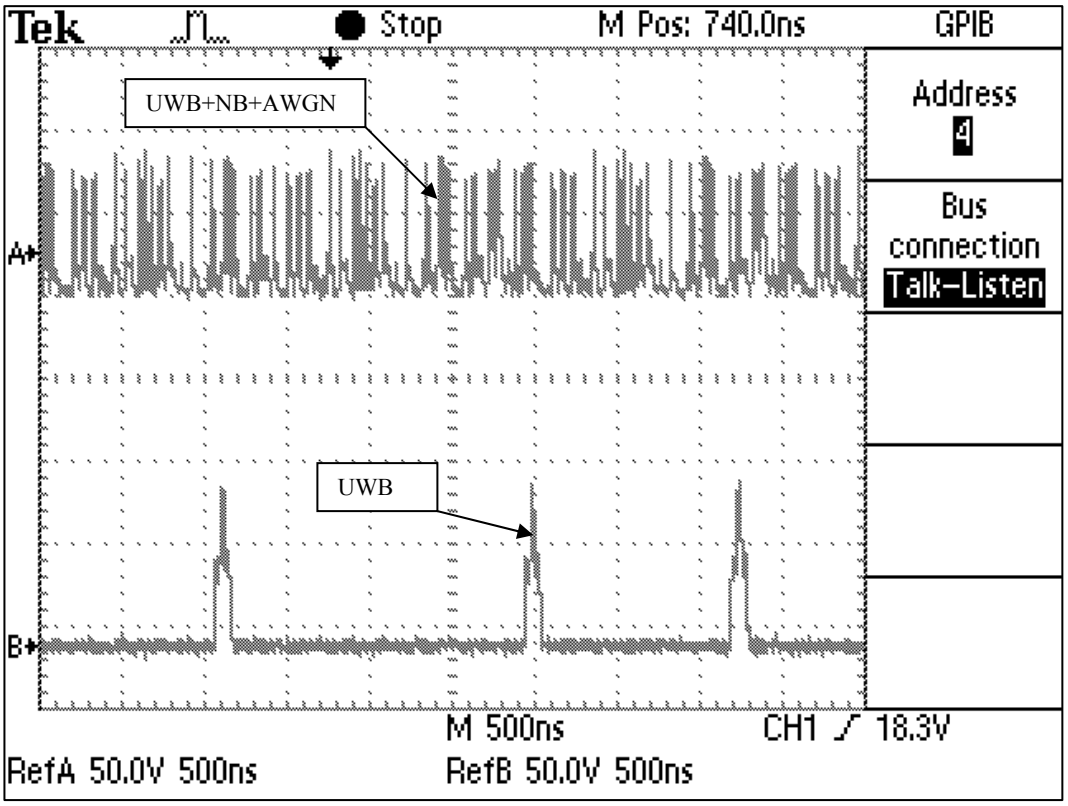

Figure 5-32. A) NB Interfered UWB Waveform, B) UWB Waveform.

Waveform A in Figure 5-32 represents the interfered UWB from NB and AWGN, waveform B represents UWB. The power strength of NB is equal to 10 times the UWB power. The UWB signal is totally buried in the NB as noise.

Waveforms A in Figure 5-33 represents the estimated UWB waveforms after passing through the NBI cancellation block. Waveforms B represents the UWB without NBI. From this figure, note that not only the delay is introduced into the estimated UWB waveforms, its shape is also deformed. The delay calculation is shown in Figure 5-34.

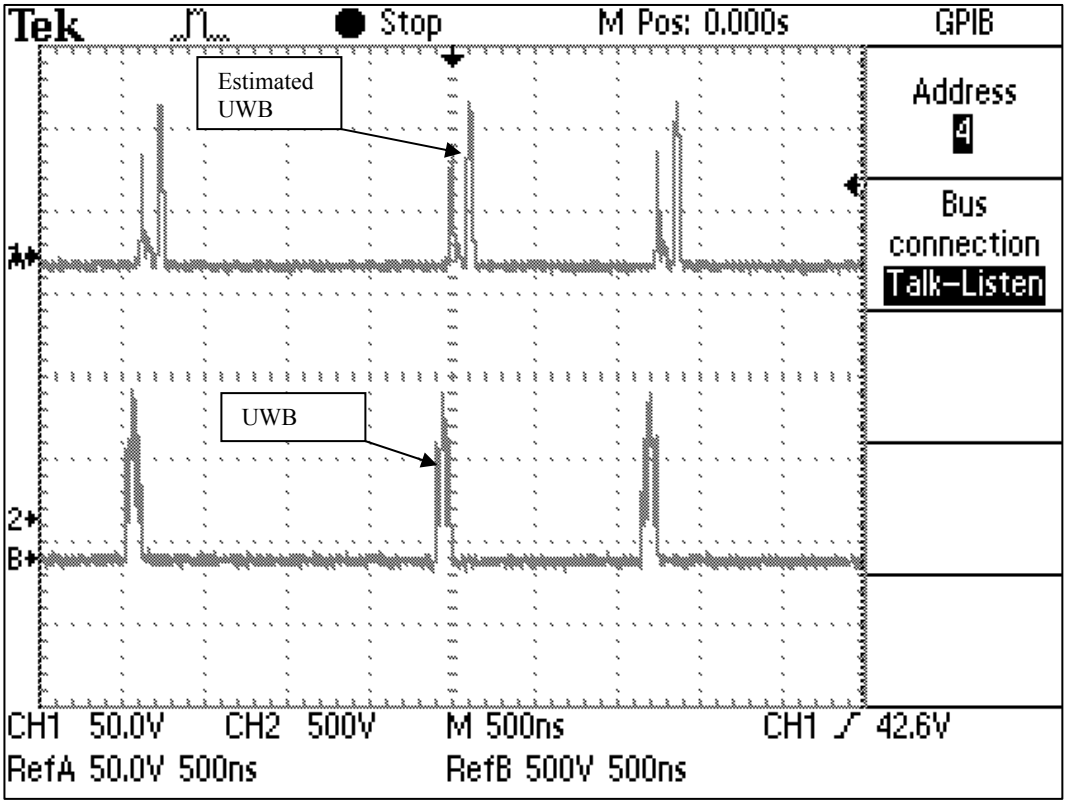

Figure 5-33. A) Estimated UWB Waveforms, B) UWB Waveforms.

The UWB waveforms leads the estimated UWB waveforms by 80 ns. The 80 ns delayed of the 9.64 ns clock setup time equivalent to 12 samples delay (i.e., $\frac{9.64}{80} * 100 = 12.05$) and the phase shift is approximate 7 degrees (i.e., $\frac{9.64}{80} * \frac{180}{\pi} \cong 7$). The delay in hardware implementation is consistent with the delay in *Matlab/Simulink* simulation however the phase shift difference is 3 degrees. The phase difference is due to the two different methods of measurement in software and hardware platforms. In the software, the measurement is taken between the transmitted UWB signal and the signal at the receiver through a large number of iterations. However, in hardware implementation, the one time measurement is taken between the transmitted UWB signal with the estimated NB signal. The reason to take a different approach

measurement in hardware is the impossibility of the iteration setup. The delays and phase shift were set as the value of delay and phase offset parameters indicated in Figure 4-1.

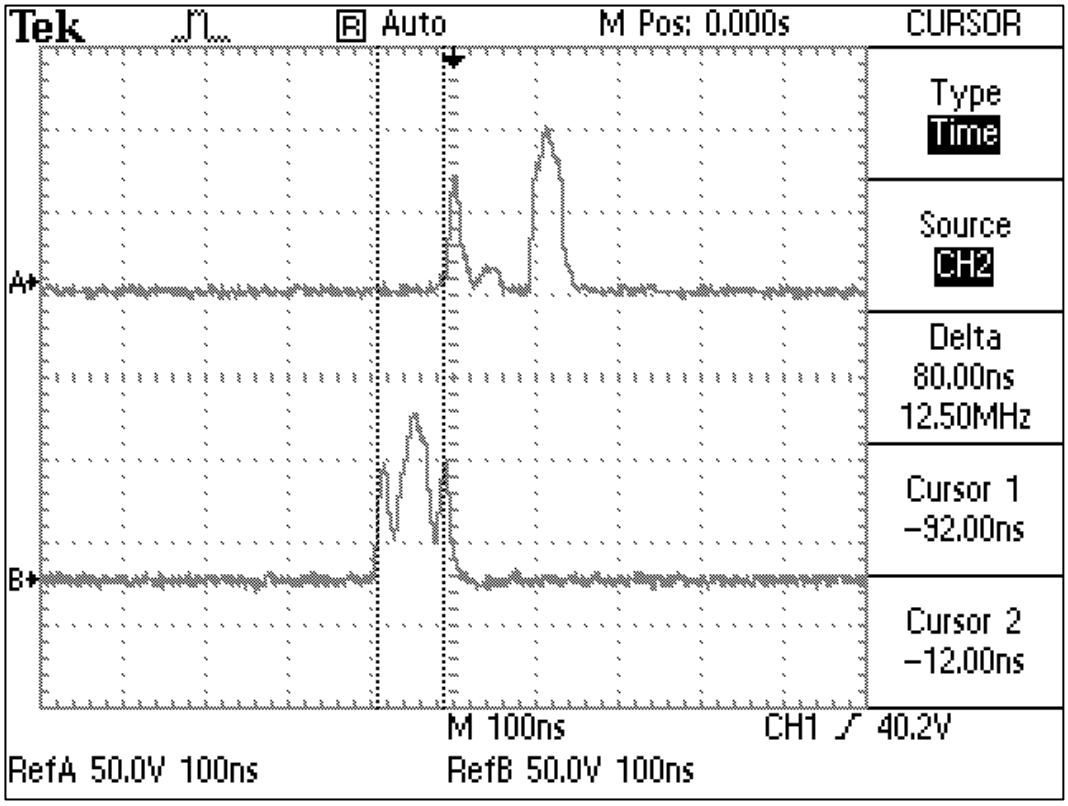

Figure 5-34. A) Estimated UWB Waveforms, B) UWB Waveforms.

The estimated UWB waveforms are not severely distorted when the NB power is 10 times higher than the UWB power. Note that the transmitted UWB signal applies the TH-PP modulation technique in which the waveform is shifted to the right by ε if a "1" is transmitted otherwise a waveform is shifted to the left by ε. However, the estimated UWB waveform deformed its shape as seen from waveform A. This deformation might cause an error in term of making decision whether the transmitted bit is a "1" or "0" at the receiver.

The overall performance of hardware implementation is consistent with the results collected from *Matlab/Simulink* simulation. The hardware simulation results proved the correctness of the NBI cancellation block.

5.6 Summary

This chapter describes how the simulation model is constructed and applied software Matlab/Simulink simulation as well as the Altera FPGA hardware implementation. Series of software simulation results were collected from frequency estimation techniques and from the narrowband (NB) cancellation performances. In addition, the results also show successful hardware implementation of the NB cancellation.

The frequency estimation performance was measured by its mean and variance value compared to the true value which is 5.2 GHz. The method of moment has shown its out performance when the sampling rate is equal to 4 times the carrier frequency (i.e., f_s=20 GHz). In contrast, the method of maximum likelihood estimation improves its performance when the sampling rate increases. In this case, the choice of sampling rate is 6 times the carrier frequency (i.e., f_s=30 GHz). In addition, more samples are taken into the evaluation improve performance of the MLE process. The better choice for the frequency estimation is the MLE with a sampling rate equals to 6 times the carrier frequency and evaluated with 128 samples.

The NB cancellation performance was measured by bit error rate and average cancellation gain. Simulations results show the mitigation performance decreases noticeably as the power strength of the NB increases and more multi-paths are in the

communication channel (i.e., from CM2 to CM3). On the other hand, the mitigation performance slightly decreases with the number of fingers of the Rake receiver. The better choice is the 10 fingers Rake receiver.

The hardware implementation results are consistent with the results collected from *Matlab/Simulink* simulation results. The consistency of the two results validates the NBI cancellation block design.

Chapter 6 Conclusions and Future Work

6.1 Summary

Chapter 1 presents general background in UWB including UWB modulation and the FCC regulations. The chapter starts with introduction and history of the UWB technology. Following the introduction, the key characteristics that often apply to the UWB systems including modulation technique, bandwidth and mapping waveform are covered. In the last section, the impact of NB onto the UWB systems is studied. It is shown that the impact is more profound when the two central frequencies are close to each other. There is no unique technique to combat NB interference, the method of choice mainly depends on the available resources and the desired system performance.

Chapter 2 describes the NB and UWB signals. The property of each signal is carefully analyzed and studied. First, the investigation of UWB system includes the derivation of the signal in term of mathematical representation modeling the signal in *Matlab/Simulink* platform. Time-hopping technique in conjunction with pulse position modulating significantly reduces ISI. The TH-PPM-UWB ultilizes a bandwidth equal to 3.7 GHz and a center frequency at 4 GHz. An orthogonal frequency division multiplexing technique is used in this study as a NB signal. This NB interferer is the IEEE 802.11a indoor wireless local area network having a bandwidth of 17 MHz centered at 5.2 GHz.

Chapter 3 focuses on the statistical properties of the NB and UWB signals. The statistical derivations are mainly based on the receiving signal consisting of NB, UWB and additive white Gaussian noise (AWGN) signals. Each signal was carefully examined and analyzed. The studies show these three signals are independent to each other and easily to identify. This makes the task of detecting the NB signal from the received UWB signal much simpler. The detection of the NB is the comparison of the average power of the receiving signal with the maximum power at the NB central frequency (i.e., 5.2 GHz). If the maximum power higher than the average power then the NB is successfully detected. NB detection is always successful when the power of the NB is more than 5 times of the UWB level.

Chapter 4 proposes a NB interference cancellation scheme and presents two techniques to estimate the NB frequency: the method of moment and the method of maximum likelihood. A NB cancellation circuit topology is introduced. The circuit consists of signal up/down converters, low pass filter (LPF) and multi-tap least mean square (LMS) update algorithm. The circuit is implemented in the form of Model Descriptive Language (MDL) provided by Altera. The MDL model can be easily converted into a synthesizable code. The code is used to program a FPGA device (i.e., the Altera Stratix Family EP1S80 in this study). The *Signal Compiler* of Altera DSP development tool is used to convert *Simulink* model into a synthesizable code. The LMS update algorithm is implemented using the pipelining technique which the intention of reducing the delay or latency in the feedback path. The pipelined LMS is constructed using the coefficient classification technique. The technique classifies the odd and even coefficients and assembles these coefficients in a tree structure. A set of parameters are simulated to find the optimum values for simulations. It is found that the filter length

N =64 and the convergence factor μ =0.03125 are the optimum parameters. The chapter also covers two techniques to estimate the NB frequency. In the method moment, the frequency is calculated by evaluating the inverse cosine function of the autocorrelation over the power of the receiving signals. The method of maximum likelihood estimates the NB central frequency by maximizing the argument of the exponent in the probability density function (PDF).

Chapter 5 verifies the NBI detection and cancellation by obtaining a series of results from Matlab/Simulink simulations and FPGA hardware implementation. Simulation results on frequency estimation indicate the method of maximum likelihood yield better performance than the method of moment. The last section presents the results of notching the narrowband power from the ultra-wideband signal. Due to the lengthy simulation time, the results were given for two typical channel models, CM2 and CM3. The narrowband power varied from 10, 100 and 1000 times of the UWB signal. The results indicates cancellation gain increases as the power of the NB increases for both CM2 and CM3. The results signify cancellation is not highly depending on channel models but mostly relying upon the cancellation method. The hardware implementation results are consistent with the results obtained from Matlab/Simulink simulations. The consistency between the two results proves and validates the design of the NBI detection and cancellation.

6.1. Conclusion

The thesis presents the design and analysis of two relevant ultra-wideband topics namely narrowband interference detection and cancellation. The spectrogram technique was used to detect NBI. The spectrogram technique involves evaluating the power at the

NB central frequency from the received UWB signal. The power calculation is accomplished by determining the variance and the mean of the received UWB signal and applied these parameters into the chi-squared distribution. The NB detection results obtained from comparing the spectrogram value against the average power of the received UWB signal. The NB detection studies show that the detection fails when the NB power is less than the UWB power and has equal chance to detect the NB when the two powers are equal. A detection is always successful when the NB power is 5 times larger than the UWB power. The NB detection results, therefore, depends on the amount of NB power contributed or added into the UWB systems.

Besides the NB detection proposed in this thesis, a NBI cancellation circuit is also proposed. The circuit eliminates NB power contributed in the UWB systems. The proposed structure was implemented in an FPGA device of the Altera high-speed DSP development board, model EP1S80. The cancellation circuit involves estimating the NB central frequency, down and up converting the received UWB signal into the base and upper band, both NB central frequency estimation and signal base conversion are performed in analog domain. However, the NB estimation is processed in digital domain using the least mean square adaptive filter technique.

The results from both Matlab/Simulink and Altera FPGA device for NBI cancellation circuit experience 12-sample delay. The delay is mainly caused by the adaptive process. There is about 3 degrees phase shift difference between the Matlab/Simulink simulation and FPGA implementation results. The cause is due to the different method of measurements. In the Matlab/Simulink simulation, the phase shift is measured by injecting an array of phase shifts and the phase shift chosen corresponding the lowest BER. The phase shift measurement in the FPGA implementation is the

measurement of the phase difference between the transmitted UWB and the estimated NB signals. Nevertheless, as long as the delay and phase offset can be found, the alignment of the received UWB signal and the estimated NB signal are achieved.

The results collected from Matlab/Simulink simulation show the average NB cancellation gain increases with the level of NB power contributed to the UWB signal. The average NB cancellation gain indicates how well the NBI cancellation circuit performs. The gain shows the benefit the UWB systems achieve from the NBI canceller circuit for various levels of NB power. The UWB system obtains up to 5 dB gain for CM2 and up to 3 dB gain for CM3 when the NBI power is 1000 times higher than UWB power. These two results signify the performance of the NBI cancellation circuit is independent with the communication channel. The improvement in term of NB cancellation gain implies the NBI cancellation circuit is a solution to solve indoor NB interference in the UWB system.

The NBI cancellation circuit performance further investigated in the hardware platform by collecting the results on the oscilloscope from a FPGA device implementation. Results of the NB elimination in hardware implementation are similar to the *Matlab/Simulink* simulation results. Agreement between the two results implies the NBI cancellation circuit is correctly designed and implemented.

The following suggestions can be used to extend this work to implement the whole system in hardware or to improve the proposed solution for multiple-interference detection and cancellation.

6.2. Suggestion for Further Research

In this thesis, the NB detection and cancellation was studied for the indoor UWB communication systems with only one interferer. It would be interesting and useful to extend this NB detection and cancellation scheme for multiple interferences.

In terms of hardware implementation, a complete system should be implemented on the FPGA board by building the UWB transmitter/receiver, OFDM signal generator and NB detector in Simulink using hardware synthesizable code. The system can be implemented on either *Altera Stratix family EP1S80* or *Xilinx Virtex 4* or higher.

The UWB system in this thesis work is assumed to be in perfect synchronization and accurate signal acquisition with the second order Gaussian mapping waveform. Future works can be extended to the non-ideal synchronization, signal acquisition with higher order of Gaussian mapping waveforms.

References

[1] FCC, First Report and Order, FCC-02-48, "Revision of Part 15 of the Commission's rules Regarding Ultra-Wideband Transmission Systems," Federal Communication Commission, adopted February 14, 2002.

[2] Maria-Gabriella Di Benedetto, Guerino Giancola, *Understanding Ultra WideBand Radio Fundamentals*, New Jersey, United State, Prentice Hall, 2004, Chapter 1.

[3] Defense Advanced Research Projects Agency, Office of the Secretary of Defense, "Assessment of Ultra-Wideband (UWB) Technology," Report R-6280, prepared by OSD/DARPA UWB Radar Review Panel, July 1990.

[4] "European regulatory information" available at http://www.eu-projects.com/ultrawaves/doc/W09-04-0031-R03.pdf.

[5] J.D. Choi and W.E. Stark, "Performance analysis of ultra-wideband spreading spectrum communications in narrowband interference," *Proc. IEEE MILCOM'02*, vol. 2, pp. 1075-1080, October 2002.

[6] Li Zhao, Alexander M. Haimovich and Haim Grebel, "Performance of UWB communications in the presence of interference," *IEEE Journal on Selected Areas in Communication*, vol. 20, issue 9, pp. 1684-1691, December 2002.

[7] Matti Hamalaimen, Raffaello Tesi, and Jari Iinatti, "UWB Co-Existence with IEEE802.11a and UTMS in Modified Saleh-Valenzuela Channel," available at *http://www.ee.oulu.fi/~mattih/IWUWBS2004_ID034.pdf*.

[8] Maria Stella Iacobucci, Maria-Gabriella di Benedetto, and Luca De Nardis, "Radio frequency interference issues in impulse radio: multiple access communication systems," *Proc. IEEE UWBST'02 on Ultra Wideband Systems and Technologies*, pp. 293-296, May 2002.

[9] A. Taha and K.M. Chugg, "A theoretical study on the effects of interference on UWB multiple access impulse radio," *Proc. IEEE ACSSC'02 on Signals, Systems and Computers,* vol. 1, pp. 728-732, November 2002.

[10] W. Tao, W. Yong, and C. Kangsheng, "Analyzing the interference power of narrowband jamming signal on UWB systems," *Proc. IEEE PIMRC'03 on Personal, Indoor and Mobile Radio Communications,* vol. 1, pp. 612-15, September 2003.

[11] Liuqing Yang and Georgios B. Giannakis, "Unification of ultra-wideband multiple access schemes and comparison in the presence of interference," *Proc. IEEE ACSSC'03 on Signals, Systems and Computers*, vol. 2, pp. 1239-1243, November 2003.

[12] Jeffrey R. Foerster, "The performance of a DS spread UWB system in the presence of multipath, narrowband interference, and multiuser interference," *Proc. IEEE UWBST'02 on Ultra Wibeband Systems and Technologies*, pp. 87-91, May 2002.

[13] I. Bergel, E. Fishler, and H. Messer, "Narrow-band interference suppression in time-hopping impulse-radio systems," *Proc. IEEE UWBST'02 Ultra Wideband Systems and Technologies,* pp. 303-307, May 2002.

[14] Qinghua Li and Leslie A. Rusch, "Multiuser detection for DS-CDMA UWB in the home environment," *IEEE Journal on Sel. Areas in Communications*, vol. 20, issue 9, pp. 1701-11, December 2002.

[15] N. Boubaker and K.B. Letaief, "A low complexity MMSE-RAKE receiver in a realistic UWB channel and in the presence of NBI," *Proc. IEEE WCNC'03 on Wireless Communications and Networking,* vol. 1, pp.233-237, March 2003.

[16] A.R. Forouzan, M. Nasiri-Kenari and J.A. Salehi, "Performance analysis of time-hopping spread-spectrum multiple access systems: uncoded and coded scheme," *IEEE Trans. On Wireless Communications*, vol.1, issue 4, pp. 671-681, October 2002.

[17] B.M. Sadler and A. Swami, "On the Performance of Episodic UWB and Direct-Sequence Communication Systems," IEEE *Trans. On Wireless Communications*, vol. 3, issue 6, pp. 2246-2255, November 2004.

[18] Multiple Access Communication Ltd, "An investigation into the impact of ultra-wideband transmission systems," RA0699/TDOC/99/02, Report to the Radio Communications Agency, UK, February 2000.

[19] A. Swami, B. Sadler, and J. Turner, "On the coexistence of ultra-wideband and narrowband radio systems," *Proc. IEEE-MILCOM'01 on Military Communications Conference,* vol. 1, pp. 16-19, October 2001.

[20] M. Mittelbach, et al. , " Study of Coexistence Between UWB and NB Cellular Systems," *Proc. IEEE UWBST'04 on Ultra Wideband Systems and Technologies*, pp. 40-44, May 2004.

[21] T. Ikegami and K. Ohno, "Interference mitigation study for UWB impulse radio," *Proc. IEEE PIMRC'03*, vol. 1, pp. 583-587, September 2003.

[22] John Wang, "Narrowband Interference Suppression in Time Hopping Impulse Radio," *Proc. IEEE VETECF'04 on Ultra Wideband Systems and Technologies*, vol. 3, pp. 2138-2142, September 2004.

[23] Diakoumis Gerakoulis, and Paola Salmi, " An Interference Suppressing OFDM System for Ultra Wide Bandwidth Radio Channels," *Proc. IEEE UWBST'02 on Ultra Wideband Systems and Technologies*, pp. 259-264, May 2002.

[24] Reza Pasand, John Nielsen, and Abu Sesay, "UWB Receiver Based On Filter Bank Architecture For Suppression Of Narrowband Interference Noise," *Proc. IEEE MILCOM'04 on Military Communications Conference*, vol. 2, pp. 579-585, November 2004.

[25] David R. McKinstry and R. Michael Buehrer, "LMS Analog and Digital Narrowband Rejection System for UWB Communications," *Proc. IEEE UWBST'03 on Ultra Wideband Systems and Technologies*, pp. 91-95, November 2003.

[26] Odling, P. et al., "An Approach to Analog Mitigation of RFI," *Proc. IEEE JSAC'02 on Selected Areas in Communications*, vol. 20, issue 5, pp. 974-986, June 2002.

[27] M. Ghavami, L. B. Michael, R. Kohno*, Ultra Wideband Signals and Systems in Communication Engineering,* West Sussex, England, John Wiley & Sons Ltd, May 2004, Chapter 5.

[28] Maria-Gabriella Di Benedetto, Guerino Giancola, *Understanding Ultra WideBand Radio Fundamentals*, New Jersey, United State, Prentice Hall, 2004, Chapter 2.

[29] Rowe, H. E., *Signal and Noise in Communication Systems*, Princeton, New Jersey: D. Van Nostrand Company, Inc, 1965.

[30] Lehmann, N. H., and A.M. Haimovich, "The Power Spectral Density of a Time Hopping UWB Signal: A Survey," *Proc. IEEE UWBST's 03 on Ultra Wideband Systems and Technologies*, pp. 234-239, November 2003.

[31] Padgett, J. E., "The Power Spectral Density of a UWB Signal with Pulse Repetition Frequency (PRF) Modulation," *Proc. IEEE UWBST'03 on Ultra Wideband Systems and Technologies,* pp. 15-20, November 2003.

[32] Win, M. Z., "A Unified Analysis of Generalized Time-Hopping Spread-Spectrum Signals in the Presence of Timing Jitter," *IEEE Journal on Sel. Areas in Communications*, vol. 20, issue 9, pp. 1664-1676, December 2002.

[33] Maria-Gabriella Di Benedetto, Guerino Giancola, *Understanding Ultra WideBand Radio Fundamentals*, New Jersey, United State, Prentice Hall, 2004, Chapter 3.

[34] Rowe, H. E., *Signal and Noise in Communication Systems*, Princeton, New Jersey: D. Van Nostrand Company, Inc, 1965.

[35] Win, M. Z., "A Unified Analysis of Generalized Time-Hopping Spread-Spectrum Signals in the Presence of Timing Jitter," *IEEE Journal on Sel. Areas in Communication*, vol. 20, issue 9, pp. 1664-1676, December 2002.

[36] Marc Engels, *Wireless OFDM systems: how to make them work?*, Kluwer Academic Publishers, Boston 2002, Chapter 4.

[37] Weinstein, S.B., and P.M. Ebert, "Data transmission by frequency-division multiplexing using the discrete Fourier transform," IEEE *Trans. Wireless Communications*, vol. 19, issue 5, pp. 628-634, October 1971.

[38] Marc Engels, *Wireless OFDM Systems, How To Make Them Work?*, Norwell, Massachusetts, USA: Kluwer Academic Publishers, 2002, Chapter 3.

[39] Van Nee, R., and R. Prasad, *OFDM for Wireless Multimedia Communications*, Norwood, Massachusetts, USA; Arthec House Publishers, 2000.

[40] J. D Choi and W. E. Stark, "Performance analysis of ultra-wideband spread-spectrum communications in narrowband interference," *Proc. IEEE MILCOM'02 on Selected Areas in Communications*, vol. 2, pp. 1075-1080, October 2002.

[41] Jeffrey. H. Reed, et al., *An Introduction to Ultra Wideband Communication Systems*, New Jersey, United State, Peasrson Education, March 2005, Chapter 7.

[42] Steven M. Kay, *Fundamentals of Statistical Signal Processing Volume II: Detection Theory*. New Jersey; Prentice Hall, 1993, Chapter 7.

[43] P. Beckman, *A History of π (PI)*, New York; Barnes and Noble, 1993.

[44] Atheros Communications Inc., "*Worldwide Regulatory Progress for Wireless LANs*",

http://www.atheros.com/pt/whitepapers/Atheros_Regulatory_whitepaper.pdf

[45] David R. McKinstry, "Ultra-Wideband Small Scale Channel Modeling and its Application to Receiver Design," Master's Thesis, Dept. of Electrical and Computer Engineering, Virginia Tech, Blacksburg, VA, 2003.

[46] Widrow, B., "Thinking about thinking: the discovery of the LMS algorithm," *Proc. IEEE MSP'05 on Signal Processing Magagize*, vol. 22 issue 1, pp. 100-106, January 2005.

[47] Simon Haykin, *Adaptive Filter Theory*. New Jersey, Prentice Hall, 4th Edition, 2002, Chapter 5.

[48] Paulo S. R. Diniz, *Adaptive Filtering: Algorithms and Practical Implementation*. Norwell, Massachusetts, Kluwer Academic Publishers, 2nd Edition, 2002, Chapter 4.

[49] Altera Devices Specification available at:

http://www.altera.com/products/devices/stratix2gx/features/s2gx-features.html

[50] Altera white paper available at

http://www.altera.com/literature/wp/wp_dsp_comp.pdf

[51] J. Rose and A. Sangiovanni-Vincentelli, "Architecture of field programmable gate arrays," *Proc. IEEE on Solid-State Circuits*, vol. 81, issue 7, pp. 1013-109, 1993.

[52] K.K. Parhi and D.G. Messerschmitt, "Pipeline interleaving and parallelism in recursive digital filters – part I: pipelining using scattered look-ahead and decomposition," *Proc. IEEE ASSP'89 on Acoustics, Speech, and Signal Processing*, vol. 37, pp. 1099-1117, September 1989.

[53] G. Long, F. Ling, and J.G. Proakis, "The LMS algorithm with delayed coefficient adaptation," *Proc. IEEE ASSP'89 on Acoustics, Speech, and Signal Processing*, vol. 37, pp. 1397-1405, September 1989.

[54] J. Okello, et al., "A new architecture for implementing pipelined FIR ADF based on classification of coefficients," *Proc. IEEE CAS:II'02 on Circuits and Systems II: Analog and Digital Signal Processing*, vol. 49, issue 6, pp. 418-426, June 2002.

[55] G-H. Im and N.R. Shanbhag, "A pipelined adaptive NEXT canceller," *Proc. IEEE SP'98 on Signal Processing*, vol. 39, issue 8, pp. 2252-2258, August 1998.

[56] N.R. Shanbhag and K.K. Parhi, "Relaxed look-ahead pipelined LMS adaptive filters and their application to ADPCM code," *Proc. IEEE OCS-II'93 on Circuits and Systems II: Analog and Digital Signal Processing,* vol. 40, issue 12, pp. 753-766, December 1993.

[57] William H. Tranter. Et all., *Principle of Communication Systems Simulation with Wireless Applications*, New Jersey, United State, Prentice Hall, 2004, Chapter 10.

[58] Steven M. Kay, *Fundamentals of Statistical Signal Processing Volume II: Estimation Theory*, New Jersey; Prentice Hall, 1993, Chapter 4.

[59] Ghassemzadeh, S.S., and V. Tarokh, "UWB Path Loss Characterization In Residential Environments," *IEEE RFICS'03*, pp. 501-504, June 2003.

[60] Pendergrass, M., and W.C. Beeler, *Empirically Based Statistical Ultra-Wideband Channel Model*, Available at http://grouper.ieee.org/groups/802/15/pub/2002/Jul02/02240r0P802-15_SG3a-Empirically_Based_UWB_Channel_Model.ppt, July 2002.

[61] Foerster, J., and Q. Li, *UWB Channel Modeling Contribution from Intel*, available at http://grouper.ieee.org/groups/802/15/pub/2002/Jul02/02279r0P802-15_SG3a-Channel-Model-Cont-Intel.doc, June 2002.

[62] Howinen, V., M. Hamalainen, R. Tesi, L. Hentila, N.Laine, D. Porcino, and G. Shor, *A proposal for a selection of indoor UWB path loss model*, Available at: http://grouper.ieee.org/groups/802/15/pub/2002/Mar02/02119r0P802-15_SG3a-Response-to-CFA-ULTRAWAVES.ppt, June 2002.

[63] Kunisch, J., and J. Pamp, *Radio Channel Model for Indoor UWB WPAN Environments,* Available at: http://grouper.ieee.org/groups/802/15/pub/2002/Jul02/02281r0P802-15_SG3a-IMST-Response-Call-Contributions-UWB-Channel-Models.pdf, July 2002.

[64] Ghassemzadeh, S.S., and V. Tarokh, *The Ultra-wideband Indoor Path Loss model,* Available at: http://grouper.ieee.org/groups/802/15/pub/2002/Jul02/02277r1P802-15_SG3a-802.15-UWB-Propagation-Path%20Loss-Model.doc, July 2002.

[65] Molisch, A.F., M.Z. Win, and D. Cassioli, *The Ultra-Wide Bandwidth Indoor Channel: from Statistical Model to Simulations.* Available at: http://grouper.ieee.org/groups/802/15/pub/2002/Jul02/02284r0P802-15_SG3a-The-Ultra-Wide-Bandwidth-Indoor-Channel-from-Statistical-Model-to-Simulations.pdf, July 2002.

[66] Cramer, R.J-M., R.A. Scholtz, and M.Z. Win, *Evaluation of an Indoor Ultra-Wideband Propagation Channel,* Available at: http://grouper.ieee.org/groups/802/15/pub/2002/Jul02/02286r0P802-15_SG3a-Evaluation-of-an-Indoor-Ultra-Wideband-Propagation-Channel.doc, July 2002.

[67] Siwiak, K., and A. Petroff, "A Path Link Model for Ultra Wide Band Pulse Transmissions," *IEEE Conference on Vehicular Technology,* vol. 2, pp. 1173-1175, 2002.

[68] Turin, G.L., F.D. Clapp, T.L. Johnston, S.B. Fine, and D. Lavry, "A Statistical Model of Urban Multipath Propagation," *IEEE Transactions Vehicular Technology,* vol. 21, pp. 1-9, February 1972.

[69] Saleh, A.A.M., and R.A. Valenzuela, "A Statistical Model for Indoor Multipath Propagation," *IEEE Journal on Selected Areas in Communications,* vol. 5, issue 2 pp. 128-137, February 1987.

[70] Win, M.Z., and R.A. Scholtz, "On the Robustness of Ultra-Wide Bandwidth Signals in Dense Multipath Environments," *IEEE Communication Letters,* vol. 2, issue 2, pp. 51-53, February 1998.

[71] Price, R., and P.E. Green Jr., "A communication technique for multi-path channels," *Proc. IRE,* vol. 46, pp. 555-570, March 1958.

[72] Win, M.Z., and R.A. Scholtz, “On the Energy Capture of Ultrawide Bandwidth Wireless Indoor Channels: A Communication-Theoretic View, “ *IEEE Journal on Selected Areas in Communications,* vol. 2, issue 9 pp. 245-247, September 1998.

[73] Cassioli, D., M.Z. Win, F. Vatalaro, and A.F. Molisch, ”Performance of Low-Complexity Rake Reception in a Realistic UWB Channel,” *IEEE International Conference on Communications,* vol. 2, pp. 763-767, April 2002.

Appendix A

The UWB Channel Models Proposed by the IEEE802.15.3a

In July 2003, the Channel-Modeling sub-committee of study group IEEE 802.15.SG3a published the final report regarding the UWB indoor multi-path channel model. This model should be used for evaluating the performance of different physical layers as submitted to the IEEE 802.15.3 task group. Different contributions were considered for developing the proposed model: a) the statistical path loss model for indoor UWB signals presented by [59]; b) channel measurements and modeling described by [60]; c) the Intel proposal [61]; d) the results of the measurement campaign performed at Oulu University by [62]; e) the radio channel model proposed by [63] after a channel sounding campaign in an office environment; f) the statistical path loss model proposed by [64] after the analysis of over 300000 frequency responses at 712 locations and 23 homes; g) the channel model submitted by Mitsubishi after a measurement campaign in an office building [65]; h) the analysis on the UWB propagation channel performed by [66] by applying the clean algorithm; i) and the studies by [67].

The IEEE channel-modeling sub-committee finally converged on a model based on the cluster approach proposed by Turin and others in 1972 [68], and further formalized by Saleh and Valenzuela in 1987 [69] in a seminal work on statistical modeling for indoor multi-path propagation. Although derived on the basis of a

measurement campaign using low-power radar-like pulses, the Saleh and Valenzuela channel model (S-V) model is not UWB-specific.

The S-V model is based on the observation that usually multi-path contributions generated by the same pulse arrive at the receiver groped into clusters. The time of arrival of clusters is modeled as a Poisson arrival process with rate Λ:

$$p(T_n \mid T_{n-1}) = \Lambda e^{-\Lambda(T_n - T_{n-1})} \qquad \textbf{(A-1)}$$

where T_n and T_{n-1} are the times of arrival of the n-th and the (n-1)-th clusters, respectively. Here $T_1 = 0$ is set for the first cluster.

Within each cluster, subsequent multi-path contributions also arrive according to a Poisson process with rate λ:

$$p(\tau_{nk} \mid \tau_{(n-1)k}) = \lambda e^{-\lambda(\tau_{nk} - \tau_{(n-1)k})} \qquad \textbf{(A-2)}$$

where τ_{nk} and $\tau_{(n-1)k}$ are the time of arrival of the n-th and the (n-1)-th contributions within cluster k. The time of arrival of the first contribution within each cluster, that is, τ_{n1} for n=1,…., N, is set to zero.

In the S-V model, the gain of the n-th ray of the k-th cluster is a complex random variable a_n with modulus β_{nk} and phase θ_{nk}. The β_{nk} values are assumed to be statistically independent and Rayleigh distributed positive random variables, while the θ_{nk} values are assumed to be statistically independent uniform random variables over $[0,2\pi)$, or:

$$p(\beta_{nk}) = \frac{2\beta_{nk}}{\left\langle |\beta_{nk}|^2 \right\rangle} e^{-\frac{\beta_{nk}^2}{\left\langle |\beta_{nk}|^2 \right\rangle}} \qquad \textbf{(A-3)}$$

$$p(\theta_{nk}) = \frac{1}{2\pi} \quad \text{with} \quad 0 \le \theta_{nk} < 2\pi$$

where $\langle x \rangle$ is the expected value of x and where:

$$\left\langle \left|\beta_{nk}\right|^2 \right\rangle = \left\langle \left|\beta_{00}\right|^2 \right\rangle e^{-\frac{T_n}{\Gamma}} e^{-\frac{\tau_{nk}}{\gamma}} \qquad \textbf{(A-4)}$$

The term β_{00} in equation (A-4) represents the average energy of the first path of the first cluster, while Γ and γ are the power decay coefficients for clusters and multi-path, respectively. According to equation (A-4), the average power delay profile (PDP) is characterized by an exponential decay of the amplitude of the clusters, and a different exponential decay for the amplitude of the received pulses within each cluster, see Figure A-1.

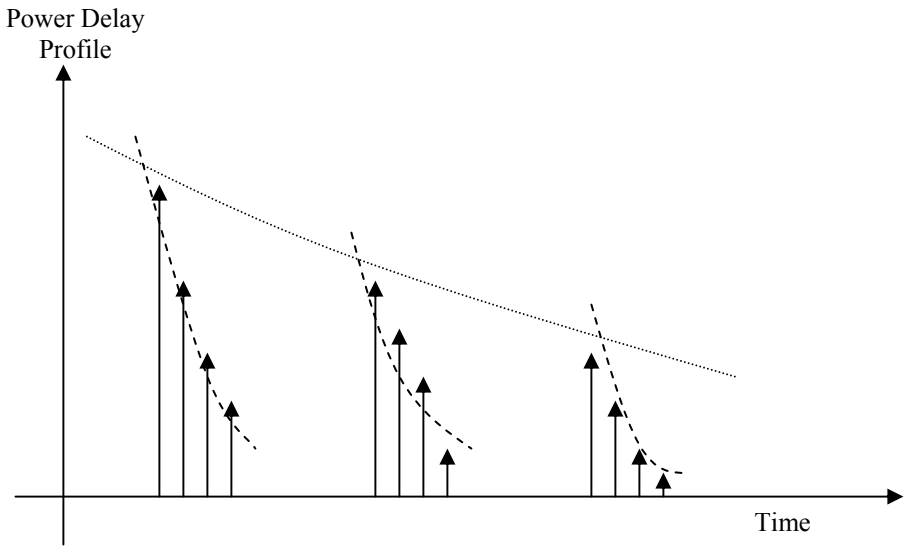

Figure A-1. Typical PDP for S-V channel model.

To be fit the data resulting from UWB measurement campaigns, the IEEE group proposed a few modifications to the S-V model. In particular, a log-normal distribution was suggested for characterizing the multi-path gain amplitudes and an additional log-normal variable was introduced for representing the fluctuations of the total multi-path gain. Finally, the channel coefficients were assumed to be real variables rather than

complex variables, that is the phase term θ_{nk} will assume $\pm\pi$ with equal probability for representing pulse inversion due to reflection from dielectric surfaces.

The channel impulse response of the IEEE model can be expressed as follows:

$$h(t) = X\sum_{n=1}^{N}\sum_{k=1}^{K(n)}\alpha_{nk}\delta(t - T_n - \tau_{nk}) \quad \textbf{(A-5)}$$

where X is a log-normal random variable representing the amplitude gain of the channel, N is the number of observed clusters, $K(n)$ is the number of multi-path contributions received within the n-th cluster, α_{nk} is the coefficient of the k-th multi-path contribution of the n-th cluster, T_n is the time of arrival of the n-th cluster, and τ_{nk} is the delay of the k-th multi-path contribution within the n-th cluster.

The channel coefficient α_{nk} can be defined as follows:

$$\alpha_{nk} = p_{nk}\beta_{nk} \quad \textbf{(A-6)}$$

where p_{nk} is a discrete random variable assuming values ± 1 with equal probability and β_{nk} is the lognormal distributed channel coefficient of multi-path contribution k belonging to cluster n. The β_{nk} term can thus be expressed as follows:

$$\beta_{nk} = 10^{\frac{x_{nk}}{20}} \quad \textbf{(A-7)}$$

where x_{nk} is assumed to be a Gaussian random variable with mean μ_{nk} and standard deviation σ_{nk}. Variable x_{nk} in particular, can be further decomposed as follows:

$$x_{nk} = \mu_{nk} + \zeta_n + \zeta_{nk} \quad \textbf{(A-8)}$$

where ζ_n and ξ_{nk} are two Gaussian random variables that represent the fluctuations for the channel coefficient on each cluster and on each contribution, respectively. We

indicate the variance of ζ_n and ζ_{nk} by σ_ζ^2 and σ_ξ^2. The μ_{nk} value is determined to reproduce the exponential power decay for the amplitude of the clusters and for the amplitude of the multi-path contribution within each cluster. One can thus write:

$$\begin{aligned} \left\langle \left|\beta_{nk}\right|^2 \right\rangle &= \left\langle \left| 10^{\frac{\mu_{nk}+\zeta_n+\xi_{nk}}{20}} \right|^2 \right\rangle \cong \left\langle \left|\beta_{00}\right|^2 \right\rangle e^{-\frac{T_N}{\Gamma}} e^{-\frac{\tau_k}{\gamma}} \\ \Rightarrow \mu_{nk} &= \frac{10\log_e\left(\left\langle \left|\beta_{00}\right|^2 \right\rangle\right) - 10\frac{T_n}{\Gamma} - 10\frac{\tau_k}{\gamma}}{\log_e 10} - \frac{\left(\sigma_\zeta^2 + \sigma_\xi^2\right)\log_e 10}{20} \end{aligned} \qquad \textbf{(A-9)}$$

The total energy contained in the β_{nk} terms must be normalized to unity for each realization, that is:

$$\sum_{n=1}^{N}\sum_{k=1}^{K(n)} \left|\beta_{nk}\right|^2 = 1 \qquad \textbf{(A-10)}$$

According to the S-V model, the arrival time variables T_n and τ_{nk} are assumed to be modeled by two Poisson processes with average rates Λ and γ, respectively.

The amplitude gain X is assumed to be a log-normal random variable:

$$X = 10^{\frac{g}{20}} \qquad \textbf{(A-11)}$$

where g is a Gaussian random variable with mean g_o and variance σ_g^2. The g_o value depends on the average total multi-path gain G, which is measured at the location under examination, that is:

$$g_o = \frac{10\log_e G}{\log_e 10} - \frac{\sigma_g^2 \log_e 10}{20} \qquad \textbf{(A-12)}$$

According to the above definitions, the channel model represented by the impulse response of equation (A-5) is fully characterized when the following parameters are defined:

- The cluster average arrival rate Λ
- The pulse average arrival rate λ
- The power decay factor Γ for clusters
- The power decay factor γ for pulses within a cluster
- The standard deviation σ_{ζ_1} of the fluctuations of the channel coefficients for clusters
- The stand deviation σ_{ξ_2} of the fluctuations of the channel coefficients for pusles within each cluster
- The standard deviation σ_g of the channel amplitude gain

The IEEE suggested an initial set of values for the above parameters. These values were tuned to fit some of the measurement data submitted to the IEEE. The list of parameters for different environmental scenarios as defined by the IEEE is provided in Table A-1.

Table A-1. Parameter setting for the IEEE UWB channel model.

Scenario	$\Lambda(1/ns)$	$\lambda(1/ns)$	Γ	γ	$\sigma_{\zeta_1}(dB)$	$\sigma_{\xi_2}(dB)$	$\sigma_g(dB)$
CM1 LOS (0-4 m)	0.0233	2.5	7.1	4.3	3.39941	3.3941	3
CM2 NLOS (0-4 m)	0.4	0.5	5.5	6.7	3.3941	3.3941	3
CM3 NLOS (4-10 m)	0.0667	2.1	14	7.9	3.3941	3.3941	3
CM4 Extreme NLOS multi-path channel	0.0667	2.1	24	12	3.3941	3.3941	3

Appendix B

Temporal Diversity and the Rake Receiver

The multi-path affected received signal $r(t)$ consists of the superimposition of several attenuated, delayed and eventually distorted replicas of a transmitted waveform $y_m(t)$. When propagation fluctuations within an observation time $T >> T_b$ and path-dependent distortions can be neglected, $r(t)$ can be expressed as follows:

$$r(t) = \sum_j a_j y_m(t - \tau_j) + n(t) \qquad \textbf{(B-1)}$$

where $n(t)$ is the AWGN at the receiver input.

Equation (B-1) can be rewritten for IR transmissions on the basis of the statistical channel model discussed in Appendix A.

$$r(t) = X\sqrt{E_{TX}}\sum_j \sum_{n=1}^{N} \sum_{k=1}^{K(n)} \alpha_{nk} a_j p_o(t - jT_s - \varphi_j - \tau_{nk}) + n(t) \qquad \textbf{(B-2)}$$

where

- X is the log-normal distributed amplitude gain of the channel
- E_{TX} is the transmitted energy per pulse
- N is the number of clusters observed at destination
- K(n) is the number of multi-path contributions associated with the n-th cluster
- α_{nk} is the channel coefficient of the k-th path within the n-0th cluster
- a_j is the amplitude of the j-th transmitted pulse
- T_s is the average pulse repetition period.
- φ_j is the time dithering associated to the j-th pulse
- τ_{nk} is the delay of the k-th path within the n-th cluster

The energy contained in the channel coefficients α_{nk} is normalized to unity for each realization of the channel impulse response, that is:

$$\sum_{n=1}^{N}\sum_{k=1}^{K(n)}\left|\alpha_{nk}\right|^2 = 1 \qquad \textbf{(B-3)}$$

and equation (B-2) can be rewritten as follows:

$$r(t) = \sqrt{E_{RX}}\sum_j \sum_{n=1}^{N}\sum_{k=1}^{K(n)}\alpha_{nk}a_j p_o(t - jT_s - \varphi_j - \tau_{nk}) + n(t) \qquad \textbf{(B-4)}$$

where $E_{RX} = X^2 E_{TX}$ is the total received energy for one transmitted pulse. Different from the AWGN channel, E_{RX} is spread in time over the different multi-path contributions and can be used by the detector if the receiver is capable of capturing all replicas of the same pulse. Realistically, the receiver can only analyze a finite subset of N_R contributions and the effective energy E_{eff}, which is used in the decision process, is smaller than E_{RX}, that is

$$E_{eff} = E_{RX}\sum_{j=1}^{N_R}\left|\alpha_j\right|^2 \le E_{RX} \qquad \textbf{(B-5)}$$

According to equation (B-4), different replicas of the same transmitted pulse overlap at the receiver only when the corresponding inter-arrival time is smaller than pulse duration T_M. In this case, signals associated with different paths are not independent, that is, the amplitude of the pulse observed at time t is affected by the presence of multi-path contributions arriving immediately before or after time t. Given the characteristics of the propagation channel, the number of independent paths at the receiver depends on T_M: the smaller T_M, the higher the number of independent contributions at the receiver input. For IR-UWB systems, the T_M value is on the order of

nanoseconds or fractions of nanoseconds, leading to the hypothesis that all multi-path contributions are non-overlapping, so that the received waveform consists of several independent components [70]. IR-UWB systems can thus I principle take advantage of multi-path propagation by combining a large number of different and independent replicas of the same transmitted pulse. In this case, we say that the receiver exploits temporal diversity of the multi-path channel to improve performance of the decision process.

Different strategies for exploiting diversity can be adopted by the receiver: Selection Diversity (SD), Equal Gain Combining (EGC) and Maximal Ratio Combining (MRC). With the SD method, the receiver selects the multi-path contribution exhibiting the best signal quality and operates the decision on the transmitted symbol based on the observation of this contribution only. Choosing the best path guarantees an increase in receiver performance with respect to the simple selection of the first path, deriving from having selected the path with highest instantaneous SNR. A different method for increasing SNR consists of combining multi-path contributions rather than selecting the best path. With the EGC method in particular, the different contributions are first aligned in time and then added without any particular weighting. In MRC, the different contributions are weighted before the combination and the weights are determined to maximize the SNR before the decision process. In the presence of Gaussian noise at the receiver, the SNR is maximized by applying to each multi-path contribution a weighting factor that is proportional to the amplitude of the corresponding received signal. In other words, the MRC method adjusts the received contributions before combining them. The adjustment is performed by amplifying the strongest components and by attenuating the

weak ones. In a single-user communication system without ISI, the method that achieves the best performance is the MRC, which ensures the largest SNR at the combiner output.

In all the above cases, the receiver takes advantage of multi-path under the hypothesis that different replicas of the same transmitted pulse can be analyzed separately and eventually combined before decision. The optimum correlator for the present case must include additional correlators associated with different replicas of a same transmitted waveform. Such a scheme was invented by [71] and is called the RAKE receiver, see figure B-1.

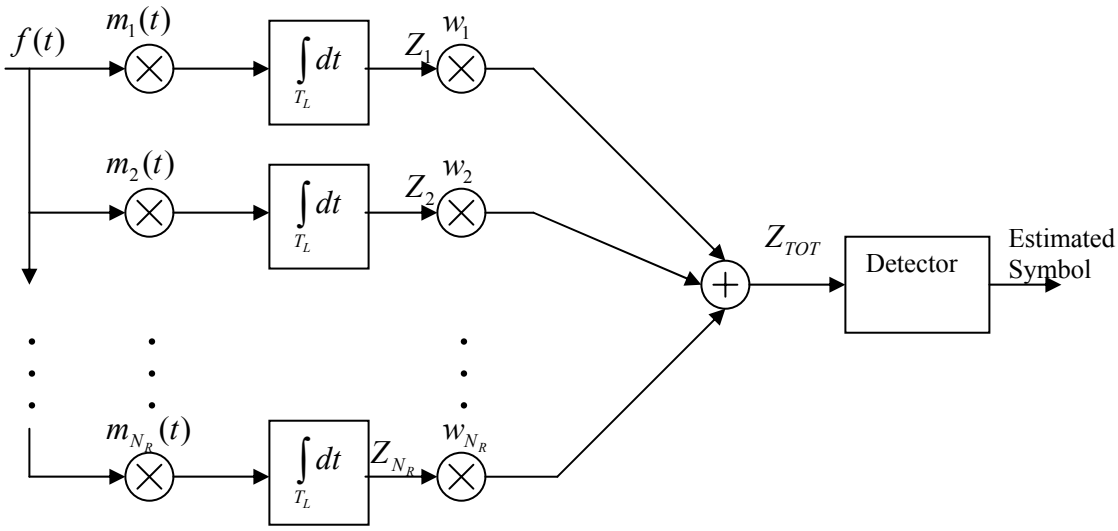

Figure B-1. Rake receiver with N_R parallel correlators.

In figure B-1, $T_L > T_s$ represents the time duration of the channel impulse response, and Z_{TOT} is the decision variable at the output of the RAKE combiner that enters the detector. Figure B-1 shows the structure of the RAKE receiver, which consists of a parallel bank of N_R correlators, followed by a combiner that determines the variable to be used for the decision on the transmitted symbol. Each correlator is locked on one of the different replicas of the transmitted symbol, that is, the correlator mask

$m_j(t)$ on the j-th branch of the RAKE is aligned in time with the j-th delayed replica of the transmitted symbol, or:

$$m_j(t) = m(t - \tau_j) \qquad \textbf{(B-6)}$$

where $m(t)$ is the correlator mask and τ_j is the propagation delay that characterizes the j-th path. The output of the bank of correlators feeds the combiner. Depending on the diversity method implemented at the receiver, a different set of weighting factors $\{w_1,.....,w_{N_R}\}$ is used to combine the outputs of the correlators. In the SD case, the weighting factors are equal to zero, except for the factor on the branch corresponding to the signal with highest amplitude, which is equal to one. In the case of EGC, all factors are equal to 1, that is , the combiner simply adds the outputs of the corrrelators without applying any weighting. Finally, in the MRC case, the output of each branch is multiplied by a weighting factor, which is proportional to the signal amplitude on that branch.

An alternative but equivalent implementation of the RAKE receiver is shown in Figure B-2, where the N_R correlators are preceded by time shift elements. The function of these elements is to align all multi-path contributions in time. The advantage of the solution of Figure B-2 with respect to the schemed of the Figure B-1 is in the possibility of adopting the same correlator mask $m(t)$ on all branches of the RAKE.

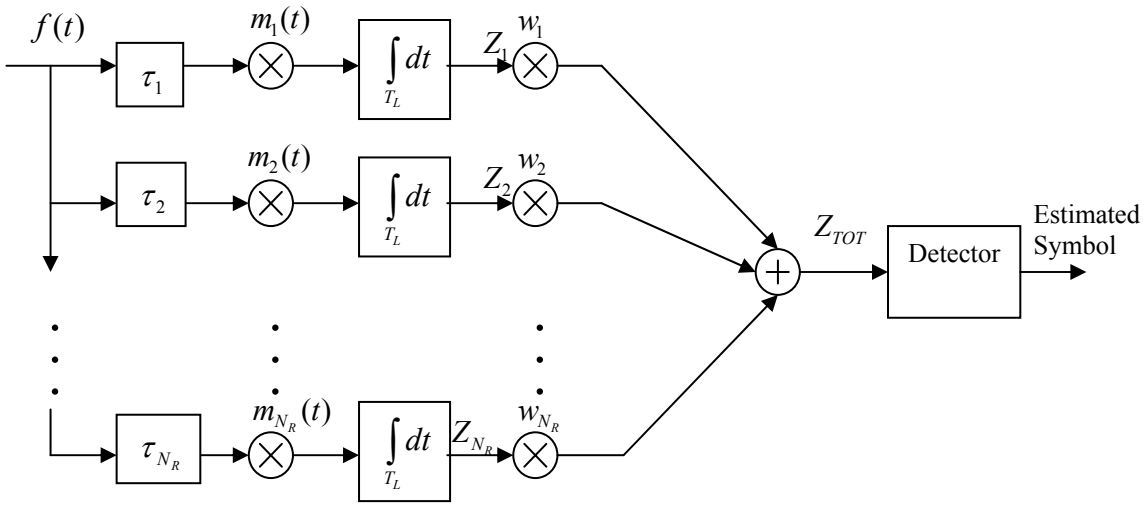

Figure B-2. RAKE receiver with N_R parallel correlators and time delay units.

According to the schemes of Figure B-1 and B-2, the RAKE receiver must know the time distribution for all multi-path contributions composing the received waveform. This task is performed by supplying the RAKE with the capability of scanning the channel impulse response, tracking and adjusting the delay of a certain number of multi-path components. Time delay synchronization for the different multi-path contributions is based in general on correlation measurements that are performed on the received waveform. In addition, if the SD or MRC methods are adopted within the combiner, the knowledge of the amplitudes of the multi-path component is also required for adjusting the weighting factors. This task is performed in general by using pilot symbols for channel estimation.

The RAKE scheme of Figure B-2 can be greatly simplified when the channel is modeled with a discrete time impulse response, as discussed in Appendix A. In this case, the different contributions at the receiver are spaced in time by a multiple of the bin duration ∇t and a single correlators structure is possible for the RAKE, see Figure B-3. In Figure -3, the correlators integrates the product between $m(t)$ and the received

waveform $f(t)$. The output of the correlator is sampled with period $\nabla\tau$ before passing through a delay unit and a combiner, which implements one of the previously described diversity methods: SD, EGC or MRC.

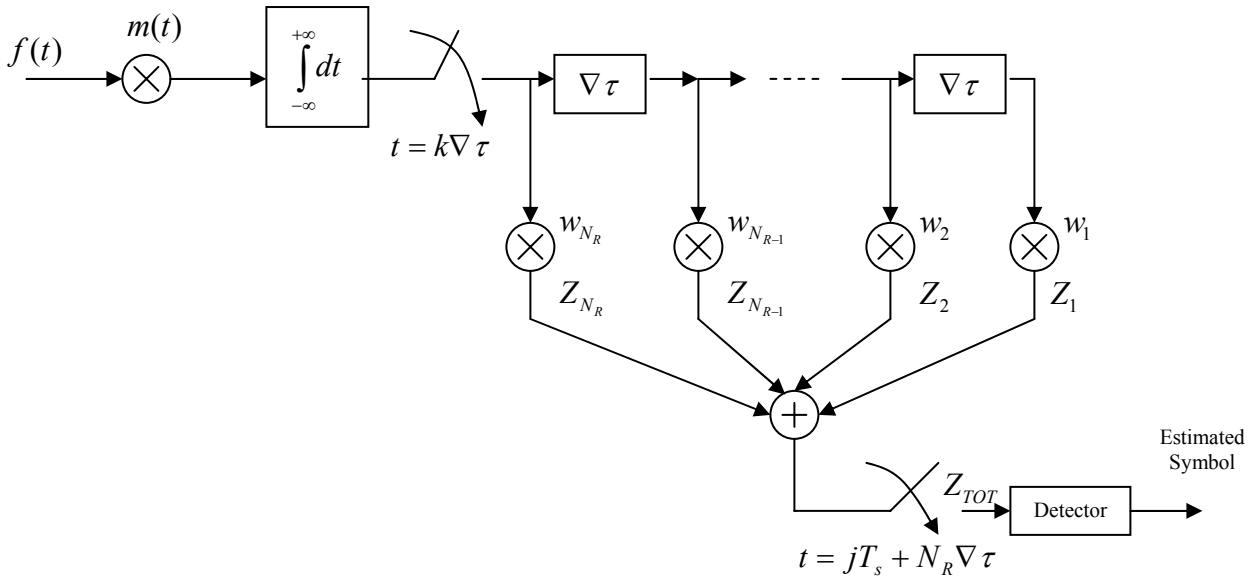

Figure B-3. RAKE receiver for discrete-time channel models.

Performance of the RAKE receiver for propagations over a multi-path channel can be evaluated by first assuming a specific model for the channel impulse response and by then evaluating the probability of error on the symbol Pr_e as a function of the E_{RX}/N_o ratio for the different diversity methods. This analysis is performed in general under the hypothesis of perfect knowledge of the coefficients of the channel impulse response, or perfect channel estimation.

The adoption of a RAKE considerably increases the complexity of the receiver. This complexity increase with the number of multi-path components analyzed and combined before decision and can be reduced by decreasing the number of components processed by the receiver. According to equation (B-5), however, a reduction of the number of paths leads to a decrease of energy collected by the receiver. A quasi-

analytical investigation of the existing tradeoff between receiver complexity and percentage of captured energy in a RAKE receiver for IR-UWB systems is presented in [72]. The results of this analysis show that a RAKE receiver operating in a a typical modern office building requires about 50 different RAKE branches to capture about 60% of the total energy of the received waveform. In [73], different strategies for reducing the complexity of the RAKE are presented and analyzed in terms of Pr_e degradation. The first strategy, called Selective RAKE, consists of selecting the L_B best components among the L_{TOT} available at the receiver input. The number of branches of the RAKE is reduced, but the receiver still must keep track of all the multi-path components to perform the selection. A second and simpler solution, called Partial RAKE, combines the first arriving L_P paths without operating any selecting among all available multi-path components. As expected, Selective RAKE outperforms Partial RAKE since it achieves higher SNR at the output of the combiner. The gap in performance, however, decreases when the best paths are located at the beginning of the channel impulse response as it happens, in general, when considering LOS scenarios.